

# Sheffield Hallam University

*Organic:inorganic heterojunctions for photovoltaic devices.*

VALE, Alistair Douglas John.

Available from the Sheffield Hallam University Research Archive (SHURA) at:

<http://shura.shu.ac.uk/20472/>

## A Sheffield Hallam University thesis

This thesis is protected by copyright which belongs to the author.

The content must not be changed in any way or sold commercially in any format or medium without the formal permission of the author.

When referring to this work, full bibliographic details including the author, title, awarding institution and date of the thesis must be given.

Please visit <http://shura.shu.ac.uk/20472/> and <http://shura.shu.ac.uk/information.html> for further details about copyright and re-use permissions.

CITY CAMPUS, HOWARD STREET  
SHEFFIELD S1 1WB



**REFERENCE**

ProQuest Number: 10701119

All rights reserved

INFORMATION TO ALL USERS

The quality of this reproduction is dependent upon the quality of the copy submitted.

In the unlikely event that the author did not send a complete manuscript and there are missing pages, these will be noted. Also, if material had to be removed, a note will indicate the deletion.



ProQuest 10701119

Published by ProQuest LLC (2017). Copyright of the Dissertation is held by the Author.

All rights reserved.

This work is protected against unauthorized copying under Title 17, United States Code  
Microform Edition © ProQuest LLC.

ProQuest LLC.  
789 East Eisenhower Parkway  
P.O. Box 1346  
Ann Arbor, MI 48106 – 1346

# **ORGANIC:INORGANIC HETEROJUNCTIONS FOR PHOTOVOLTAIC DEVICES**

**Alistair Douglas John Vale**  
**BEng (Hons.)**

**A thesis submitted in partial fulfilment of the requirements of  
Sheffield Hallam University  
for the degree of Doctor of Philosophy**

**July 2005**



## **Declaration**

I hereby declare that this thesis submitted for the degree of Ph.D. is the result of my own research and that this thesis has not been submitted for a higher degree to any other university or institution.

Signed

**Alistair Vale**

## Abstract

Thin films of  $\text{TiO}_2$  with a thickness around 200nm were produced by DC reactive sputtering at room temperature. A variety of types of bandgap including direct allowed, direct forbidden, indirect allowed, and indirect forbidden were observed, with good fits of the Tauc model, between annealed and unannealed samples, and within the same sample. Planar conductivity was measured at  $8.7 \times 10^{-3} \Omega^{-1} \text{m}^{-1}$ , falling to  $7.4 \times 10^{-3} \Omega^{-1} \text{m}^{-1}$  after annealing. Refractive index and extinction coefficient spectra were obtained via the Swanepoel technique and were found to be around 2.2 and  $3 \times 10^{-3}$  respectively, in the region of weak absorption, with little change after annealing. Surface details in the micro and nano regimes showed flat films with few defects. XRD showed the Rutile phase dominating, and XPS showed correct stoichiometry. AFM showed the grain size to be in the range of 64nm rising to 82nm after annealing.  $\text{TiO}_2$  films with an extended surface area were made using Degussa P25 and were deposited by the new technique of flood printing developed for this research. 2D profiles of thin films of P25 were measured at different concentrations and the thickness of the highly rough films was in the range of  $5 \mu\text{m}$  to  $15 \mu\text{m}$  rising with increasing concentration. AFM also showed films that were highly rough in the nanoscale.

Thin films of CuPc and Rose Bengal were deposited on differently coated substrates; F:TO,  $\text{TiO}_2$ , and bare glass. The absorption spectra was seen to vary significantly with substrate, in particular, the 530nm peak of Rose Bengal was seen to diminish greatly when the dye was deposited on  $\text{TiO}_2$ .

Heterojunction photovoltaic devices based on dye layers adsorbed on semiconducting layers were produced in fifteen different designs with each design based on another to observe the effect of single parameters changes. Such changes included different thickness of porous  $\text{TiO}_2$  layer, and whether a conducting polymer layer is applied. The devices were built up on F:TO coated glass slides and electrical contacts were made by DC sputtering platinum fingers on the top. The best device design gave a fill factor of 35.5%, and an overall conversion efficiency of  $4.2 \times 10^{-3}\%$ . Devices were thought to be greatly affected by series resistance from the top contact being applied to a highly rough surface. The top contact on different structures were electrically characterised and were found to have resistances in the region of  $\text{k}\Omega$ , which manifests as a high series resistance in the final solar cells. This is one of the reasons for the low efficiency. The I(V) spectra of all the devices were fitted to a diode model using an algorithm developed for this research. The model fit gave reverse saturation currents in the range of  $3.2 \times 10^{-9} \text{A}$  to  $7.5 \times 10^{-3} \text{A}$ . Ideality factor varied from 3.8 to 80, series resistance varied from  $15 \Omega$  to  $500 \Omega$ , and parallel resistance varied from  $117 \Omega$  to  $778 \text{k}\Omega$ .

An experimental setup capable of measuring the lifetime of photogenerated carriers in the dye films was developed that could produce pulses with a cut off time in the nano-seconds time regime, but can be simply improved to give cut off times in the sub nano-second regime, and only costs around £200 for the optical modulator.

## **Acknowledgements**

I would like to thank all the people who assisted me in this research. I would also like to thank the Digital Technology Research Studentship for the funding without which the research would have been unaffordable.

I would finally like to thank all the scientists who worked before me, without whom this work would surely have been impossible.

# CONTENTS OF THESIS

## DECLARATION

## ABSTRACT

## ACKNOWLEDGEMENTS

## CHAPTER 1

### INTRODUCTION

1.1. General Introduction	1
1.2. Aims and Objectives	6
1.3. Organisation of the Thesis	6
Reference List	7

## CHAPTER 2

### LITERATURE REVIEW

2.1. Dye-Sensitised Solar Cells	8
2.1.1. Dye: Metal Oxide Cells in General	8
2.1.2. Dye: TiO <sub>2</sub> Cells	9
2.2. Titanium Dioxide Thin Films	10
2.2.1. Sputtered	11
2.2.2. Nano Powder	13
2.3. Dyes and Other Layers	15
2.3.1. CuPc, Rose Bengale, poly(9-vinylcarbazole) (PVK)	15
2.3.2. Other Commonly Used Chemicals	19
2.4. Light Modulation	19
Reference List	21

## CHAPTER 3

### THEORETICAL BACKGROUND

3.1. Structural characteristics	25
3.1.1. Crystallographic Phase	25
3.1.2. Microscopic and Nanoscopic Details	28
3.1.3. Stoichiometry	29
3.2. Electrical Characteristics	29
3.2.1. Conventional Solid State Solar Cell	29
3.2.2. Dye Sensitised Solar Cell	31
3.2.3. Diode Model Fitting	34
3.3. Optical Characteristics	37
3.3.1. n Spectra and k Spectra	38
3.3.2. The Ray-Hogarth and Vale Procedures	40
3.3.3. The Swanepoel Procedure	43
3.4. Description of Selected Measurement Methods	46
3.4.1. Atomic Force Microscopy	46
3.4.2. X-Ray Diffraction	48
3.4.3. X-Ray Photoelectron Spectroscopy	51
3.4.4. Spectroscopic Ellipsometry	52
3.5. Basic Theory of the Optical Modulator	56
Reference List	59

## **CHAPTER 4**

### **EXPERIMENTAL METHODS**

4.1. Preparation of Samples	60
4.1.1. Sputtered TiO <sub>2</sub> Thin Films	60
4.1.2. Powder TiO <sub>2</sub> Thin Films	62
4.1.3. Fabrication of Solar cells	63
4.2. Structural Measurements	68
4.2.1. Atomic force microscopy	68
4.2.2. Scanning electron microscopy	69
4.2.3. X-Ray Diffraction	70
4.2.4. X-Ray Photoelectron Spectroscopy	70
4.2.5. Surface 2-D Profilometry	71
4.3. Electrical Measurements	71
4.3.1. DC Voltage Characteristics	71
4.3.2. Load Resistance Characteristics	72
4.4. Optical Measurements	72
4.4.1. Optical Microscopy	72
4.4.2. UV-Vis Absorption Spectroscopy	73
4.4.3. Spectroscopic Ellipsometry	73
Reference List	74

## **CHAPTER 5**

### **RESULTS AND DISCUSSIONS**

5.1. Sputtered TiO <sub>2</sub> Layer	75
5.1.1. Structural Characteristics	75
5.1.2. Optical Characteristics	83
5.1.3. Electrical Characteristics	93
5.2. Nano Powder TiO <sub>2</sub> Layer	96
5.2.1. Structural Characteristics	96
5.2.2. Optical Characteristics	100
5.3. Dye Layer Optical Characteristics	103
5.4. Solar Cells Electrical Characteristics	105
5.5. Top Cell Contact	119
5.5.1. Optical Characteristics	119
5.5.2. Electrical Characteristics	123
5.6. Optical Modulator	127
5.6.1. Development	127
5.6.2. Final Design and Tests	135
Reference List	137

## **CHAPTER 6**

### **CONCLUSION AND SUGGESTIONS FOR FURTHER WORK**

6.1. Discussion of Achievements	139
6.2. Contribution to Knowledge	141
6.3. Future Work	142

## Introduction

---

### 1.1. General Introduction

Mankind uses huge amounts of energy in a multitude of ways; transport, heating, entertainment, industrial manufacture etc. The energy typically comes from 'fossil fuels' (which are running out), or from nuclear reaction (which has many problems associated with extraction of raw materials, containment of used materials, and decommissioning of power plants). There are of course good aspects of these energy sources least of all that they are mature technologies and are reliable until the energy supply runs out. A better long term solution would be to use so called renewable sources of energy that are effectively never ending. The main renewable sources of energy are described below.

Natural organic material from plants (such as wood and straw) and animals (such as chicken and cattle faeces) are collectively known as 'biomass' (1). The biomass contains energy that can be released in various ways, such as the burning of dry wood chips to obtain heat, or the digestion of faeces to obtain methane that can then be burned to obtain heat. The heat can be used directly to provide heating of space and water, or indirectly to provide electricity via steam turbines (like in a normal power station). This has the same problem as coal burning power stations in that it produces a lot of carbon dioxide. In order for the biomass use not to increase the amount of carbon dioxide in the

environment, the biomass must be made as fast as it is used i.e. for every plant or tree burned, another must be planted to replace it.

Energy extracted from the heat of the earth itself is known as geothermal energy (2). Geothermal energy can be tapped into for providing hot water for electricity, heating for houses and bathing, and for industry. Although it is used worldwide (95% of the buildings in and around the Icelandic city of Reykjavik are heated by springs providing water at 86°C), it is not fully utilised and remains to be a great option for environmentally friendly energy. A geothermal reservoir is a mass of fractured rock in the earth's surface that contains hot water or steam. Wells can be drilled into them and the water or steam extracted (with or without a pump). The water or steam can be used to drive a turbine and produce electricity or used directly as a heat source for buildings.

The energy contained in the wind (3) has been used for hundreds of years for (initially) simple operations like milling grain or to pump water. In more recent years, the wind is used to drive a turbine to produce electricity either for the power grid, or for local use. This form of energy has great potential both onshore and offshore, as it is one of the cleanest and safest sources of renewable energy available. The UK has the largest wind resource in Europe. A draw back of harnessing this type of energy is the very large and unsightly windmills dotted across the open landscape (compared with a single large and unsightly estate for a normal power station). The cost of electricity from a 'wind farm' can be as little as 2p/kWh, which compares favourably with normal sources.

The energy contained in moving water (4) has also been used for hundreds of years, for (initially) driving water wheels that drove machinery like cotton mills. More recently, the power of water has been used to drive turbines to produce electricity. Hydropower

produces around 2% of the electricity needs of the UK, which is mostly in small dams. Inland hydropower uses the potential energy (via water dropped from a reservoir behind a dam) or kinetic energy (via turbines placed in the river with no reservoir) of water to drive a turbine. Off shore hydropower can use the energy of waves to drive many different types of machine. This type of hydropower is more complicated, as there isn't a constant flow of water, instead a constant undulation. Such designs include a mechanical 'snake' whose sections are flexed back and forth (with the sections driving some sort of generator) by the force of the wave.

The last main renewable energy source is direct from the sun (5), which is also known as solar energy, and is captured by solar panels. There are two main types of solar panel; solar water heaters, which can consist of a black metal sheet (to absorb the heat) on which are attached pipe work for the water to flow around and be heated in. The other type of solar panel is the photovoltaic cell, which produces a voltage when illuminated by light, which can be used to drive an electrical load. The panels can be attached to the roofs of buildings of all sorts (providing that the panel faces the sun), and even transport vehicles like trains, and cars. A solar farm may be built, similar to the wind farm; an area of land that gets a lot of sunshine may be covered with photovoltaic panels oriented at the best angle. A problem with this is that the area covered by the panels is completely unusable and not even plants may grow there because the sun is blocked out. The rooftop coverage is probably the most appropriate utilisation of this technology.

The photovoltaic panel (called solar cell from now on) is the simplest type of electricity providing renewable energy source transformer, as it requires no moving parts (mainly no turbine which the others have in common) and can be made without liquids (i.e. can

be 'solid state'). This means that it can be used to power portable (or just small) devices like watches, calculators, parking meters, burglar alarms etc. The main drawbacks with solar cells are their relatively low conversion efficiency, around 9% for good quality amorphous silicon cells as shown in table 1.1 (6), and the high level of technology usually required to produce them. The vast majority of solar cells are based on Silicon in one form or another. The various most common technologies are presented in fig 1.1 (7). The world market for solar cells has been increasing rapidly since 1992, as shown in fig 1.2 (7), and whilst this is only a small percentage of the total world electrical use, it is a good sign that we are heading towards cleaner energy.

Table 1.1. Comparison of the photovoltaic parameters of cells under AM1.5 sunlight

Semiconductor	$E_g$ (eV)	$V_{oc}$ (V)	Max $J_{sc}$ (mA cm <sup>-2</sup> )	FF	$\eta$ (%)	Comment
Si, single crystal	1.1	0.5-0.69	42	0.7-0.8	16-24	Amorphous film with tandem structure. Convenient large area fabrication
Si, polycrystalline	1.1	0.5	38	0.7-0.8	12-19	
Amorphous Si:Ge:H film					8-10	
GaAs, single crystal	1.42	1.03	27.6	0.85	24-25	Different bandgap materials in tandem increases absorption efficiency
AlGaAs/GaAs Tandem		1.03	27.9	0.864	24.8	
GaInP/GaAs Tandem	-	2.5	14	0.86	25-30	Different bandgap materials in tandem increases absorption efficiency
CdTe Thin film	1.5	0.84	26	0.73	15-16	polycrystalline films
InP, single crystal	1.34	0.88	29	0.85	21-22	
CuInSe <sub>2</sub>	1.0				12-13	

There are alternatives to the normal silicon based cells, one of which is dye sensitised metal oxide cell. These comprise a large bandgap semiconductor like Titanium Dioxide with a dye adsorbed to harvest the light. This type of cells promises simple technology, and potentially useful light conversion efficiency (around 7% for a cell with a liquid electrolyte). The simplicity of the technology and potentially low cost of the materials

makes this type of cell far cheaper than many of the other types of cell. This research will concentrate on optimising dye sensitised cells.

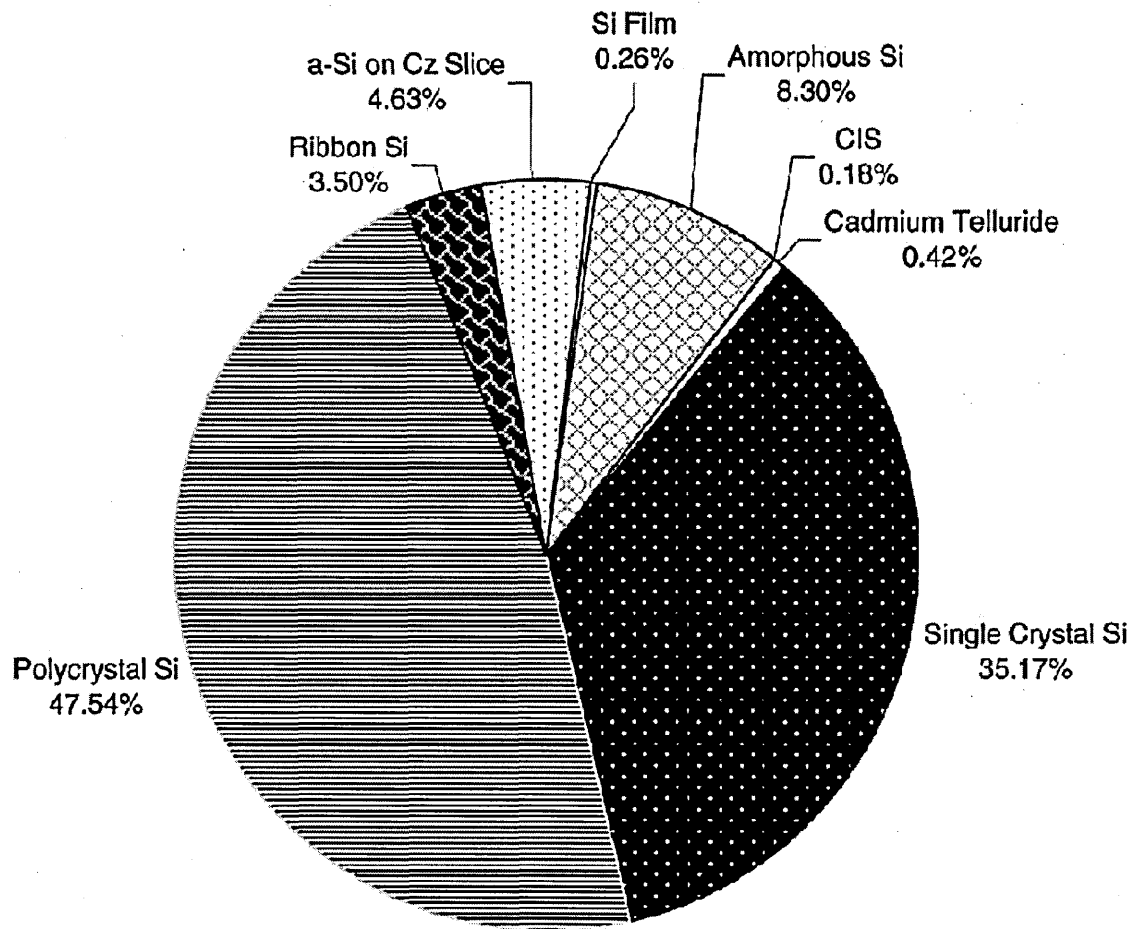


Figure 1.1. Percentages of the most common photovoltaic cell technologies.

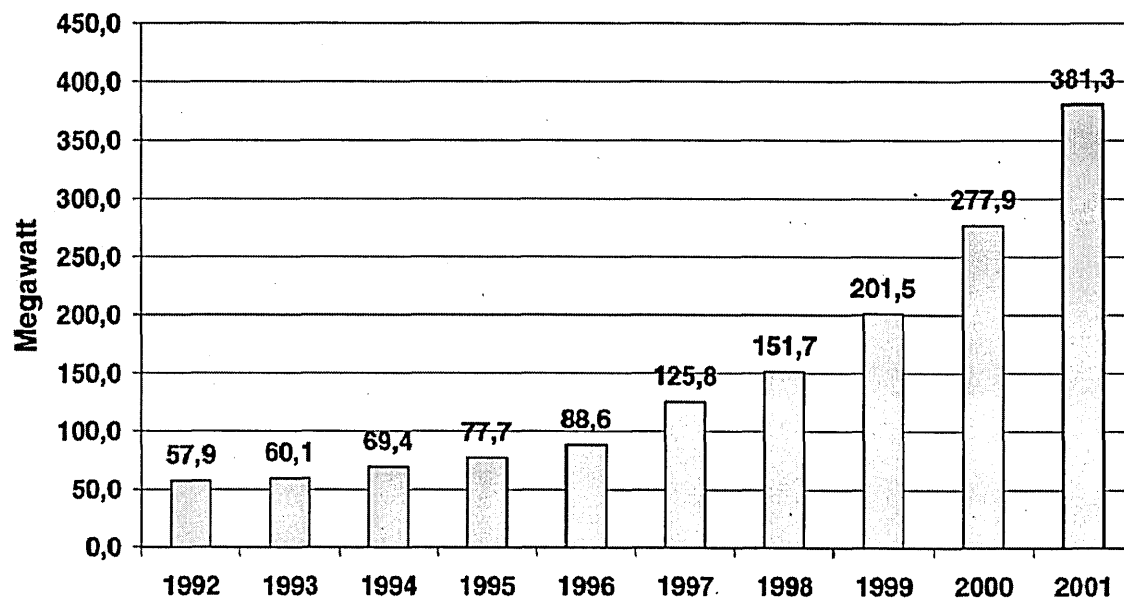


Figure 1.2. World market of photovoltaic cells increasing with years.

## **1.2. Aims and Objectives**

- Develop and deposit semiconducting layers of Titanium Dioxide (TiO<sub>2</sub>) with and without an extended surface area made using a fine powder
- Characterise the semiconducting layers using a variety of appropriate techniques
- Develop and deposit various thin dye layers adsorbed on different substrates by various methods
- Characterise the dye layers using appropriate techniques
- Develop and attempt to optimise heterojunction solar cells based on the dye layers adsorbed on the semiconducting layers
- Characterise the solar cells in terms of efficiency, load characteristics, and equivalent circuit model parameters.
- Design and produce an experimental setup capable of measuring the lifetime of photogenerated carriers in thin films of dye

## **1.3. Organisation of the Thesis**

This thesis is comprised of the following chapters; Introduction, Literature Review, Theoretical Background, Experimental Methods, Result and Discussions, and Conclusions and Suggestions for Further Work. The literature review chapter describes published work that is relevant to this research, so that the reader may quantify this work in terms of other previous work. The theoretical background chapter presents any mathematical methods used for data analysis, along with the physical theory of selected measurements techniques, and of the operation of solar cells. The experimental methods chapter describes how each type of sample was made, and practical information regarding the measurements of the samples. The results and discussions chapter describes the results that were obtained, and discusses the implications of the results and how they compare with published work. The conclusions chapter compares the research

aims with actual outcomes, describes how the research furthers academic knowledge, and what work can be done to further this research.

#### Reference List

- (1) <http://www.nef.org.uk/greenenergy/biomass.htm> accessed 17th June 2005
- (2) <http://www.nef.org.uk/greenenergy/geothermal.htm> accessed 17th June 2005
- (3) <http://www.nef.org.uk/greenenergy/wind.htm> accessed 17th June 2005
- (4) <http://www.nef.org.uk/greenenergy/hydro.htm> accessed 17th June 2005
- (5) <http://www.nef.org.uk/greenenergy/solar.htm> accessed 17th June 2005
- (6) Kasap S.O., 2001, Optoelectronics and Photonics : Principles and Practices.  
Prentice Hall
- (7) Goetzberger A., Hebling C., Schock H., Materials Science and Engineering  
2003, R40, 1-46

## Literature Review

---

### 2.1. Dye-Sensitised Solar Cells

Solar cells based on Titanium Dioxide films sensitised with a dye are a commonly researched topic due to their being an interesting potential option as a cheap source of 'green' electricity. Two main types of dye sensitised Titanium Dioxide cell are studied; those with an electrolyte and those without. Studies of both types will be described, but with emphasis on the type without an electrolyte (the 'dry' type).

#### 2.1.1. Dye: Metal Oxide Cells in General

There are many published works on dye sensitised solar cells with a  $\text{TiO}_2$  layer that also have a liquid layer. One such work (1) presented a cell comprised of; substrate/ $\text{SnO}_2$  nanopowder/Ruthenium dye/electrolyte/Pt. The cells were illuminated with a solar light of 200% ambient (such as that experienced using a condenser lens arrangement), and a fill factor of 65% and an efficiency of 6% were achieved. Another such work (2) presented a cell comprised of substrate/ $\text{ZnO}$  nanopowder/Ru dye/ $\text{LiI}+\text{I}_2$ /metal contact. A fill factor of 68% and an efficiency of 5% was achieved at 10% of full sunlight. It is common to test cells at less than full sunlight as the cell might be used in low light levels such as in buildings or in countries with little sunlight (such as England). The two above results are typical of the higher quality range of wet dye sensitised cells.

There are even fewer published works on dye sensitised solar cells without a liquid layer that do not have a  $\text{TiO}_2$  layer than for those that do have a liquid layer, which is

probably because of the greater efficiency normally obtained with a wet cell. One of those published (3) presents a cell comprised of Al/Al oxide/dye/Au (more details are in a paper referenced by the authors). The cell obtained a fill factor of 25% and an efficiency of  $5 \times 10^{-4}\%$  at full sun. The low efficiency obtained is common to dry sensitised cells and is probably due to insufficiently intimate contact between the top metal and the dye. Where the wet cell has better efficiency, the dry cell has simplicity and less likely to harm the environment by the leakage of toxic chemical (the liquid electrolyte).

### 2.1.2. Dye: TiO<sub>2</sub> Cells

There is much work published on dye sensitised TiO<sub>2</sub> solar cells with a liquid electrolyte. One such study (4) demonstrated a cell made up of; FTO/TiO<sub>2</sub> nanopowder/Ruthenium dye/electrolyte/Pt. The cell achieved 67% fill factor and 0.22% efficiency at 120% of full sunlight. Another study (5) presented a cell with the design; FTO (assumed)/TiO<sub>2</sub> nanopowder(treated with TiCl<sub>4</sub>)/ Mercurochrome dye/KCl/Pt. The cell gave a fill factor of 73% at full sunlight, and an efficiency of 1.44%. The most commonly referenced work (6), is one of the earliest works on modern dye sensitised TiO<sub>2</sub>, and it describes one of the best qualities of solar cell, giving a fill factor of 68.5% and an efficiency of 7.12% at full sunlight with a cell design of; FTO/TiO<sub>2</sub> nanopowder/Ruthenium dye/electrolyte/Pt. The majority of modern cells are based on this design.

There is also much work published on dye sensitised TiO<sub>2</sub> solar cells without a liquid electrolyte. One such study (7) on the design; ITO/TiO<sub>2</sub>/CuPc/Au gave a fill factor of about 25%, and an efficiency of about  $1.5 \times 10^{-4}\%$  under simulated solar light. Another study (8) described cells made of; FTO/nc-TiO<sub>2</sub>/Ru dye/Pentacene/Graphite, which

gave a fill factor of 49% and an efficiency of 0.8% under full sunlight illumination. Yet another article (9) described a cell of design; ITO/TiO<sub>2</sub>/MEH-PPV/Au, with a fill factor of 67% and an efficiency of 1.6%, but the illumination was only monochromatic light at 500nm.

It has been shown that a higher series resistance and a lower parallel resistance lead to a lower fill factor (10). Since the fill factor has a significant effect on efficiency, it is critical that a cell has low series resistance and a high parallel resistance (along with various other good characteristics) to have a useful efficiency. The ideality factor of dye sensitised solar cells normally ranges from 1.5 to 2 (11-13), when analysed with the one-diode model. The reverse saturation current has been shown to vary in the range from 15nA to 30nA for a particular design, the series resistance can vary in the range 2.5Ω to 142Ω, and the parallel resistance can vary in the range 1.3kΩ to 61kΩ. The diode ideality factor has been shown (14) to fall outside the above range, with a value of 2.9, and a corresponding value of saturation current of 1.15nA.

## **2.2. Titanium Dioxide Thin Films**

The inorganic layer of the cell studied in this research is comprised of a very thin ( $\leq 200\text{nm}$ ) layer of non-porous TiO<sub>2</sub> to cover the bottom contact and prevent short circuits, onto which is deposited a thicker (around 10μm) porous film to give an extended area of interface. Much work has been done to study such films made and measured in various ways, and the published work is described below.

### 2.2.1. Sputtered

There is a great wealth of published work on  $\text{TiO}_2$  produced by sputtering with various parameters (such as with Rf or DC power supply, or whether the target is metallic or a sub-oxide of Titania). The work on RF sputtering will be summarised first. AFM images of thin films of  $\text{TiO}_2$  have been obtained (15;16) that show grain sizes in the range 60nm to 176nm with roughness in the range 2.1nm to 6.6nm. X-Ray Diffraction (XRD) spectra have been presented (15-18) for samples produced with various substrate heating from ambient to 1000°C. It is shown that without heating, Anatase is the only phase present, and with heating above about 350°C, the Rutile phase begins to manifest and increasingly so with extra heating up to 1000°C, where the Rutile phase dominates. Stoichiometry has been determined for various  $\text{TiO}_2$  thin films by X-ray Photoelectron Spectroscopy (XPS) (19;20). It shows that with and without annealing at temperatures of up to 500°C, the films remain fully or very nearly fully stoichiometric with a ratio of two atoms of Oxygen to every one atom of Titanium. SEM images have shown (20) that the microstructure of a  $\text{TiO}_2$  thin film can change from one of higher porosity to one of higher density when the oxygen partial pressure and total pressure decrease and the RF power (and thus sputtered particle kinetic energy) increase. Titanium oxide films of greatly varying conductivity have been presented (21;22). For  $\text{TiO}_2$ , a conductivity of  $9.4 \times 10^{-7} \Omega^{-1} \text{m}^{-1}$  was given, whilst for sub oxides of  $\text{TiO}_x$  where  $x = 0.75$  to 1.45, conductivities in the range  $3076 \Omega^{-1} \text{m}^{-1}$  to  $1111 \Omega^{-1} \text{m}^{-1}$  respectively were given. These correspond well with the conductivity of  $\text{TiO}$  which is stated as  $2500 \Omega^{-1} \text{m}^{-1}$ . Refractive index and extinction coefficient spectra have been published (17;23) and give wide variation depending on e.g. pressure, power and annealing temperature. At 600nm, refractive index has been shown to vary from 2.1 to 2.4, and extinction coefficient has been shown to vary from 0.001 to 0.016. This shows that the optical properties of thin  $\text{TiO}_2$  films are tuneable and offers great prospects for many types of device.

The work on DC sputtered films will now be presented. AFM images have shown (24;25) that the grain size for DC sputtered films can vary from about 40nm to an average of 143nm and can have a complex dependency on the temperature of the substrate during deposition. The crystallinity of thin TiO<sub>2</sub> films have been determined (26-29) by their XRD spectra. For films with substrate heating during deposition of up to 220°C, only the Anatase phase was observed. For films with substrate heating of 620K, a mixture of Anatase and Rutile phases were observed, where the ratio of the phases was seen to be dependent (in part) on the stoichiometry (which was controlled by the plasma emission), and the phase transforms entirely to Rutile by annealing at 1070K. Films produced by a pulsed (25kHz to 40kHz) DC supply show the Rutile phase with substrate temperature as low as 200°C. Stoichiometry of TiO<sub>2</sub> sputtered films has been determined from XPS spectra (30;31). For XPS measurements, the authors will generally use a ceramic or nonstoichiometric target, which has been shown to give higher deposition rates. It has been shown that sputtering from a nonstoichiometric target with a low oxygen mole fraction in the sputtering gas will yield a stoichiometric film, whilst for a higher oxygen fraction, there is a deviation from stoichiometry. The details observed by SEM show (32;33) a general (and often seen) columnar growth pattern and a rough surface (in the sub-microscopic range) of grains size of approximately 9.2nm for films deposited at room temperature and growing to approximately 46.2nm for films deposited at 220°C. A wide range of conductivities have been measured (24;25) for films under various conditions; effective multi layer films of TiO<sub>2</sub> with embedded Ti gave transparent films with high conductivity (relative to pure TiO<sub>2</sub>) in the range  $10\Omega^{-1}\text{m}^{-1}$  to  $1000\Omega^{-1}\text{m}^{-1}$ , films of thickness in the range 230nm to 450nm had a conductivity in the range  $0.3\Omega^{-1}\text{m}^{-1}$  to  $239\Omega^{-1}\text{m}^{-1}$  which was dependant on substrate temperature, deposition rate and weight percentage of Anatase phase. The optical characteristics of TiO<sub>2</sub> films in terms of their refractive index and

extinction coefficient have been studied (34;35) and have been shown to vary somewhat;  $n$  can vary from 2.43 to 2.58 with temperature and from 2.1 to 2.3 with oxygen mole fraction in the sputtering gas, and  $k$  can vary from 0.000 to 0.03 with temperature and from 0.002 to 0.002 with oxygen mole fraction in the sputtering gas. The majority of published work detailing the band gap type extracted as a parameter in the Tauc model assumes a particular value for the index  $n$ , usually either 0.5 or 2. As many films of sputtered  $\text{TiO}_2$  show some amorphicity, it is perhaps better to extract the real value of the parameter and then discuss it. The bandgap type has been obtained (36;37) as 0.5 (direct allowed) with a bandgap of 3.27eV at 300K (compared with other work the authors referenced giving between 3.02 and 3.54eV), and as 2 (indirect allowed) with a bandgap of 3.34eV to 3.39eV. Most authors usually obtain the index by plotting the data to the power of the index reciprocal; if the graph is linear, the index is correct and parameters can be obtained from the linear portion.

### **2.2.2. Nano Powder**

Surface morphology of nanoporous films has been studied by AFM and SEM (38;39), at two ranges of magnification and of two different types of samples; those with irregular space in  $\text{TiO}_2$  mass and those with irregular  $\text{TiO}_2$  mass in space (an analogy is a sponge for the former and a layer of granules for the latter). The sponge type films were made by using tetrabutylorthotitanate and polyethylene glycol (PEG) as a precursor and template, respectively, and the effect of the amounts of PEG and other complexing agents (such as diethanolamine) on the structure were observed. The SEM images show that pore size depends on the molecular weight of PEG used; 2.0 g PEG (1000)/100 ml gives a mean pore size of 186nm, whilst 4.0 g PEG (1000)/100 ml gives a mean pore size of 684nm. Changing the complexing agents changes the structure from large pores (using diethanolamine – DEA) to solid polycrystalline mass (using citrate

acid – H<sub>3</sub>L). The granule type films were produced by autoclaving a mixture of 40mg/ml Degussa P25/water at 200°C for between one and ten days. The suspension was then applied to a glass substrate via a simple doctor-blading method and sintered at 450°C for 30 min. The SEM images show that the homogeneity (in terms of particle size and roughness) of the films improves after longer times of autoclaving the suspension. The AFM images also show this, and show a particle size in the region of 80nm. Roughness values were in the region of 20nm and were highest for nonautoclaved P25. Conductivities for different samples of nanoparticle films have been studied for their electrical characteristics (40;41). Nanoporous films of TiO<sub>2</sub> were manufactured by a chemical method and some were annealed in hydrogen at 400°C for 15minutes to create oxygen vacancies. The average particle size was in the range of 10nm to 15nm. The conductivities of as-prepared samples and annealed samples were measured and were found to be dependent on temperature, with the as-prepared sample having a room temperature conductivity of  $1.3\Omega^{-1}\text{m}^{-1}$ , and the annealed sample having a room temperature conductivity of  $0.040\Omega^{-1}\text{m}^{-1}$ . The conductivities at higher temperature (673K) became similar. Films of nanoporous TiO<sub>2</sub> of 50% porosity and particle size in the range 10nm to 15nm have been made by in-house synthesis and studied for photoconductivity in under various conditions. Resistivity was found to be in the order of  $10^4\Omega\text{m}$  to  $10^6\Omega\text{m}$  in dark and in ambient air. This falls by  $10^2$  to  $10^3$  times when measured under vacuum which the authors tentatively attribute to removal of water which may dope the film with protons. Photoconductivity is  $10^6$  times larger in vacuum than in air and increases with decreasing pressure, which the authors attribute to the loss of surface adsorbed oxygen. The authors used a 75W xenon lamp for illuminating the samples.

### 2.3. Dyes and Other Layers

The dye is the layer that absorbs the light, although only a portion of the solar spectrum is actually absorbed due to an incomplete absorption spectrum that occurs in most dyes.

Published work on the dyes used in this research is presented below.

#### 2.3.1. CuPc, Rose Bengale, poly(9-vinylcarbazole) (PVK)

Absorption spectra of various Metal Phthalocyanines have been studied in different chemical and physical environments. Dyes in solution, such as that shown in fig 2.1 (42), may have quite narrow peaks, with CuPc being more absorbent near the main peak, whereas dyes spun coated, such as that shown in fig 2.2 (42), may be much broader with a greatly diminished main peak.

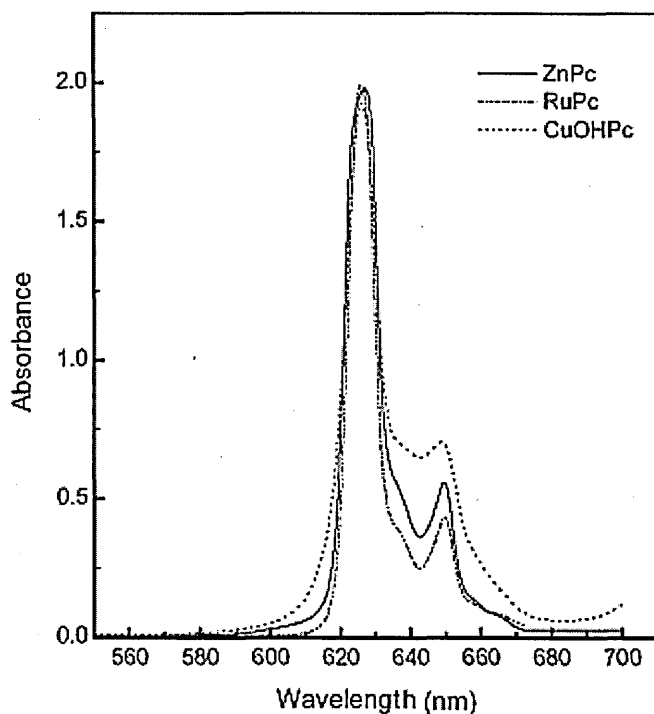


Figure 2.1. Metal Phthalocyanines in solution with chloroform (concentration of  $3.3\text{mg ml}^{-1}$ )

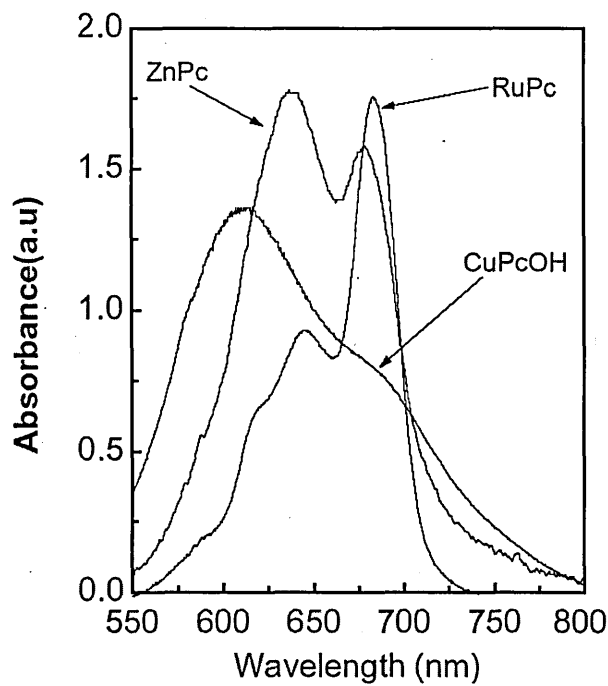


Figure 2.2. UV-Vis spectra of Spin coated films of Metal Phthalocyanines about 100nm thick

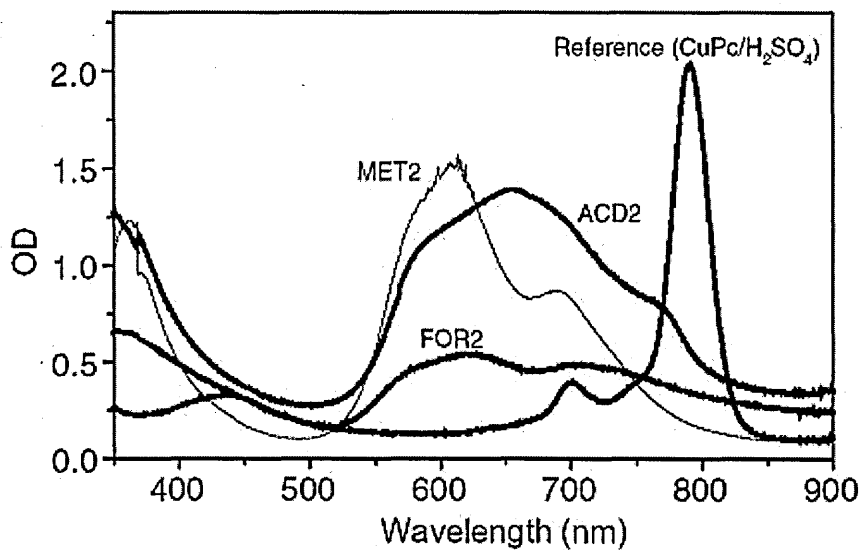


Figure 2.3 UV-VIS absorption spectra for CuPc-SiO<sub>2</sub> composites with different chemical processing. Reference of CuPc dissolved in H<sub>2</sub>SO<sub>4</sub> shown.

Absorption spectra of various Metal Phthalocyanines have been studied in different composites and solvents such as H<sub>2</sub>SO<sub>4</sub> and give results such as that in fig 2.3 (43).

H<sub>2</sub>SO<sub>4</sub> shifts the main absorbance peak to the right by about 150nm relative to CuPc in Chloroform. The environment that the dye is in clearly changes its optical

characteristics, and it can be worth studying a dye deposited on different layers to determine the properties of the dye as part of a device in addition to the dye in isolation.

Absorption spectra of Rose Bengale in different environments have been studied and give results such as that fig 2.4 (44). It was seen that the spectrum of Rose Bengal dissolved in water is quite different from that adsorbed onto a polymer (mostly in terms of the relative peak heights and shapes - not the overall height difference which is mostly due to the light passing through a different amount of dye).

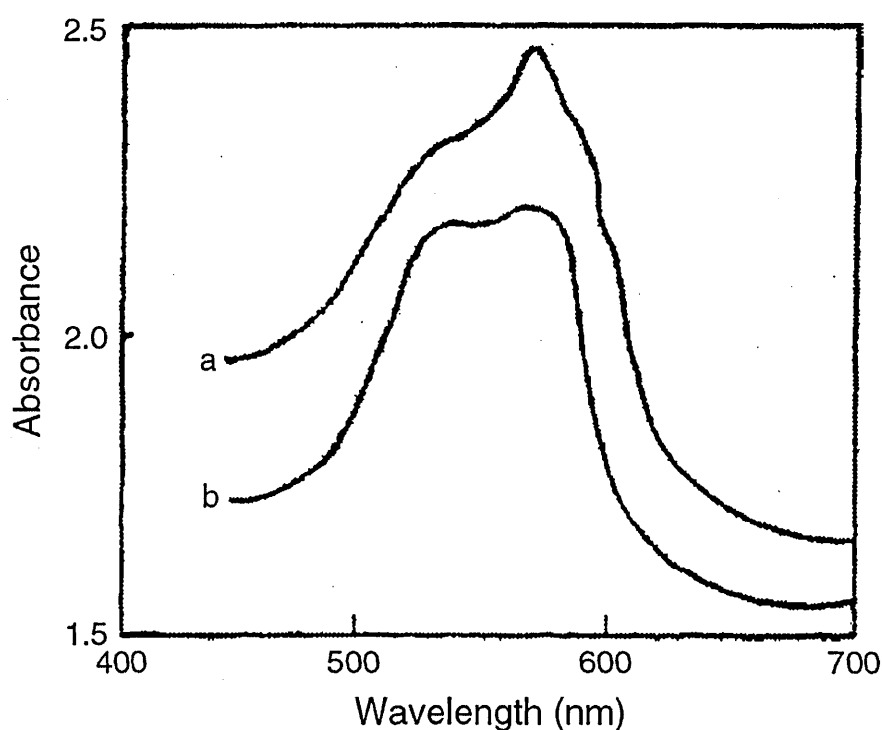


Figure 2.4. UV/VIS spectra of (a) Rose Bengal in water and (b) Rose Bengal bound to poly(N-vinylpyrrolidone).

The measured spectrum of Rose Bengal in ethanol in fig 2.5 (45) is quite different from that in plain water - the main peak of the spectrum in ethanol is much higher than that in water. As with the CuPc studies, it is seen that the environment of the dye changes its optical characteristics significantly. PVK is visually transparent and thus, absorption spectra are uninteresting for PVK.

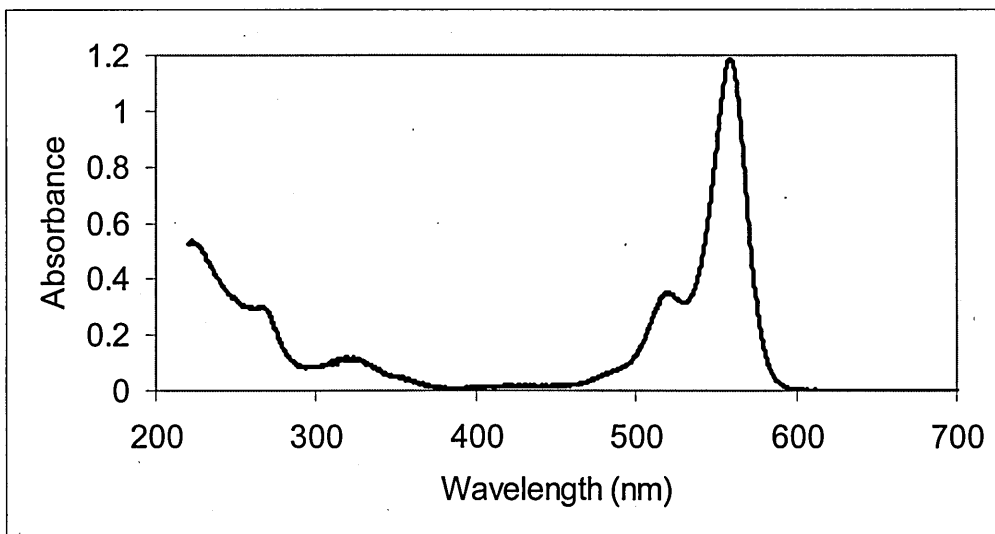


Figure 2.5. UV-Vis spectrum of Rose Bengal in ethanol

The electrical conductivity of CuPc and its dependency on gaseous atmosphere and temperature has been studied (46) and has been found to vary from  $10^{-7}\Omega^{-1}\text{m}^{-1}$  to  $10^{-4}\Omega^{-1}\text{m}^{-1}$ , rising with temperature. Activation energy,  $E_a$ , varied with atmosphere from 0.54eV to 1.1eV. Another study (47) which used a CuPc layer as a electrical gas sensing element by thermally evaporating CuPc onto an interdigitated electrode, gave an electrical conductivity of about  $250 \times 10^{-6}\Omega^{-1}\text{m}^{-1}$ , which rose by 75 times when exposed to 3 parts per million of  $\text{NO}_2$ , and is the same range as the previous study.

Little work could be found that described the conductivity of PVK (which is actually quite a commonly used hole transport material in dye sensitised solar cells), but one study (48) showed a temperature dependence of conductivity, but the response was such that at room temperature, the conductivity was in the order of  $10^{-15}\Omega^{-1}\text{m}^{-1}$  which seems unreasonable. Rose Bengal is used often in medicine to detect damage to the eye (bad areas are stained while good areas are not). Its use in physics research is fairly new, and as such, electrical conductance studies are rare.

### 2.3.2. Other Commonly Used Chemicals

Out of the over 100 dyes used for solar cells, by far the most common dyes that scientists use are based on a Ruthenium complex (with the most common complex being cis-dithiocyanato-bis[2,2'-bipyridyl 4,4'-dicarboxylate] Ru(II)). The Ru dyes strongly absorb light in low wavelengths, (unlike CuPc and Rose Bengal), but cost around £2000 per gram (49). Other dyes used include porphyrin (50), Chlorophyll (51), and Santalin (52) from sandalwood. The electrolytes used in 'wet' cells have advantages and disadvantages; on one hand they give great penetration of the porous dye-covered layers with subsequent high extraction of carriers and good conversion efficiency, but on the other hand they are toxic, and prone to leak out of the cell even if it is sealed (over time any sealant will degrade and crack) and the cell may break (it is made of glass after all) and spill the electrolyte onto the ground or into the loft space of a house it is installed on. Such spillage could be disastrous. Many scientists have tried to use a thicker form of electrolyte or to dispense with an electrolyte altogether and apply a solid (as a solution that dries leaving the material penetrating the pores) conducting layer to carry away the photogenerated holes. Examples of such hole conducting layers are; poly(3-octylthiophene) (P3OT) (53), Copper Iodide (52), poly[3-(11 diethylphosphoryl-undecyl) thiophene] (abbrev. P3PUT), poly(4-undecyl-2,2'-bithiophene), (abbrev. P4UBT), poly(3-undecyl-2,2'-bithiophene) (abbrev. P3UBT) (54).

### 2.4. Light Modulation

Application of pulses of light to a sample is a common way of exciting the sample. As such, there is a plethora of ways of producing light from mechanical modulators like choppers that intermittently interrupt a light source, to pulsed LEDs that operate in the tens of picoseconds time regime. The time regime needed will depend on the type of sample and type of measurement. A selection of equipment capable of producing pulses

of light in different time regimes and in different ways is shown in table 2.1, to give the reader a better appreciation of the range of capabilities, technologies and cost of various commercial light pulse generators. The data was mostly obtained from company websites and technical queries. Lifetimes of Titanium oxides have been shown (55;56) to vary across several orders of magnitude from nanoseconds to microseconds (dependent on such parameters as Platinum doping level), and lifetimes in other semiconductors have been shown (57) to vary from 1ps to 10ns (depending on doping levels of Zinc and Carbon). Clearly, if one system is to be able to study all types of samples, it must be able to deal with at least six orders of magnitude of variance in lifetime. Lifetimes have been measured by various means including photoluminescence and the Time Resolved Photocharge (TRPC) method.

Table 2.1. A review of a selection of commercial optical modulators

Manufacturer	Technology	Pulse dimensions	Power	Variability
Melles Griot	mechanical iris shutter	16.7us cut-off	n/a	Use any light source including diverging beam from monochromator
Optical Choppers	rotating slotted disk (6000rpm)	31us cut-off	n/a	Use any light source including diverging beam from monochromator
Optical Choppers	rotating slotted disk (50000rpm)	3.8us cut-off	n/a	Use any light source including diverging beam from monochromator
Oriel	flash lamp	1.6us pulse	16W	flash frequency (approx £300 each)
Oriel	flash lamp	9us pulse	60W	flash frequency (approx £200 each)
IBH	flash lamp	100ps to 100us pulse		flash frequency
IBH	xenon flash lamp	120ns pulse		flash frequency
Edinburgh Instruments	flash lamp	1ns pulse		flash frequency, fillable with desired gas
IBH	Pulsed LED	0.9ns pulse		various spectra from UV to near IR
IBH	Pulsed LED	1us to 1s pulse		various spectra from UV to near IR
IBH	Pulsed LED	100ps pulse		various spectra from UV to near IR
PicoQuant	Pulsed LED	approx 50ps pulse		various spectra
PicoQuant	Pulsed LED	<1ns pulse		various spectra
PicoQuant	Pulsed LED	3ns to 100ns pulse	20mW	various spectra
Edinburgh Instruments	Pulsed LED	750ps pulse, up to 40MHz	approx 0.1mw	various spectra. Approx £1000 per LED, £6000 for the driver unit
Edinburgh Instruments	Pulsed diode lasers	approx 50ps pulse		various spectra

## Reference List

- (1) Tennakone K, Jayaweera PVV, Bandaranayake PKM. Journal of Photochemistry and Photobiology A: Chemistry 2003; 158(2-3):125-130.
- (2) Keis K, Bauer C, Boschloo G, Hagfeldt A, Westermarck K, Rensmo H et al. Journal of Photochemistry and Photobiology A: Chemistry 2002; 148(1-3):57-64.
- (3) Nevin W, Chamberlain G. IEEE Transactions on Electron Devices 1993; 40(1):75.
- (4) Nogueira AF, De Paoli MA. Solar Energy Materials and Solar Cells 2000; 61(2):135-141.

- (5) Hara K, Horiguchi T, Kinoshita T, Sayama K, Sugihara H, Arakawa H. *Solar Energy Materials and Solar Cells* 2000; 64(2):115-134.
- (6) Regan B, Gratzel M. *Nature* 1991; 353:737.
- (7) Tracey S, Ray A, Shishiyanu T. *IEE Proceedings* 1998; 145(5):383.
- (8) Senadeera GKR, Jayaweera PVV, Perera VPS, Tennakone K. *Solar Energy Materials and Solar Cells* 2002; 73(1):103-108.
- (9) Fan Q, McQuillin B, Bradley DDC, Whitelegg S, Seddon AB. *Chemical Physics Letters* 2001; 347(4-6):325-330.
- (10) Yeon Song M, Kim KJ, Kim DY. *Solar Energy Materials and Solar Cells* 2005; 85(1):31-39.
- (11) Boschloo G, Lindstrom H, Magnusson E, Holmberg A, Hagfeldt A. *Journal of Photochemistry and Photobiology A: Chemistry* 2002; 148(1-3):11-15.
- (12) Frank J, Kopidakis N, Lagemaat Jvd. *Coordination Chemistry Reviews* 2004; 248(13-14):1165-1179.
- (13) Hagfeldt A, Boschloo G, Lindstrom H, Figgemeier E, Holmberg A, Aranyos V et al. *Coordination Chemistry Reviews* 2004; 248(13-14):1501-1509.
- (14) Grant CD, Schwartzberg AM, Smestad GP, Kowalik J, Tolbert LM, Zhang JZ. *Synthetic Metals* 2003; 132(2):197-204.
- (15) Mardare D, Rusu GI. *Materials Science and Engineering B* 2000; 75(1):68-71.
- (16) Jeong B-S, Budai JD, Norton DP. *Thin Solid Films* 2002; 422(1-2):166-169.
- (17) Amor SB, Guedri L, Baud G, Jacquet M, Ghedira M. *Materials Chemistry and Physics* 2003; 77(3):903-911.
- (18) Hiratani M, Kadoshima M, Hirano T, Shimamoto Y, Matsui Y, Nabatame T et al. *Applied Surface Science* 2003; 207(1-4):13-19.
- (19) Chow LLW, Yuen MMF, Chan PCH, Cheung AT. *Sensors and Actuators B: Chemical* 2001; 76(1-3):310-315.
- (20) Ben Amor S, Baud G, Jacquet M, Pichon N. *Surface and Coatings Technology* 1998; 102(1-2):63-72.
- (21) Banakh O, Schmid PE, Sanjines R, Levy F. *Surface and Coatings Technology* 2002; 151-152:272-275.
- (22) Mardare D, Rusu GI. *Materials Science and Engineering B* 2000; 75(1):68-71.
- (23) Amor SB, Baud G, Besse JP, Jacquet M. *Materials Science and Engineering B* 1997; 47(2):110-118.
- (24) Mardare D, Baban C, Gavrilă R, Modreanu M, Rusu GI. *Surface Science* 2002; 507-510:468-472.

- (25) Springer SG, Schmid PE, Sanjines R, Levy F. *Surface and Coatings Technology* 2002; 151-152:51-54.
- (26) Radecka M, Zakrzewska K, Brudnik A, Posadowski W. *Thin Solid Films* 1999; 343-344:152-155.
- (27) Lapostolle F, Huu Loi T, Billard A, Frantz C. *Surface and Coatings Technology* 1997; 97(1-3):574-581.
- (28) Treichel O, Kirchhoff V. *Surface and Coatings Technology* 2000; 123(2-3):268-272.
- (29) Takeda S, Suzuki S, Odaka H, Hosono H. *Thin Solid Films* 2001; 392(2):338-344.
- (30) Ohsaki H, Tachibana Y, Mitsui A, Kamiyama T, Hayashi Y. *Thin Solid Films* 2001; 392(2):169-173.
- (31) Tomaszewski H, Poelman H, Depla D, Poelman D, De Gryse R, Fiermans L et al. *Vacuum* 2002; 68(1):31-38.
- (32) Takeda S, Suzuki S, Odaka H, Hosono H. *Thin Solid Films* 2001; 392(2):338-344.
- (33) Viseu TMR, Almeida B, Stchakovsky M, Drevillon B, Ferreira MIC, Sousa JB. *Thin Solid Films* 2001; 401(1-2):216-224.
- (34) Vergohl M, Malkomes N, Staedler T, Matthee T, Richter U. *Thin Solid Films* 1999; 351(1-2):42-47.
- (35) Tomaszewski H, Poelman H, Depla D, Poelman D, De Gryse R, Fiermans L et al. *Vacuum* 2002; 68(1):31-38.
- (36) Miao L, Jin P, Kaneko K, Terai A, Nabatova-Gabain N, Tanemura S. *Applied Surface Science* 2003; 212-213:255-263.
- (37) Dannenberg R, Greene P. *Thin Solid Films* 2000; 360(1-2):122-127.
- (38) Kontos AI, Arabatzis IM, Tsoukleris DS, Kontos AG, Bernard MC, Petrakis DE et al. *Catalysis Today* 2005; 101(3-4):275-281.
- (39) Bu SJ, Jin ZG, Liu XX, Yang LR, Cheng ZJ. *Journal of the European Ceramic Society* 2005; 25(5):673-679.
- (40) Madhusudan Reddy K, Manorama SV, Ramachandra Reddy A. *Materials Chemistry and Physics* 2003; 78(1):239-245.
- (41) Eppler AM, Ballard IM, Nelson J. *Physica E: Low-dimensional Systems and Nanostructures* 2002; 14(1-2):197-202.
- (42) Spadavecchia J, Ciccarella G, Vasapollo G, Siciliano P, Rella R. *Sensors and Actuators B: Chemical* 2004; 100(1-2):135-138.
- (43) Litran R, Ramirez-del-Solar M, Blanco E. *Journal of Non-Crystalline Solids* 2003; 318(1-2):49-55.

- (44) Gigimol M, Mathew B. *Polymer International* 2003; 52:973-980.
- (45) Du H, Fuh R, Li J, Corkan A, Lindsey J. *Photochemistry and Photobiology* 1998; 68:141-142.
- (46) Zhivkov I, Spassova E, Dimov D, Danev G. *Vacuum* 2004; 76(2-3):237-240.
- (47) Newton MI, Starke TKH, Willis MR, McHale G. *Sensors and Actuators B: Chemical* 2000; 67(3):307-311.
- (48) Tayyan A, Khogali A. *CHINESE JOURNAL OF PHYSICS* 2004; 42(4):392-400.
- (49) <http://www.solaronix.com/products/Chemicals/specialty.html>. accessed June 2005.
- (50) Ma T, Inoue K, Noma H, Yao K, Abe E. *Journal of Photochemistry and Photobiology A: Chemistry* 2002; 152(1-3):207-212.
- (51) Kumarasinghe AR, Flavell WR. *Journal of Photochemistry and Photobiology A: Chemistry* 2002; 148(1-3):145-151.
- (52) Tennakone K, Kumara GRRA, Kottegoda IRM, Perera VPS, Weerasundara PSRS. *Journal of Photochemistry and Photobiology A: Chemistry* 1998; 117(2):137-142.
- (53) Gebeyehu D, Brabec CJ, Sariciftci NS, Vangeneugden D, Kiebooms R, Vanderzande D et al. *Synthetic Metals* 2001; 125(3):279-287.
- (54) Smestad GP, Spiekermann S, Kowalik J, Grant CD, Schwartzberg AM, Zhang J et al. *Solar Energy Materials and Solar Cells* 2003; 76(1):85-105.
- (55) Wilke K, Breuer HD. *Journal of Photochemistry and Photobiology A: Chemistry* 1999; 121(1):49-53.
- (56) Kim SC, Heo MC, Hahn SH, Lee CW, Joo JH, Kim JS et al. *Materials Letters* 2005; 59(16):2059-2063.
- (57) Cui D, Hubbard S, Pavladis D, Eisenbach A, Chelli C. *Semicond Sci Technol* 2002; 17:503-509.

## Theoretical Background

---

### 3.1. Structural characteristics

This section describes the structural aspects of materials, such as what is meant by crystallinity, and what may be seen at different levels of magnification. There is sufficient depth that the reader may better understand the presented results in chapter 5.

#### 3.1.1. Crystallographic Phase

A crystal is a solid, and a periodic arrangement of atoms or molecules that is comprised of repeated instances of a basic "unit cell", in three dimensions (1). Not all solids are crystalline; glass for example is amorphous and shows no periodicity in its atomic layout. Many solids are comprised of a mosaic of crystals with different orientations to one another, but each crystal will have periodicity matching the periodicity of the rest of the crystals. A solid comprised of a single crystal (like a silicon wafer made for the IC industry) is termed "monocrystalline", while one that is comprised of many crystals (like cast iron) is termed "polycrystalline". Each crystalline material will arrange in a very specific way. For example, some crystals arrange such that each atom or molecule lies at the corners of a cube, while others arrange such that each atom or molecule lies at the corners or centre of a cuboid. The specific way that a crystalline material arranges is known as its 'phase'. Some materials can exist in more than one phase, with  $\text{TiO}_2$  being a good example.

There are seven different crystal systems; cubic (three axes, all equal length), tetragonal (three axes, two equal length), orthorhombic (three axes, non equal length), rhombohedral (three axes, equal length, equal angles of inclination), monoclinic (three unequal axes, one angle not a right angle), triclinic (three unequal axes none at right angles), and hexagonal (two equal coplanar axes at  $120^\circ$ , third (not equal) at right angles). Some systems are subdivided into other types due to additional atoms at the base centre, face centre, or body centre. In total there are 14 lattice types collectively known as the Bravais Lattices, each of which define not only the lattice structure (in terms of relative positions and parameters) but also the unit cells that make up the lattices. Two examples of unit cells are given in fig 3.1, with the important lattice parameters shown. The type of unit cell and the particular values of the lattice parameters define the phase of a material. The lengths of the sides of the cell and internal angles are labelled  $a$ ,  $b$ ,  $c$ ,  $\alpha$ ,  $\beta$ ,  $\gamma$ , respectively.

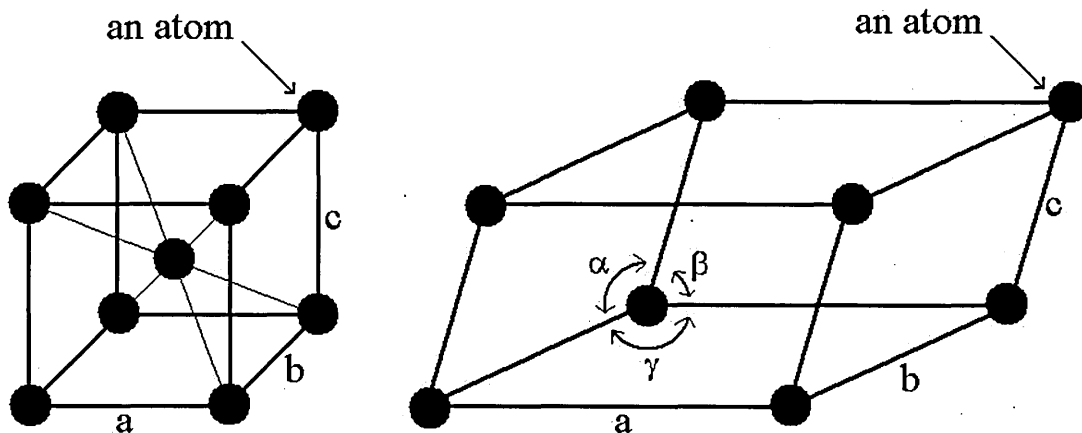


Figure 3.1. Body-centred orthorhombic (left) and triclinic (right).

The atoms in a lattice form planes that will diffract incoming X-Ray beams at certain directions, in a vaguely similar manner to a mirror (this is explained in detail later). Each plane has its orientation defined by a set of numbers called Miller Indices (the indices are labelled  $[hkl]$  for a 3D lattice). Each Miller Index is equal to the reciprocal of the fraction of the point of intersection of the plane to an axis, to the length of the

axis. Negative values having a bar placed above the index. It is better explained by the following relation;

$$\text{Miller Index} = \frac{\text{axis length}}{\text{point of intercept}} \quad (3.1)$$

If a plane lies parallel to an axis, it will never cross it, so the point of intercept is infinity, and the corresponding index is zero. Each lattice type has an associated equation relating the miller indices, the interplanar thickness and the dimension of the unit cell. A selection is given below;

Cubic: 
$$\frac{1}{d^2} = \frac{h^2 + k^2 + l^2}{a^2} \quad (3.2)$$

Tetragonal: 
$$\frac{1}{d^2} = \frac{h^2 + k^2}{a^2} + \frac{l^2}{c^2} \quad (3.3)$$

Orthorhombic: 
$$\frac{1}{d^2} = \frac{h^2}{a^2} + \frac{k^2}{b^2} + \frac{l^2}{c^2} \quad (3.4)$$

A selection of planes through a simple lattice, each plane being parallel to the z-axis in the page, is shown in fig 3.2. It is obvious that as the angle of the plane changes from flat to a large angle, the distance between the planes (interplanar distance) decreases.

This is proved later.

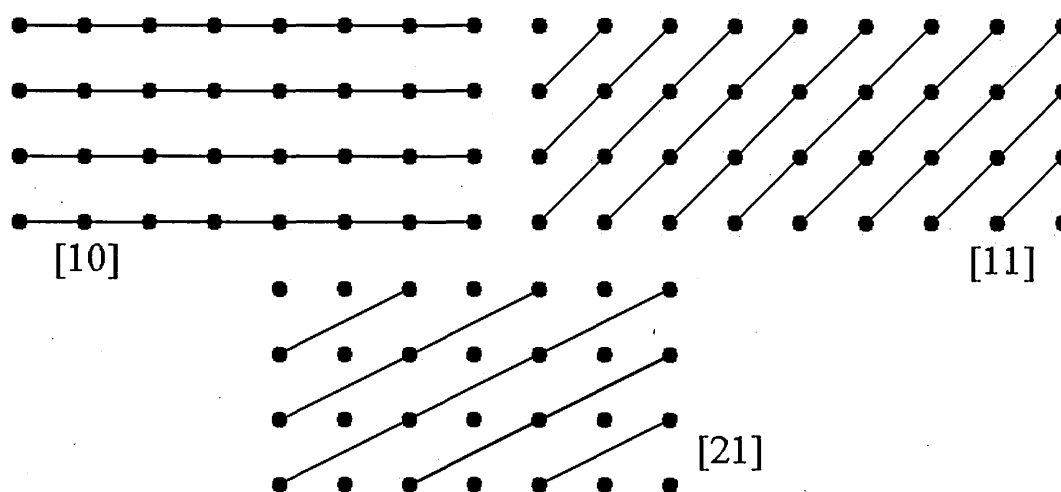


Figure 3.2. Three examples of atomic planes in the same lattice with indices shown.

### 3.1.2. Microscopic and Nanoscopic Details

Microscopic details are those that have a size in the order of micrometres. Such details may include specks of dust or pollen on the sample surface or trapped within one of the layers, or tiny cracks and fissures or 'pinholes' that are beyond the range of human eyesight. The presence of such details can be devastating to the operation of a device especially those whose layers are thinner than the detail's size. A speck of dust can blot out many hundreds of devices in a modern VLSI circuit, and may destroy the order of a very thin multi layer device possibly causing device failure. Nanoscopic details are those that have a size range in the order of nanometres (sub-micrometer). Such details may include individual grains in a polycrystalline sample, or the step at the start of a layer on a substrate. Details at these size ranges are not visible through an ordinary optical microscope. There exist other types of microscope, such as the atomic force microscope that can allow an observer to observe details in the nanometre size range.

If details such as dust specks are seen *in* a sample, then this can be indicative of poor sample preparation due to insufficient air filtering in a clean room for example. A network of fine cracks can be the result of excess shrinkage when a sample is annealed in an oven. A qualitative analysis of the porosity of a powder sample may be made at this range. The size of the grains can have a significant effect on the properties of a device, so to know the grain size distribution of a sample can be useful in identifying reasons for certain characteristics of some data. The presence of nanoscopic particles of one material in another, smooth or amorphous material can show up in nanoscopic analysis.

### **3.1.3. Stoichiometry**

Stoichiometry is the study of the ratios of elements in a reaction to balance the chemical equation. In the case of this research, the stoichiometry just refers to the ratio of elements in a sample i.e. 2 moles of Oxygen for every 1 mole of Titanium will produce a sample of Titanium Dioxide with correct stoichiometry, and the sample can be said to be stoichiometric.

If the sample has incorrect stoichiometry, then its properties can change considerably. Excess Titanium will make the film appear shiny and darker, reducing the amount of light that penetrates it (while at the same time increasing the conductivity). Excess Oxygen can lead to trapping of electrons, and because the  $\text{TiO}_2$  side of the solar cell is where the photogenerated electrons move to, any trapping effects will reduce the efficiency of the cell.

## **3.2. Electrical Characteristics**

This section describes the electrical aspects of materials and device, such as how the heterojunction solar cell differs from the homojunction solar cell, and how the diode model parameters are extracted by a fitting algorithm.

### **3.2.1. Conventional Solid State Solar Cell**

Conventional solar cells are made of a homojunction device, which is to say that it is from one piece of material that the junction and the areas to each side are made (2). Assuming that a silicon wafer cell (the most common type) is being studied, the junction is made by heavily doping one side n-type (electrons are the majority carriers), and doping the other side p-type (holes are the majority carriers). A schematic (not to scale) diagram of a homojunction is shown in fig 3.3.

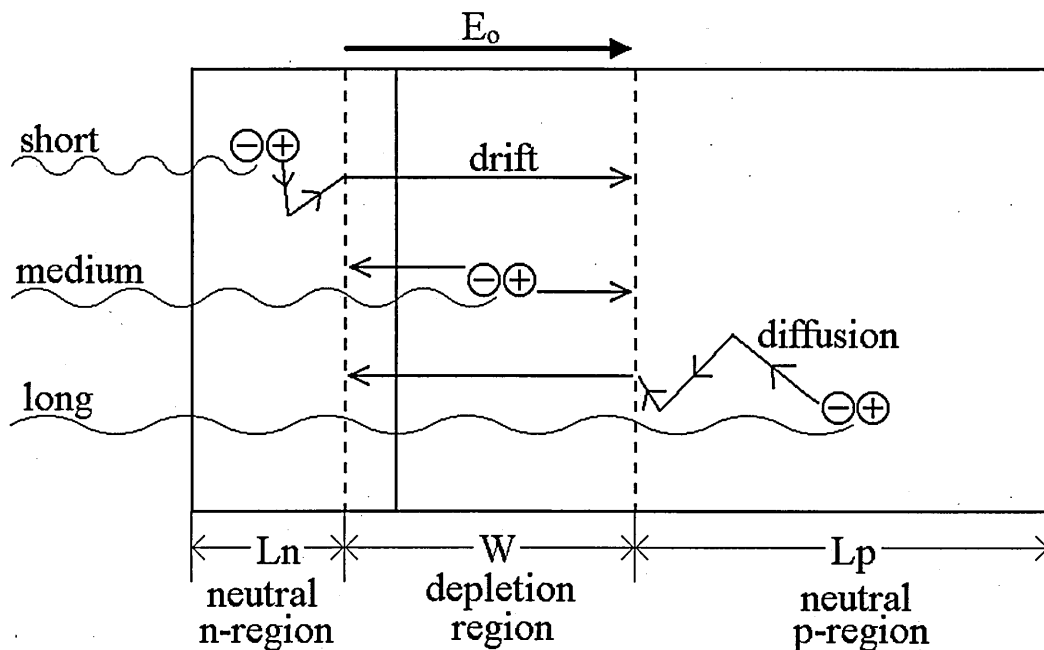


Figure 3.3. A schematic diagram of a silicon solar cell showing carrier transport.

The sunlight is incident on the n side and photons can be absorbed in the n region if they are short wavelengths, in the depletion region (the area depleted of carriers) if they are of medium wavelength, or in the p-region if they are of long wavelength. The place where the photons are absorbed is not some fixed distance, but a most probable distance based on the likelihood of absorption (shorter wavelengths will be absorbed with a high probability and so will tend to be absorbed after a shorter journey, hence, in the n-region). When a sufficiently energetic photon is absorbed, an electron-hole pair is created and the electron will diffuse to the boundary with the depletion layer before drifting across (due to the built in potential created by the ionised atoms from which carriers have been removed) to the n-region, to make it more negative and vice versa for the holes. A voltage (called the photovoltage) is thus produced across the terminals of the device, which may be connected to a load to do work. Any accumulated electrons in the n-region will travel through the load to recombine with the holes in the p-region. The smaller the load, the more current will be supplied by the device, but this lowers the photovoltage as the carriers producing the voltage are being removed by the load. The

n-region is heavily doped so as to make it thinner than the p-region, as the photogenerated holes diffuse a shorter length before recombination compared to the electrons and vice-versa.

### **3.2.2. Dye Sensitised Solar Cell**

A deep theoretical analysis of the function of a heterojunction will not be presented here, as it is not within the scope of this work. Instead, a summary of the theory presented by previous Ph.D. research (3) will be described. This will give the reader sufficient understanding of the workings of the heterojunction to better understand the results and the implications of them.

The adsorbed dye is photoexcited by an incident photon and produces a free electron, which will diffuse to the junction and is then injected into the conduction band of the semiconductor it is deposited on, leaving behind a free hole in the valence band of the dye. Electrons coming back from the load may fill these holes. Direct photogeneration of the electron is rare in Phthalocyanines, and it is most likely that the absorbed photon produces a loosely bound electron that can dissociate at a free surface, or at an internal dissociation point such as an impurity. In a typical heterojunction cell, there may be several current transfer mechanisms occurring in addition to the injection, such as generation-recombination, and recombination at interface states at the junction.

The semiconductor in the case of all dye sensitised work is transparent in the visible region, and will therefore absorb only a very small amount of sunlight - that of low wavelength (below around 300nm), meaning the dye must absorb as much light as possible. This is quite different to the homojunction cell described above, where all of the device thickness can contribute to light absorption. Dyes tend to absorb in tight

bands of wavelength, so to absorb most of the light, several dyes must be used (either simply mixed together or made up as a tandem cell).

Band diagrams of separate n and p materials ( $\text{TiO}_2$  and  $\text{CuPc}$  respectively in this case) and joined n and p materials are shown in fig 3.4 and fig 3.5 respectively. It was assumed that the electron affinity of the n type material was greater than that for the p type material. When the materials are joined (when the  $\text{CuPc}$  is deposited on the  $\text{TiO}_2$  surface), the Fermi levels shift such that they coincide. This shifts the rest of the energy levels forming a step in the bands. The built-in potential that is created by the union of n and p materials is given by the difference in the work function ( $\phi_p - \phi_n$ ) of the two materials.

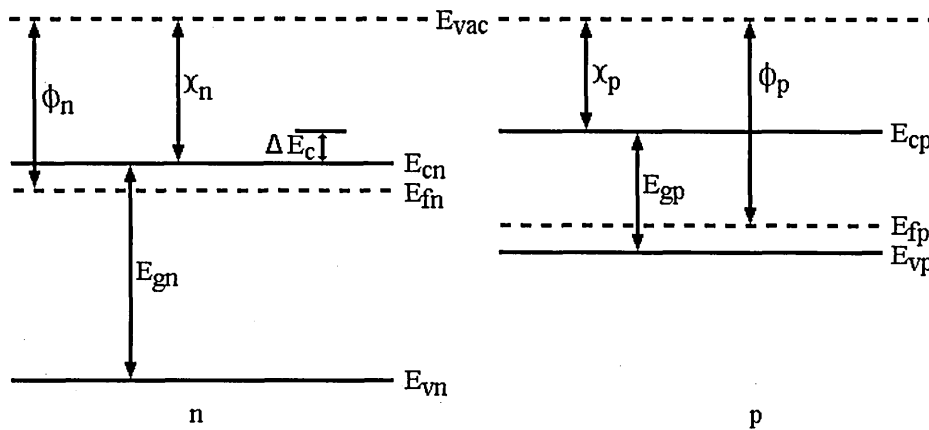


Figure 3.4. Isolated n and p type materials.

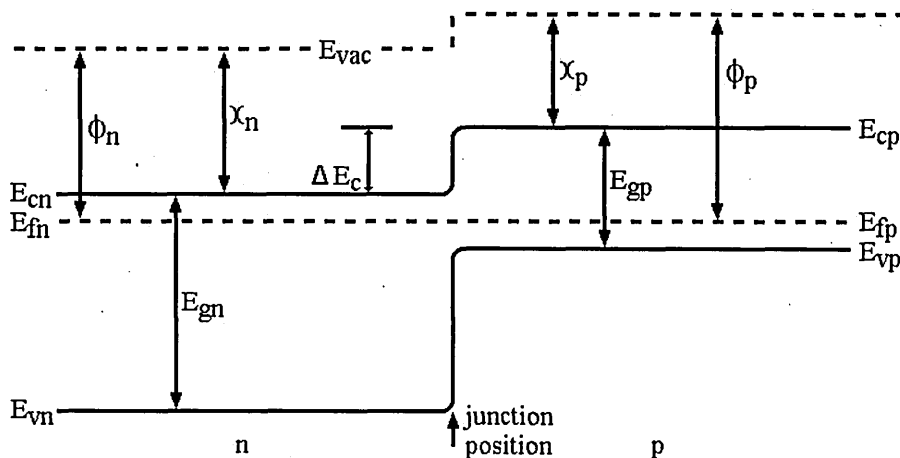


Figure 3.5. Joined n and p materials forming a heterojunction at the position shown

A photovoltaic cell acts as a diode in parallel with a current generator that is light intensity dependent. This gives the cell diode-like characteristics with a negative current offset due to the photovoltaic effect. By varying the load that the cell is connected to, the cell output can be varied from zero voltage with maximum current (giving  $I_{sc}$  with short circuit load) to zero current with maximum voltage (giving  $V_{oc}$  with open circuit load), both extreme states giving no power to the load, as the power is the product of current and voltage. At any other load resistance, the power will be non-zero and at some load value, there will be a maximum power delivered to the load. The ratio of the maximum output power to the product of  $I_{sc}$  and  $V_{oc}$  is termed the fill factor of the device. A low fill factor will limit the efficiency.

The fill factor can be calculated by inducing a photovoltage in a cell, connecting it to a variable load, and then measuring the photovoltage at different loads. The photocurrent (usually a much smaller value than photovoltage) can then be calculated and the maximum power can be obtained, and the fill factor determined. An example of this process is shown in fig 3.6 for simulated data.  $V_{oc} = 0.502V$ ,  $I_{sc} = 100\mu A$ ,  $V_{work} = 0.428V$ ,  $I_{work} = 94.3\mu A$ , giving a fill factor value of 0.804, or 80.4%. The best load is  $4.54k\Omega$ . This means that when this cell is illuminated, only 80.4% of all the available electrical energy it produces can be used. The fill factor for many devices is much less than this.

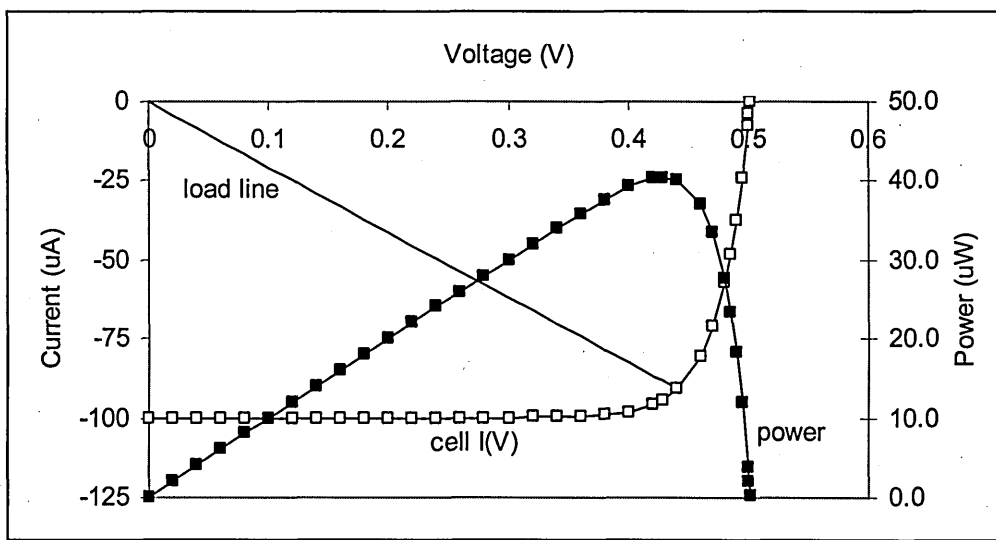


Figure 3.6. Simulated cell response with varying load. Load line at maximum power shown.

It was believed that the heterojunction cell had the same current-voltage model (and thus the same equivalent circuit) as the homojunction cell, also incorporating series and parallel resistance and ideality factor, and this model is shown below.

### 3.2.3. Diode Model Fitting

A simple PN junction (a device comprised of a semiconductor where one half is doped with acceptor impurities - p type, and the other half is doped with donor impurities - n type) has electrical characteristics that can be described by the universal diode equation;

$$I = I_s \left[ \exp\left(\frac{qV}{nkT}\right) - 1 \right] \quad (3.5)$$

where V is the voltage across the PN junction,  $I_s$  is the reverse saturation current, k is the Boltzmann constant, n is the ideality factor, T is the ambient temperature, and q is the electron charge.

A real solar cell has a photovoltaic current and some resistance that is in series with the cell, and therefore the basic diode equation must be modified as follows (2);

$$I = -I_{ph} + I_s \left[ \exp\left(\frac{q(V - IR_s)}{nkT}\right) - 1 \right] \quad (3.6)$$

where  $I_{ph}$  is the generated photovoltaic current, and  $IR_s$  is the voltage drop across the series resistance  $R_s$ . Solar cells have a parallel resistance that manifests itself as a linearly changing current in the negative bias quadrant. It will be shown that  $R_s$  has a detrimental effect on the quality of the solar cell.

There is a resistance,  $R_p$ , in parallel with the device and the effect of this (when it dominates) is to make the cell look like a resistor of value  $R_p$ .  $R_p$  can be determined as the reciprocal of the gradient of the  $I(V)$  graph in the negative voltage range. Similarly,  $R_s$  can be determined (though with somewhat more difficulty) as the reciprocal of the gradient of the  $I(V)$  spectra in the positive voltage range when it tends towards linearity. The values of  $n$  and  $I_s$  can be found by taking natural logs of the  $I$  values, and plotting against  $V$ , which will result in a plot that tends towards linear. The gradient of the linear section of the plot yields  $q/nkT$ , and the intercept yields natural log of  $I_s$ .

Whilst the above procedure for extracting the parameters of the model works fairly well with error-free data and with the parameters meeting certain criteria, a much better method is to perform the extraction by a curve fitting procedure. Such a procedure has been developed for this research (to be known as the Vale diode model fitting method). An alternative equation relating  $V$  and  $I$  must be used to generate data from the chosen parameters for the fitting procedure (2);

$$V = \left( \frac{nkT}{q} \right) \times \ln \left[ \frac{(I + I_{ph} + I_s)}{I_s} \right] + R_s I \quad (3.7)$$

This form must be used as the original had the term  $I$  on both sides of the equation. The procedure works by observing changes in a graph of the difference between the fitted and original graphs, when the parameters are changed. A change in  $n$  makes the difference graph non-linear (this is due to the fact that one curve minus a second curve of the same family creates a third curve of the same family). A change in  $I_s$  creates a

constant shift in direction of the I-axis. A change in  $R_s$  creates a shift in the direction of the I-axis linearly dependent on V. By sweeping through each parameter until its effect is nullified, the parameters are determined. This has been thoroughly tested with parameters over several orders of magnitude, and with three levels of random error (from 0% to 5%) in the I values. The results of the testing are shown in table 3.1. The table is split into rows; the actual values of the parameters, the fitted values (the values obtained from the fitting procedure), and the percentage error between the actual and fitted values. Sets 1 to 6 have no error in I, sets 7 to 12 have 1% error in I, and sets 13 to 18 have 5% error in I. All the fitted parameters shown were obtained by one iteration of the procedure, and the occasional large error should not be misinterpreted as a flaw, as the procedure can be re-run several times to improve the accuracy. The procedure is simple, which means that a computer program can be simply made to perform the function automatically on several I(V) spectra.

Many mathematical processes in the research (the above procedure included) required computing the numerical differentiation of spectra of data. The basic method is to simply calculate a difference in two y-values then divide by the difference in the two corresponding x-values which is not sufficiently accurate for this work. A much more accurate and thus better method has been published which takes four points around the point of interest to determine the gradient at the point of interest. The equation for this is given as (4);

$$y'(x) = \left(\frac{4}{3}\right) \times \left(\frac{y(x+h/2) - y(x-h/2)}{h}\right) - \left(\frac{1}{3}\right) \times \left(\frac{y(x+h) - y(x-h)}{2h}\right) \quad (3.8)$$

where h is the constant data interval in the x-axis. The quality of this differentiation formula was compared to the basic process described above. A set of data for  $y=x^2$  from  $x=0.0$  to  $x=3.0$  with an interval of 0.1 was calculated and differentiated numerically by both examples. The basic method gave a range of errors from 1.8% to 33% with average

of 6%. The better method gave zero error (this was retested with different data sets from polynomials and all were found to give zero error for the better method).

Table 3.1. Results of the testing of diode model fitting procedure.

Set no.	1	2	3	4	5	6	
Actual	Is(A) =	1.639E-09	3.215E-08	2.103E-07	2.984E-06	3.459E-05	5.119E-07
	n =	2.373E+00	1.982E+00	1.755E+00	7.675E-01	7.312E+00	1.719E+00
	Iph(A) =	6.000E-08	6.000E-07	6.000E-06	6.000E-05	6.000E-04	1.800E-05
	Rs(ohm) =	2.894E+01	1.434E+01	5.045E+00	2.525E+01	6.492E+01	2.153E+01
Fitted	Is(A) =	1.641E-09	3.217E-08	2.109E-07	3.003E-06	3.432E-05	5.141E-07
	n =	2.374E+00	1.982E+00	1.755E+00	7.683E-01	7.302E+00	1.720E+00
	Rs(ohm) =	2.652E+01	1.424E+01	5.005E+00	2.524E+01	6.493E+01	2.151E+01
Error	%Is =	-1.025E-01	-6.729E-02	-3.083E-01	-6.125E-01	7.856E-01	-4.164E-01
	%n =	-1.531E-02	-1.085E-02	-4.660E-02	-9.911E-02	1.292E-01	-6.141E-02
	%Rs =	8.376E+00	7.022E-01	8.016E-01	1.799E-02	-7.473E-03	9.290E-02
Set no.	7.000E+00	8.000E+00	9.000E+00	1.000E+01	1.100E+01	1.200E+01	
Actual	Is(A) =	2.469E-09	2.080E-08	4.212E-07	1.591E-06	4.248E-05	1.178E-06
	n =	4.403E+00	3.583E+00	1.810E+00	1.137E+00	6.208E+00	2.214E+00
	Iph(A) =	6.000E-08	6.000E-07	6.000E-06	6.000E-05	6.000E-04	1.800E-05
	Rs(ohm) =	1.893E+01	1.278E+01	5.275E+00	2.342E+01	5.651E+01	1.046E+01
Fitted	Is(A) =	2.477E-09	2.076E-08	4.208E-07	1.597E-06	4.216E-05	1.180E-06
	n =	4.405E+00	3.582E+00	1.810E+00	1.138E+00	6.200E+00	2.215E+00
	Rs(ohm) =	5.156E+00	1.339E+01	5.297E+00	2.341E+01	5.652E+01	1.045E+01
Error	%Is =	-3.363E-01	1.946E-01	1.053E-01	-3.882E-01	7.502E-01	-1.233E-01
	%n =	-5.280E-02	2.978E-02	1.829E-02	-5.717E-02	1.291E-01	-2.096E-02
	%Rs =	7.276E+01	-4.813E+00	-4.101E-01	1.671E-02	-8.248E-03	9.428E-02
Set no.	1.300E+01	1.400E+01	1.500E+01	1.600E+01	1.700E+01	1.800E+01	
Actual	Is(A) =	3.959E-09	3.312E-08	4.258E-07	3.438E-06	3.685E-05	9.341E-07
	n =	4.699E+00	2.762E+00	1.875E+00	6.961E-01	4.541E+00	2.238E+00
	Iph(A) =	6.000E-08	6.000E-07	6.000E-06	6.000E-05	6.000E-04	1.800E-05
	Rs(ohm) =	1.759E+01	1.231E+01	4.892E+00	1.740E+01	5.748E+01	1.749E+01
Fitted	Is(A) =	3.954E-09	3.316E-08	4.254E-07	3.434E-06	3.701E-05	1.228E-06
	n =	4.698E+00	2.763E+00	1.875E+00	6.960E-01	4.544E+00	2.350E+00
	Rs(ohm) =	2.407E+01	1.192E+01	4.916E+00	1.740E+01	5.747E+01	1.381E+01
Error	%Is =	1.339E-01	-1.468E-01	8.193E-02	1.036E-01	-4.407E-01	-3.143E+01
	%n =	2.285E-02	-2.412E-02	1.478E-02	1.900E-02	-8.328E-02	-5.011E+00
	%Rs =	-3.681E+01	3.136E+00	-4.809E-01	-8.878E-03	8.574E-03	2.101E+01

### 3.3. Optical Characteristics

This section describes the optical aspects of materials, such as what is meant by refractive index, and how parameters of the Tauc model of absorption spectra may be obtained.

### 3.3.1. n Spectra and k Spectra

The refractive index ( $n$ ) of a material is given by the ratio of the speed of light through a vacuum with respect to the speed of light through the medium, for each wavelength of light. The values of  $n$  are positive numbers, equal to or greater than 1.0, and tend to be small numbers. Refractive index spectra can sometimes be described by the Cauchy model for refractive index;

$$n(\lambda) = A + \frac{B}{\lambda^2} + \frac{C}{\lambda^4} \quad (3.9)$$

where  $A$ ,  $B$ , and  $C$  are parameters of the model.

Example spectra of  $n$  for various samples of  $\text{TiO}_2$  are given in fig 3.7.

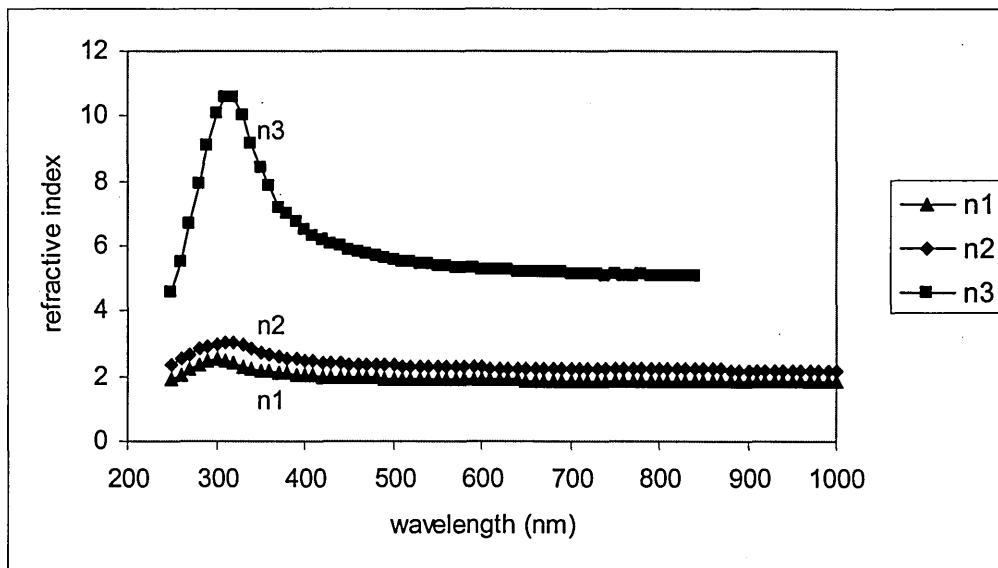


Figure 3.7. Example spectra of refractive index from the WVase32 software

When light passes through a material of thickness  $d$ , such as in fig 3.8, some of the incident light  $I_0$  is absorbed, at different rates, depending on the wavelength, to give the outgoing light  $I$ . The absorption spectra of a material can be analysed in many ways to determine many properties of the material, for instance, interference effects in the spectra can yield the spectra of  $n$  and  $k$  and the thickness  $d$ .

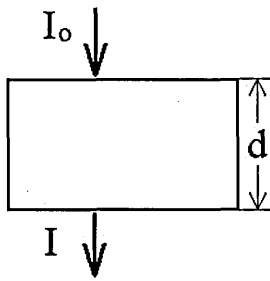


Figure 3.8. Model of light loss due to absorption by a material

The extinction coefficient ( $k$ ) of a material is a measure of the absorption of light and is given by;

$$k(\lambda) = \frac{\alpha\lambda}{4\pi} \quad (3.10)$$

where  $\alpha$  is given by;

$$I = I_0 \times e^{-\alpha d} \quad (3.11)$$

Extinction coefficient spectra can sometimes be described by the Cauchy model for extinction coefficient;

$$k(\lambda) = D \times \exp \left[ E \times 1240 \times \left( \frac{1}{\lambda} \right) - \left( \frac{1}{F} \right) \right] \quad (3.12)$$

where  $D$ ,  $E$ , and  $F$  are parameters of the model. Example spectra of  $k$  for various samples of  $\text{TiO}_2$  are given in fig 3.9.

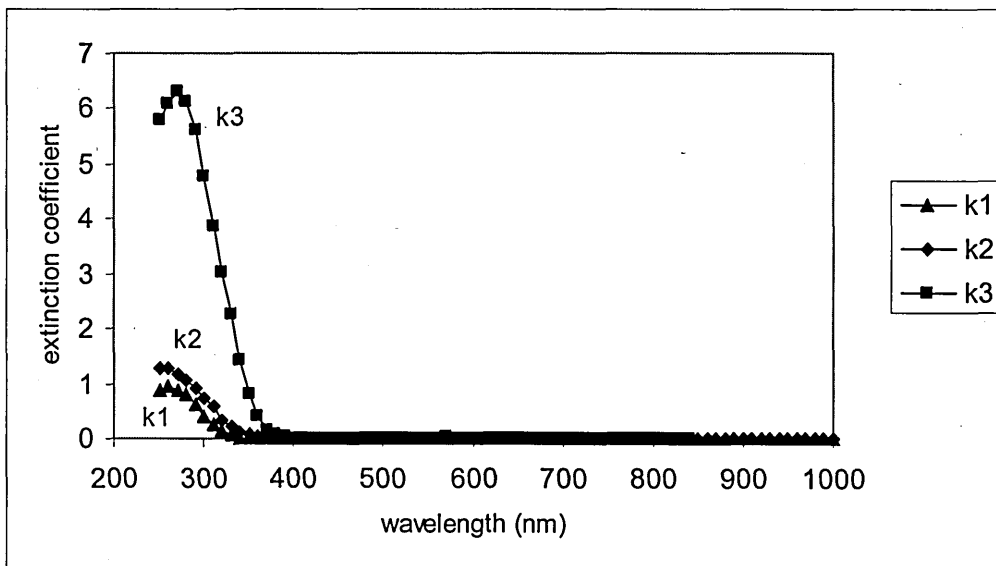


Figure 3.9. Example spectra of extinction coefficient from the WVase32 software

### 3.3.2. The Ray-Hogarth and Vale Procedures

For a large number of materials and thin films, absorption coefficient,  $\alpha(\omega)$ , is believed to obey a power law given in the form (5);

$$\alpha(\omega) = (B/\hbar\omega)(\hbar\omega - E_o)^n \quad (3.13)$$

or in a slightly simpler form;

$$\alpha(f) = (B/hf)(hf - E_o)^n \quad (3.14)$$

where B, E<sub>o</sub>, and n are parameters of the material to be found, and hf is photon energy.

E<sub>o</sub> is the optical band gap, and n is an index that depends on the type of transition between the bands. n can take on four numbers for a crystalline solid; 0.5, 1.5, 2, 3, corresponding to direct allowed, direct forbidden, indirect allowed, and indirect forbidden transitions respectively.

because;

$$I = I_o \times \exp(-\alpha d) \quad (3.15)$$

or;

$$\alpha = \frac{1}{d} \times \ln\left(\frac{I_o}{I}\right) \quad (3.16)$$

a relation can be defined and substituted;

$$Y = hf \times \ln\left(\frac{I_o}{I}\right) \quad (3.17)$$

giving;

$$Y = C(hf - E_o)^n \quad (3.18)$$

where the parameter C is a constant given by;

$$C = dB \quad (3.19)$$

from equation 3.18, the following is obtained;

$$\frac{dY}{dhf} = nC(hf - E_o)^{n-1} \quad (3.20)$$

and therefore;

$$\frac{Y}{Y'} = \frac{(hf - E_o)}{n} \quad (3.21)$$

The spectra of Y can be obtained from the UV-Vis absorption spectra. The spectra of Y' can be obtained by a very careful differentiation of Y. The parameters of E<sub>o</sub> and n can be obtained from the gradient and intercept of the Y/Y' graph.

$$n = \frac{1}{\text{gradient}} \quad (3.22)$$

$$E_o = n \times \text{intercept} \quad (3.23)$$

Once n and E<sub>o</sub> are obtained, it is a simple matter to obtain the value of C. It is recommended to obtain a value of C for each value of energy and then take some sort of average.

The Ray-Hogarth procedure works very well for UV-Vis data without error, but when numerical differentiation is performed on data with error, that error is exaggerated. This leads to significant errors in the extracted parameter values. The following method (to be known as the Vale Tauc model fitting method) is shown to be quite superior to the Ray-Hogarth method in reducing the parameter errors.

From equation 3.18, the following is obtained;

$$\sqrt[n]{Y} = \sqrt[n]{C} \times (hf - E_o) \quad (3.24)$$

If a root other than n is taken, the plot of equation 3.24 will be a curve. This can be used as criteria to obtain the correct value of n; simply sweep through increasingly accurate values of n until the plot is a straight line (for slightly noisy data, this can be ascertained by continually fitting a linear equation to the plot, and when the fit is best, the plot is deemed straight).

From the straight line, C can be obtained from the gradient as;

$$C = \text{gradient}^n \quad (3.25)$$

and  $E_o$  can be obtained as;

$$E_o = \frac{\text{intercept}}{-\sqrt[n]{C}} \quad (3.26)$$

The simplest method of acquiring the constant line fitting is to plot the nth root of Y data in a program such as Microsoft Excel, with a linear trend line and the  $R^2$  error displayed to at least 6 decimal places. To show the improvement in accuracy, a comparison was run on six identical sets of data calculated from three sets of parameters each with two levels of random noise;  $\pm 0.5\%$  error in Y and  $\pm 2\%$  error in Y. The noise was added with the rand() function in Microsoft Excel. The results of the comparison and the original parameter values are shown in table 3.2. Sets 1-3 have 0.5% error, sets 4-6 have 2% error. The Vale method is seen to be generally superior to the Ray-Hogarth method.

Table 3.2. Results of the Tauc model fitting method comparison

True Values				Vale error as percentage of Ray-Hogarth error (%)		
set	n	Eo (eV)	C	n	Eo	C
1	2.0000	2.1400	8.1120	0.0000	0.4377	1.3034
2	1.5000	3.0990	1.0140	23.0484	15.1233	17.0620
3	3.0000	4.1330	64.9000	0.0000	5.1931	20.0371
4	2.0000	2.1400	8.1120	14.6067	0.6347	3.2952
5	1.5000	3.0990	1.0140	9.2655	4.7781	8.6675
6	3.0000	4.1330	64.9000	99.4393	74.5153	78.4906
Vale fit results				Error (%)		
set	n	Eo (eV)	C	n	Eo	C
1	2.0000	2.1400	8.1148	0.0000	0.0016	0.0347
2	1.5030	3.0979	1.0111	0.2000	-0.0358	-0.2828
3	3.0000	4.1331	64.8288	0.0000	0.0026	-0.1098
4	1.9990	2.1400	8.1076	-0.0500	-0.0014	-0.0548
5	1.5020	3.0984	1.0116	0.1333	-0.0181	-0.2348
6	3.0120	4.1312	64.4582	0.4000	-0.0443	-0.6808
Ray and Hogarth fit results				Error (%)		
set	n	Eo (eV)	C	n	Eo	C
1	2.0143	2.1322	7.8958	0.7128	-0.3624	-2.6654
2	1.5130	3.0917	0.9972	0.8677	-0.2368	-1.6575
3	2.9917	4.1350	65.2555	-0.2753	0.0493	0.5478
4	2.0068	2.1354	7.9770	0.3423	-0.2155	-1.6645
5	1.5216	3.0873	0.9865	1.4390	-0.3782	-2.7087
6	2.9879	4.1355	65.4629	-0.4023	0.0595	0.8673

### 3.3.3. The Swanepoel Procedure

Work was presented in 1983 (6) describing a procedure for calculating the thickness ( $d$ ), refractive index spectra ( $n$ ), and extinction coefficient spectra ( $k$ ) of a thin absorbing film, to an accuracy of better than 1%. The method requires only the transmission spectra of a sample and is potentially fast and simple enough to be used on a pocket programmable calculator. A transmittance spectrum (such as that in fig 3.10) of a thin absorbing film will contain 'fringes' due to interference effects arising from reflection at the layer interfaces. The Swanepoel method uses the values of transmittance of the maxima and minima to determine values of refractive index and extinction coefficient at those wavelengths.

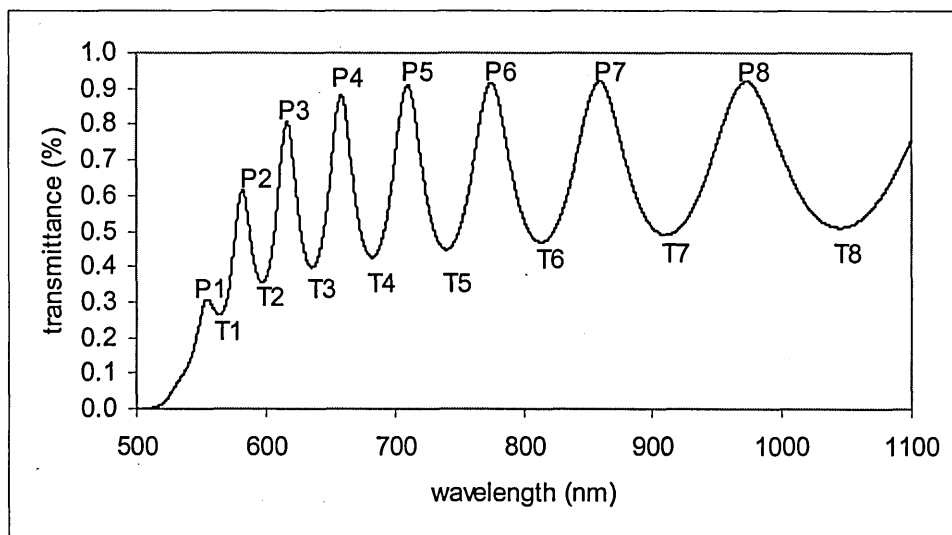


Figure 3.10. A transmittance spectrum with interference. Peaks and troughs are labelled.

The following steps are taken to obtain  $n$ ,  $k$ , and  $d$ ;

- Determine the substrate refractive index (or index spectra for better accuracy)
- The peaks and troughs must be found with high accuracy. It is recommended to fit a 3<sup>rd</sup> order polynomial function through the top (or bottom) few points to get the actual peak or trough location to several decimal places.
- Two envelopes must be constructed; one through the peaks and one through the troughs (it is recommended to create these by cubic interpolation through known

points). Values can be read off the envelopes that correspond to either a peak or trough on the spectra. The two values form a pair for that wavelength.

- Refractive index can be calculated for each pair of values from;

$$n = \left[ N + (N^2 - s^2)^{\frac{1}{2}} \right]^{\frac{1}{2}} \quad (3.27)$$

where;

$$N = 2s \frac{T_M - T_m}{T_M \times T_m} + \frac{s^2 + 1}{2} \quad (3.28)$$

where  $T_M$  is the value from the peak envelope, and  $T_m$  is the value from the trough envelope

- A value of  $d$  can be obtained from the spectra of  $n$  knowing that the basic interference equation is;

$$2nd = m\lambda \quad (3.29)$$

and thus for whole and half wavelengths;

$$2nd = \left( m + \frac{L}{2} \right) \lambda \quad (3.30)$$

or

$$\frac{L}{2} = 2d \left( \frac{n}{\lambda} \right) - m \quad (3.31)$$

This is in the form of a straight line if  $(L/2)$  is plotted against  $(n/\lambda)$ . The intercept is exactly an integer or half-integer, so the closest such value of intercept should be taken for the linear line fit of the plot. The value of  $d$  is half the gradient of the linear line fit.

- The spectra of  $\alpha$  can be obtained from the spectra of  $x$  where;

$$x = \exp(-ad) \quad (3.32)$$

and  $x$  is given by either;

$$x = \frac{E_M - \left[ E_M^2 - (n^2 - 1)^3 (n^2 - s^4) \right]^{\frac{1}{2}}}{(n-1)^3 (n-s^2)} \quad (3.33)$$

where;

$$E_M = \frac{8n^2 s}{T_M} + (n^2 - 1)(n^2 - s^2) \quad (3.34)$$

or by;

$$x = \frac{E_m - \left[ E_m^2 - (n^2 - 1)^3 (n^2 - s^4) \right]^{\frac{1}{2}}}{(n-1)^3 (n-s^2)} \quad (3.35)$$

Where;

$$E_m = \frac{8n^2 s}{T_m} - (n^2 - 1)(n^2 - s^2) \quad (3.36)$$

Swanepoel gives an example of the procedure used to extract parameters from simulated data with  $n$  and  $\alpha$  determined from two simple models. Fig 3.11 shows the spectra of the simulated data (which is repeated in fig 3.10), with the envelopes constructed and the pairs of values shown by square markers (maxima) and triangles (minima). Fig 3.12 shows spectra of  $n$  and  $\alpha$  true values (solid lines) and those obtained from the procedure (triangles and squares respectively). The true and derived thickness values differed by 0.05%. As can clearly be seen from fig 3.12, and the aforementioned thickness error, Swanepoel's method can be very accurate.

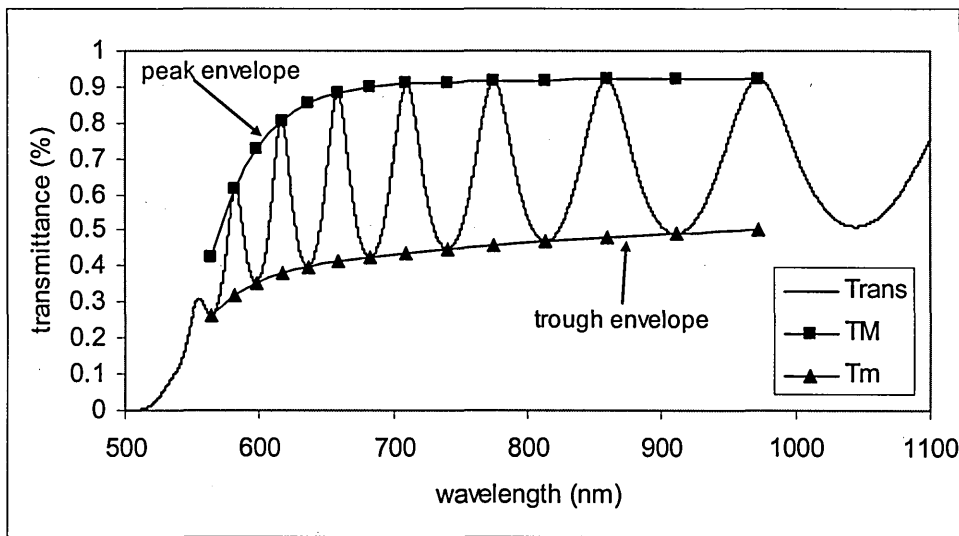


Figure 3.11. Swanepoel example showing both envelopes and TM and Tm data points.

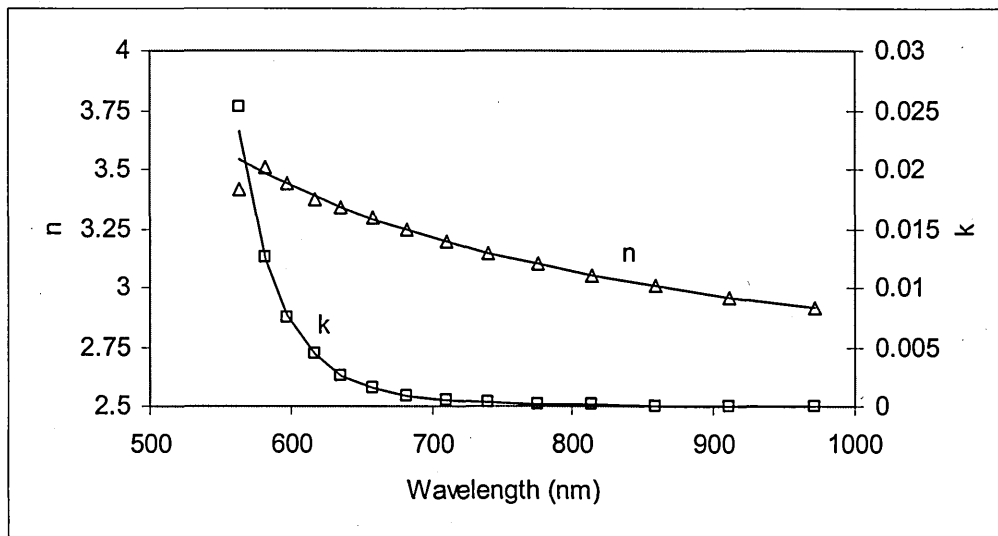


Figure 3.12. Swanepoel example showing true and fitted n and k spectra.

### 3.4. Description of Selected Measurement Methods

There were many complicated measurement methods used in this research, and to allow the reader to better understand the basic operation of the more complicated ones, they are described below, with relevant theory where appropriate.

#### 3.4.1. Atomic Force Microscopy

AFM is a microscope measurement method that can be used to image a sample surface in three dimensions and at atomic scale. It comprises a tiny spike of Si or Si<sub>3</sub>N<sub>4</sub> with a

sharp point. The tip of the spike is moved across the sample and is deflected by deviations on the surface. The deviations can be detected by the following technique; the spike is attached to a shiny cantilever upon which a laser is focused. The deviations in the sample surface cause deviations in the cantilever and thus the laser is reflected away from the equilibrium position. The deviation in the laser spot can be detected with e.g. a photodiode array. An example of such a system is given in the functional diagram in fig 3.13. The four-quadrant detector will measure the deflection of the laser spot, and thus the deflection of the tip and the height of the sample at that point relative to some point of the sample. Height resolution can be as low as 0.01nm and scan sizes can be as large as 150,000nm. The radius of the tip is typically in the range of 10nm. There are two main modes of AFM; contact and tapping mode. In the tapping mode, the tip is tapped against the sample at high frequencies, whereas in contact mode, the tip is dragged and moves up and down only by the sample.

The tips used in this research were tapping mode tips and were designed to oscillate at 300kHz, with drive amplitude of approximately 200mV.

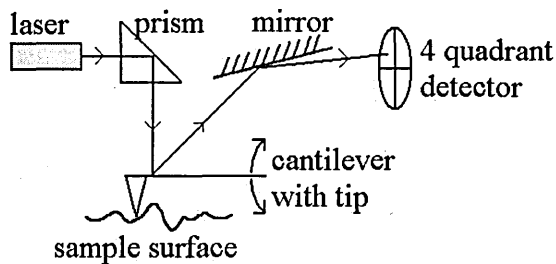


Figure 3.13. A schematic diagram of an AFM system

The AFM setup (fig 3.14) used in this research is situated in a dedicated room, and the microscope itself rests on an antivibration platform, which itself can be placed on a sprung tripod (one leg is shown in the right of fig 3.14a), to further reduce the vibration noise.

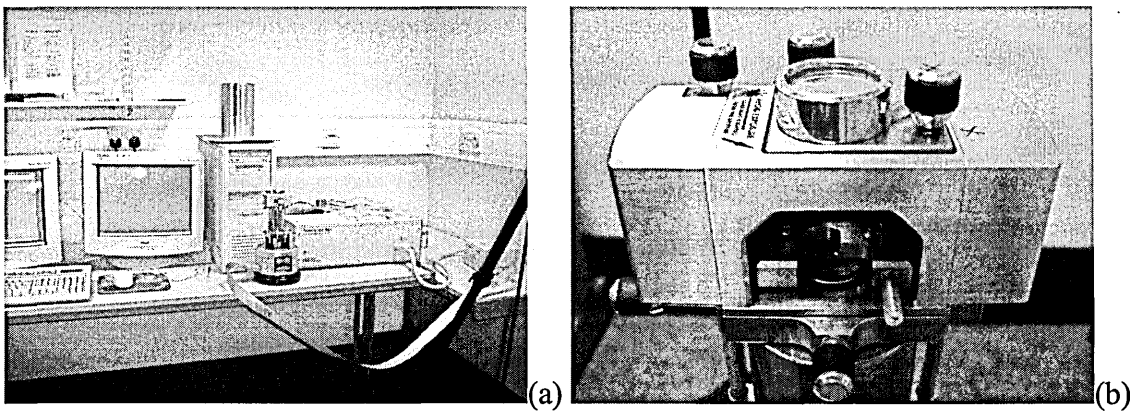


Figure 3.14. The laboratory containing the AFM setup (a) and the scanning head of the microscope with adjustment knobs visible (b).

There are many problems that can happen with AFM; a particle can become attached to the tip and stamped across the sample - this can lead to loss of resolution and a false change in height; the tip can become split in two (or more) by wear - this leads to multiple images of details (shown by obvious pairs of details everywhere); the sample may begin the scan warmer or cooler than the microscope- this causes thermal drift in the sample relative to the tip and a smearing of details as the temperatures equalise.

Scan times are in the range of one second per line, making for around 250 seconds per entire scan. The frequency can be increased making for shorter times in the lab, but the tip will begin to miss smaller details. The frequency can be decreased giving better pictures but more thermal drift effects due to the thermal drift being relatively faster than the tip scanning speed.

### 3.4.2. X-Ray Diffraction

The physics of the production and nature of X-Rays will not be described here. It is suffice to say that the X-rays used for the measurements were approximately collimated, monochromatic waves and have a wavelength of 0.1540561nm.

When an X-Ray is incident on an atom it is scattered in all directions, though not equally (1). If a ray scattered in a particular direction from an atom is in phase with a ray in the same direction coming from an atom further within the crystal, the two rays

will fully constructively interfere as shown in fig 3.15. In 3.15 (a), rays a, b, and c, forming a wavefront, are incident on (and scattered by) three different atoms in the lattice. All three rays are at the correct angle for the planes and are thus interfering constructively. Ray b' is one wavelength behind a', and c' is two behind. In 3.15 (b), two rays a, and b are incident on (and scattered by) two different atoms in the lattice and are of the correct angle. Ray b' is one wavelength behind a', so both interfere constructively.

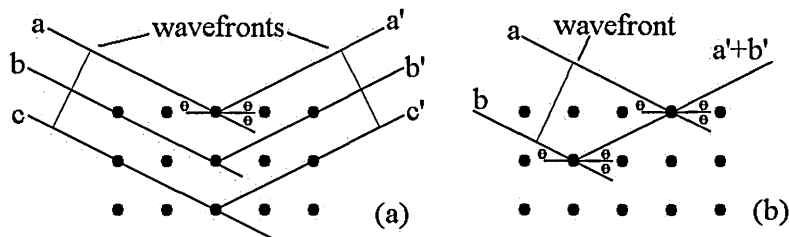


Figure 3.15. Diffracted rays forming a wavefront (a), and diffracted rays forming a single in phase ray (b).

At all angles other than a particular angle, the rays will partly destructively interfere, and thus give a reading less than 100% at this angle. Each set of planes in the lattice will have an angle at which full constructive interference can take place. At these angles the X-Ray signal will be strongest. It is then a simple matter to sweep a detector through all angles, measuring X-Ray strength as it does. A spectrum containing peaks for each plane will result. The requirement for diffraction is given by Bragg's Law;

$$n\lambda = 2d' \sin(\theta) \tag{3.37}$$

where  $n\lambda$  is an integer number of X-Ray wavelengths,  $d'$  is the inter-planar distance and  $\theta$  is the incident (and diffracted) angle. Values of  $d'$  can be simply obtained for each peak in the spectrum ( $n$  is normally assumed to equal one for this procedure).

The technique of XRD is to find what kind of crystal the material is. It is slightly surprising that the best sample is an amount of compressed ultra-fine powder. The angle of incidence determines which plane in the lattice is 'excited'. A particle is a single

crystal or collection of crystals randomly oriented with respect to the X-Ray beam, which means that the powder sample is like a single crystal sample rotated about all axes simultaneously, which makes it much easier for the detector to catch each excited plane (in a non-powder sample, the certain planes may be rotated about the axis of the beam, so the diffracted rays miss the detector - if the rays are in all directions about the beam axis, the diffracted beams can't be missed).

There is a broadening effect on the diffraction peak due to a non-infinite crystal thickness (this will not be explained here, just the application of the effect). If a crystal thickness is below several hundred angstroms, there is a measurable range of angles, beside the Bragg angle, at which the intensity is non-zero. The range increases with decreasing crystal thickness, giving a means to measure the crystal (or grain) thickness, and if the grains are assumed to be spherical, the grain width or size may also be determined. The grain thickness is given by Scherrer's equation;

$$t = \frac{0.9\lambda}{B \cos \theta_B} \quad (3.38)$$

where B is either half the width of the range of  $2\theta$  where the intensity drops to zero, or can be determined from the full width measured at half the maximum height (Full Width at Half Maximum or FWHM) a pictorial explanation of the process is given in fig 3.16.

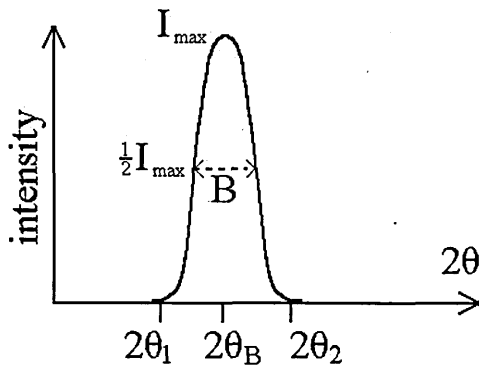


Figure 3.16. The peak broadening parameter, B, used for calculating thickness

Sometimes there are planes within the lattices that give two sets of rays in the same direction and individually in phase, but where the two sets are in anti phase. In this case, there ought to be a diffraction peak, but the intensity is zero due to the two sets annulling each other. The intensity of the peaks should depend only on the structure of the unit cell, but is actually modified by six factors, including; thermal agitation of the atoms which decrease the periodicity of the lattice, and absorption within the sample itself. These changes in the relative intensity of the peaks (a value that is more important than the actual intensity) are not consistent across the spectrum, and so, they complicate the matter of identifying the phase being studied.

Several data may be obtained from XRD including the interplanar distance calculated from Bragg's law, a comparison with a standard database of phases to determine the material and its particular structure, size, and its interior angles, and an approximate estimate of the grain size or grain height from Scherrer's equation. XRD is therefore a powerful tool for the material scientist.

### **3.4.3. X-Ray Photoelectron Spectroscopy**

The electrons in the core levels of atoms have a binding energy, which is unique to that particular atom, much like a fingerprint is unique to a particular person. When a beam of X-Rays are incident on the surface of a sample, the core electrons absorb the photons, and if the photon energy is sufficiently high, the electron can escape the surface with kinetic energy given by the photon energy minus the binding energy as follows;

$$E_b = hf - E_k \quad (3.39)$$

If  $hf$  is known,  $E_k$  can be measured and thus  $E_b$  can be determined for each element in the sample. By comparing the  $E_b$  data to a list of standards, the elements in the sample

may be determined (much like phase identification with XRD). The  $E_b$  is sensitive to changes in the chemical structure in which the elements are part, because the bonding of atoms in a compound shifts  $E_b$ . From this shift, it is possible to determine the bonding states of the atoms and thus, the compounds (not just the individual elements) that are present in the sample (again by comparison with a list of standards).

#### 3.4.4. Spectroscopic Ellipsometry

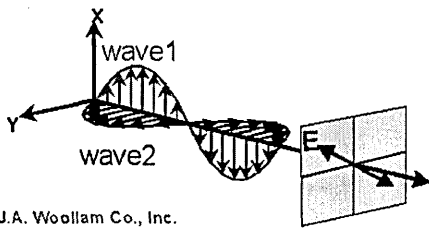
The theory of ellipsometry and the analysis of the data obtained are presented in an instruction manual (7) and are quite complex. A brief description of ellipsometry will be presented here.

Ellipsometry uses linearly polarised light and measures samples by the change in the polarised light after reflecting from the sample surface. The light incident on the sample is comprised on two components; p-polarised light (whose wave is parallel to the plane of incidence) and s-polarised light (whose wave is perpendicular to the plane of incidence). Each wave is reflected differently when passing through the various layers of the sample, and in doing so, a difference in phase and amplitude in the waves is created which make the light elliptically polarised. The size of the changes depends on the characteristics of the sample, so the changes are a measure of the characteristics.

The user will obtain experimental spectra of  $\Psi$  and  $\Delta$ , and by constructing a model of the layers of the sample with suggested values for thickness and complex refractive index ( $\tilde{n} = n + jk$ ) for each layer, the user will also obtain theoretical values of  $\Psi$  and  $\Delta$ , and then by a fitting algorithm, the parameters of the model are iteratively changed, depending on the quality of fit (Mean Squared Error - MSE) such that the experimental and theoretical values converge. The best fit gives the correct model parameters.

The method of obtaining the experimental and theoretical values of  $\Psi$  and  $\Delta$  is presented below. In practice, only two parameters of the entire model can normally be fitted at a time - the rest must be known.

Light is comprised of waves consisting of an electric and magnetic field travelling through space. The two fields are perpendicular to each other and the direction of travel, and it is the electric field that is of interest here. A particular wave can be thought of being the sum of two rays perpendicular to each other (one in a plane lying on the x axis, and one on the y axis), each with some amplitude and phase. The polarisation state of the wave refers to the imaginary shape traced in space by the wave as it travels through some plane perpendicular to the direction of travel. If the two waves are in phase, the waves will be at a maximum at the same time, then at a minimum at the same time, and the shape traced will be a straight line as shown in fig 3.17. If the two waves are  $90^\circ$  out of phase, first one will reach a maximum while the other is zero, then vice versa, then one will reach minimum while the other is zero, and then vice versa. This gives a circular traced shape as shown in fig 3.18. If the phase difference is any other angle, the traced shape will be elliptical (it is obvious that the linear and circular states are subsets of the elliptical state) as shown in fig 3.19. This gives the technique of ellipsometry its name.



J.A. Woollam Co., Inc.

Figure 3.17. Linear polarisation of light waves.

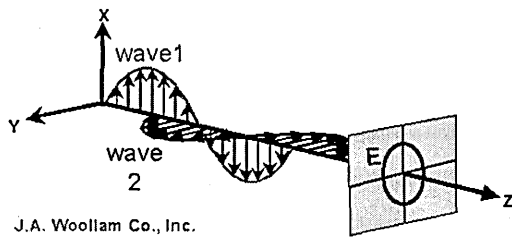


Figure 3.18. Circular polarisation of light waves.

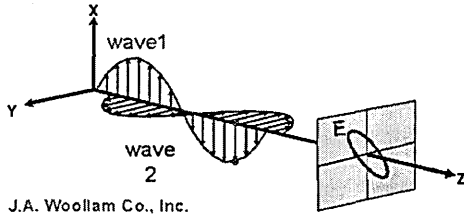


Figure 3.19. Elliptical polarisation of light waves.

The light reflected from the sample passes into a detector, which produces a sinusoidally alternating voltage of the form;

$$V(t) = DC + a \cos(2\omega t) + b \sin(2\omega t) \quad (3.40)$$

The two important quantities measured by the ellipsometer are  $\alpha$  and  $\beta$ , which are normalised Fourier coefficients of the signal, and are given by;

$$\alpha = \frac{a}{DC} = \frac{\tan^2 \Psi - \tan^2 P}{\tan^2 \Psi + \tan^2 P} \quad (3.41)$$

and

$$\beta = \frac{b}{DC} = \frac{2 \tan \Psi \times \cos \Delta \times \tan P}{\tan^2 \Psi + \tan^2 P} \quad (3.42)$$

where  $\alpha$  and  $\beta$  are the ellipsometric parameters that characterise the sample, and  $P$  is the input polarizer angle with respect to the plane of incidence, which will be known.

Equations 3.41 and 3.42 can be inverted to give the *experimental* values of  $\Psi$  and  $\Delta$  in terms of  $\alpha$ ,  $\beta$ , and  $P$  as;

$$\tan \Psi = \sqrt{\frac{1+\alpha}{1-\alpha}} \times |\tan P| \quad (3.43)$$

and

$$\cos \Delta = \frac{\beta}{\sqrt{1-\alpha^2}} \times \frac{\tan P}{|\tan P|} \quad (3.44)$$

When the ellipsometer calculates the theoretical data for a multi layered sample, it must consider that there are an infinite number of (quickly diminishing) reflections from each layer interface. The nature of each reflection will depend on each reflection before, and the result is a series of expressions that converge into one equation. The Fresnel reflection coefficients for p and s polarised waves and the phase (or optical) thickness of the film are;

$$\tilde{r}_p = \frac{\tilde{n}_1 \cos \tilde{\varphi}_0 - \tilde{n}_0 \cos \tilde{\varphi}_1}{\tilde{n}_1 \cos \tilde{\varphi}_0 + \tilde{n}_0 \cos \tilde{\varphi}_1} \quad (3.45)$$

and

$$\tilde{r}_s = \frac{\tilde{n}_0 \cos \tilde{\varphi}_0 - \tilde{n}_1 \cos \tilde{\varphi}_1}{\tilde{n}_0 \cos \tilde{\varphi}_0 + \tilde{n}_1 \cos \tilde{\varphi}_1} \quad (3.46)$$

and

$$\beta = 2\pi \tilde{n}_1 \frac{d}{\lambda} \cos \tilde{\varphi}_1 = 2\pi \frac{d}{\lambda} \sqrt{\tilde{n}_1^2 - \tilde{n}_0^2 \sin^2 \varphi_0} \quad (3.47)$$

respectively, where the subscripts refer to the layer (0=upper layer, 1=lower layer),  $\phi_n$  is the angle transmitted from layer n through layer n+1, d is layer thickness, and  $\lambda$  is wavelength. The light reflected from an interface is the electric field expression of the incident beam multiplied by the Fresnel coefficient, and clearly, after multiple reflections, the expression becomes a complicated series. The series converges into simple form (which depends on the number of interfaces) and for example, the expression for a two layer system is;

$$\tilde{E}_{total}^r = \left( \frac{\tilde{r}_{01} + \tilde{r}_{12} \exp^{-j2\beta}}{1 + \tilde{r}_{01} \tilde{r}_{12} \exp^{-j2\beta}} \right) \times \tilde{E}^{incident} \quad (3.48)$$

where  $\tilde{E}_{total}^r$  is the resultant reflection and  $\tilde{E}^{incident}$  is the input wave. The pseudo Fresnel coefficient for the p polarisation is;

$$\tilde{R}_p \equiv \frac{\tilde{E}_{total}^r}{\tilde{E}_{incident}} \quad (3.49)$$

and the same expression applies to the s polarisation. This represents an overall coefficient that is affected by all the layers in the sample.

The relation between the ratio of pseudo Fresnel coefficients and  $\Psi$  and  $\Delta$  is;

$$\tan \Psi \exp^{j\Delta} = \frac{\tilde{R}_p}{\tilde{R}_s} \quad (3.50)$$

Equation 3.50 gives the *theoretical* values of  $\Psi$  and  $\Delta$ .

The two versions of  $\Psi$  and  $\Delta$ , experimental and theoretical, have now been described and the calculations for them presented.

### 3.5. Basic Theory of the Optical Modulator

It was decided at the start of the research to investigate the recombination lifetime of photogenerated carriers in the photovoltaic cell, or in individual layers. The lifetime of carriers is an important parameter, which can limit the efficiency of the device. If photogenerated carriers recombine before they are separated and used, then their energy only produces light and/or heat and is thus effectively wasted. It has been shown in published work that recombination can happen in the order of tens of nanoseconds for some materials (8,9).

The carrier recombination time can be measured by generating excess free carriers in a sample, then very quickly stopping the generation, and measuring the time it takes for the number of carriers to decrease to half the steady value. This will of course give the 'half life' of the carriers. The recombination can be observed by monitoring the change in resistance (via voltage change) of the sample in a simple circuit as shown in fig. 3.20.

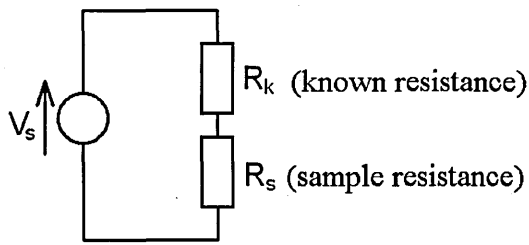


Figure 3.20. A simple circuit for measuring recombination time via voltage change

The concentration of excess free carriers reduces exponentially according to;

$$\delta n(t) = \Delta n \exp\left(-\frac{t}{\tau}\right) \quad (3.51)$$

Where  $\delta n$  is excess carrier concentration at time  $t$  and  $\Delta n$  is the initial excess. Assuming the sample is strongly  $n$  or  $p$  type, the conductivity can easily be calculated;

$$\sigma(t) = q\mu[\delta n(t) + n] \quad (3.52)$$

Where  $\mu$  is the mobility of majority carriers and  $n$  is the equilibrium carrier concentration. The resistance of the sample ( $R_s$ ) at time  $t$  is thus given by;

$$R_s(t) = \frac{L}{A\sigma(t)} \quad (3.53)$$

where  $L$  is the length (or normally the thickness of film) and  $A$  is the cross sectional area normal to the direction of current flow (normally the area of the sample).

The known resistance  $R_k$  should be of the same order of magnitude as the sample resistance (in equilibrium) so as not to be negligible or dominating. The voltage measured across  $R_s$  is simply given by;

$$V_{R_s} = \frac{V_s R_s}{(R_k + R_s)} \quad (3.54)$$

If the time for the generation cut-off is similar to, or even greater than the carrier half life, then  $R_s$  will closely follow the fall off curve of generation (since significant numbers of carriers are still being generated when the steady state concentration is supposed to be going down), and will be useless for calculation. It therefore follows that

the generation cut-off must be as fast as possible to have negligible effect. If the generation cut-off time is one fifth of the lifetime then generation will end soon enough for the tests. The generation itself must ideally continue for long enough for the sample to attain a steady concentration of free carriers, and must also be off for the carriers to fully recombine (it is obvious from equation 3.51 that the carriers will never fully recombine as it is a probabilistic phenomena, but the number of excess carriers will at some point become negligible). If the generation pulse width and space times are at least five lifetimes, then the sample should become steady in both cases.

The response of the circuit (the value of  $V_{RS}$ ) to a pulse of light is to first fall from the dark value, until there is equilibrium of generation and recombination of free carriers, then as the pulse suddenly ends, the response will rise back up to the dark value. By fitting equation 3.51 to the curve, the lifetime can be obtained.

For an oscilloscope to monitor such tests, the generation must be applied in consistent pulses, of mark and space times of at least hundreds of nanoseconds, and cut off (and cut on) time(s) of at most nanoseconds.

It is shown in Chapter 2 that commercial systems for producing sufficiently fast pulses can run into the tens of thousands of pounds. For this reason, a cheap system had to be devised. The other problem with commercial systems is that the pulse tends to be a narrow and rounded and gives inhomogeneous illumination to the sample and therefore produces an inhomogeneous excess carrier distribution. This adds extra complexity to the measurements. A simple mechanical chopper will produce a rectangular (or slightly trapezoidal) pulse, which if the on time is long enough, will produce a homogeneous excess carrier distribution, which is greatly desirable. Unfortunately, simple mechanical

choppers are relatively slow and even the best cannot produce pulses with cut-off times in the region of nanoseconds.

#### Reference List

- (1) Cullity B.D., S.R. Stock, 2001, Elements of X-ray Diffraction. 3rd ed. Prentice Hall
- (2) Kasap S.O., 2001, Optoelectronics and Photonics: Principles and Practices. Prentice Hall
- (3) Tracey S., 1997, Dye Sensitisation of Sol-Gel Derived Titanium Dioxide films, Ph.D., School of Engineering, Physical Electronics and Fibre Optics Research Laboratories, Sheffield Hallam University.
- (4) Kincaid D., Cheney W., 1991, Numerical Analysis. Published Brooks/Cole Pub. Co.
- (5) Ray A.K., Hogarth C.A., Journal of Physics. D: Applied Physics, 1990, 23, 458-459.
- (6) Swanepoel R., Journal of Physics E: Scientific Instruments, 1983, Vol 16, 1214-1222
- (7) Guide to Using WVASE32, 1997, J.A.Woollam Co. Inc.
- (8) Wilke K., Breuer H.D. Journal of Photochemistry and Photobiology A: Chemistry 1999; 121(1):49-53.
- (9) Kim S.C., Heo M.C., Hahn S.H., Lee C.W., Joo J.H., Kim J.S. et al. Materials Letters 2005; 59(16):2059-2063.

## Experimental Methods

---

### 4.1. Preparation of samples

In this section, the manufacture of various types of sample studied for this research will be described. Many different samples were made to study many properties of materials and devices, such as crystallinity and solar cell efficiency, but only the manufacture of common elements will be given. For example, thin films of  $\text{TiO}_2$  were deposited as base layers in solar cells and also for studying the properties of the  $\text{TiO}_2$  itself. All substrates were cleaned by the following method; rinsed in Millipore water, submerged in a glass container full of a mix of Millipore and Decon Neutracon soap, and ultrasonically agitated for 30 mins in a Kerry PUL 55 Ultrasonic Bath. After the agitation, the glass container was flushed out with more millipore water, until no soap bubbles remained, the substrates were then placed on lab tissue and their topsides were dried with nitrogen.

#### 4.1.1. Sputtered $\text{TiO}_2$ Thin Films

$\text{TiO}_2$  thin films were deposited by DC reactive magnetron sputtering on cleaned standard glass slides, pieces of silicon wafer, and etched (the procedure for etching is described below) Fluorine doped Tin Oxide (F:TO) coated glass (Hartford Glass Company), using a Microvac 350 sputtering system by Ion Tech, within an atmosphere of a mixture of argon and oxygen with neither substrate biasing or heating. The target was made from metallic titanium of purity  $>99.99\%$  with a 30 mm erosion zone. Before deposition, the chamber was pumped down to a vacuum better than  $5 \times 10^{-5}$  mbar by

rotary and diffusion pumps, before refilling with the required mixture and pressure of argon and oxygen in a continuous flow through the chamber. The target to substrate distance was approximately 120 mm, and the thickness was measured in situ by a quartz crystal microbalance (QCM) placed at the same height as the substrates and near to one side. It is important to note that the substrates were placed very close to each other, and at the same height, so that the film on each should have been nominally identical.

The films were 200nm thick, according to the QCM, and didn't appear to be shiny, implying good stoichiometry (unoxidised metal give the samples a shiny appearance). The ratio of Oxygen to Argon was at 1:10. The working pressure was approximately  $5 \times 10^{-3}$  mbar. The deposition rate about 0.1nm/s, with voltage and current supplied at 450V, and 0.2A respectively, and the films took about 35min to deposit. These values were found by a great deal of trial, error, and change. Visually good films were made with twice the pressure, and had very similar physical characteristics (in terms of XRD, AFM, and bandgap) to the current films, but the rate was only 0.02nm/s (to still give non-metallic films) meaning it took around 2hours 46minutes to deposit 200nm. More work was done to improve the rate to the current level, which involved mainly dropping the working pressure by half. This may have allowed the oxidised material to reach the sample without losing so much kinetic energy due to collisions with the sputtering gas, and thus for more material to reach the sample, and produce a higher rate. If the deposition rate was higher than stated, the Titanium did not have time to oxidise and the film became shiny. If the pressure was lower than stated, the plasma became unstable and sometimes went out. For those samples that were annealed, post annealing took place in a programmable furnace as explained below. The samples were cooked in batches, and each batch took at least 26 hours. The time was usually longer than this as the furnace didn't have active cooling and therefore couldn't cool fast enough, which isn't a problem for the samples, as the cooling rate is ideally very slow.

#### 4.1.2. Powder TiO<sub>2</sub> Thin Films

A new technique for deposition of the Degussa P25 powder has been developed for this research, to be known as 'flood printing', which is an alternative to the usual method of screen-printing that is usually used for depositing thin films of powder (1, 2, 3). A thin mixture of the nanoparticle TiO<sub>2</sub> (also referred to as nc-TiO<sub>2</sub>) is poured into a shallow trough placed tightly on top of the substrate (scotch tape can easily be used to create such a trough), which flooded the trough. The trough was slightly tipped up (to force the majority of the liquid to flow to one side) and the excess fluid was drained away, leaving a thin layer of the mixture, which can be quickly dried, before a second or third layer is applied, as shown in fig 4.1.

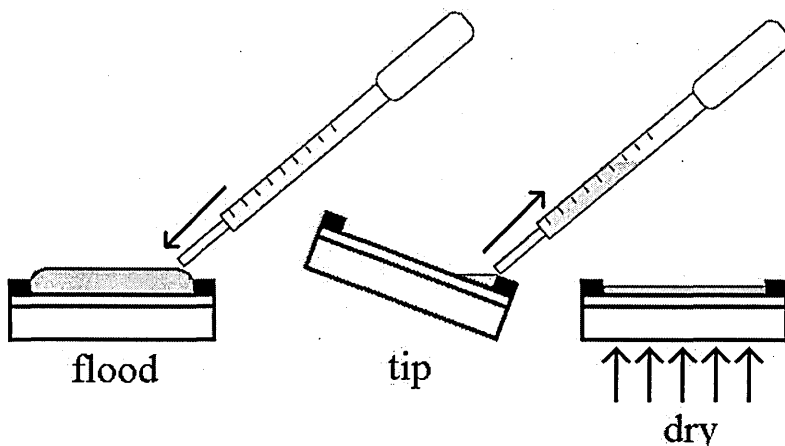


Figure 4.1 The flood printing process

Flood printing has advantages over screen printing in that it can easily coat large substrates and does not require something to scrape over the surface of the newly created film (which would make subsequent layers difficult to apply) possibly causing uneven films by slight bowing of the spreader (even a 10 $\mu$ m deep bow would be disastrous) or particles being dragged along the film. There are limits to the flood printing process; if the mixture is too thin, there is difficulty in properly wetting the substrate and a film cannot be applied, whereas if the mixture is too thick, there is substantial shrinkage damage and the edges of the film become crusty and flake away.

Some powder and sputtered films were sintered (in fact all of the last 8 designs of solar cells were sintered before dye application). The sintering involves slowly heating the sample to and holding it at a temperature of 550°C for 30 minutes before slowly cooling the sample back to room temperature. Many published work uses sintering as a method of increasing the mechanical strength of the porous film (4, 5, 6). The slow cooling and heating rates allows the films to gradually stretch and shrink and may prevent stress damage. The sintering greatly improves the mechanical strength of the powder films as shown by the greater rubbing force required to remove the powder from a glass slide. A more rugged powder film was also less susceptible to damage during the dyeing process. A graph of the heating cycle is shown in fig 4.2.

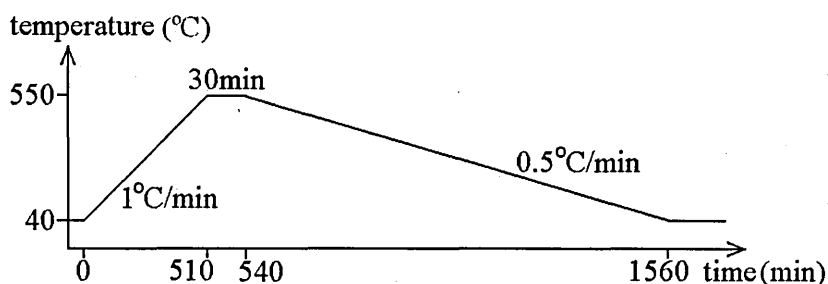


Figure 4.2. A graph of the heating cycle for sintering TiO<sub>2</sub> films

#### 4.1.3. Fabrication of Solar cells

The solar cells were formed from between four and six active layers, depending on complexity. All cells were based on an F:TO coated glass slide, 25mm long by 25mm wide, with a pinhole-blocking layer of 100nm TiO<sub>2</sub> that was deposited by the sputtering process described above. A strip of F:TO was etched off by the following sequence;

1. Mask off wanted area with scotch tape (making sure that it is *all* in contact)
2. Soak tip of cotton bud with HCl (conc.)
3. Dip tip of soaked cotton bud in zinc powder (not solid zinc)
4. Rub tip across the area to be etched

5. Observe colour change in F:TO film from clear (with a *very* slight blue tint) to yellow-brown and back to clear again

When the substrate became clear, any residue was washed off with water, the sample was then dried and the resistance checked with an ohmmeter. A reading off the scale for all of the etched area was a good indication of complete etching. The scotch tape was removed and the sample cleaved for easier mounting. The gold top contact was applied using an Edwards E306a vacuum system, with gold wire (99.999% pure) in a molybdenum boat. The platinum (99.99% pure) contacts were all sputtered using the same system as the Titanium (and with similar parameters except that the rate was 0.2nm/s). The nc-TiO<sub>2</sub> thin films were applied as described above, and the dyes were applied by either the flood soak technique where the sample is flooded with a set amount of dye solution, which is then left to dry, or the bath soak technique, where the sample is soaked in a bath of solution (upside down to reduce the amount of solution needed) then tipped up to allow the excess dye to run off, and the rest to dry, as shown in fig 4.3, and fig 4.4 respectively. There were 15 designs of solar cell made, which are shown in table 4.1. Every design had a 100nm thick layer of sputtered TiO<sub>2</sub> on top of the F:TO layer to prevent short circuits.

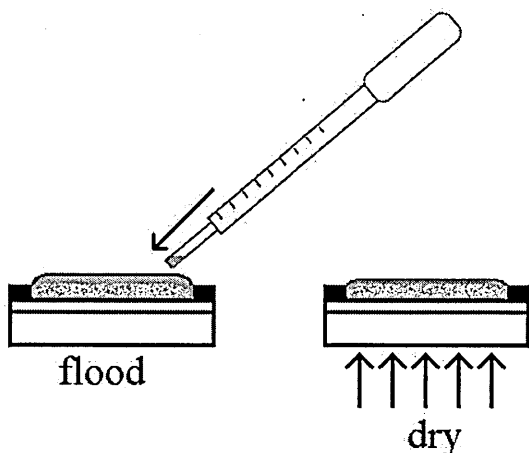


Figure 4.3. The flood soaking technique for dye application.

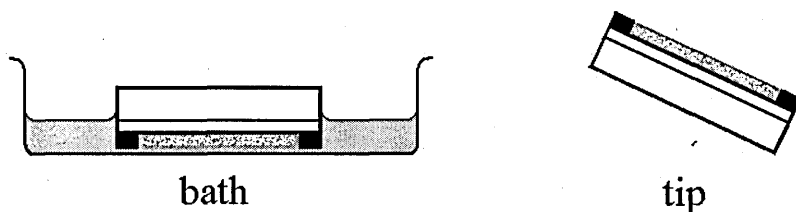


Figure 4.4. The bath soaking technique for dye application

The dyes used as the sensitising material in the cells must make the best use of the light from the sun that actually makes it through the atmosphere. Most sunlight energy arriving at the Earth's surface is in the 'visible' region (visible to humans due to evolution) and a bit beyond – from about 400nm to 900nm, and it makes sense to choose a dye that strongly absorbs in this region. The best dyes would absorb across the whole region, and then be able to efficiently use the absorbed energy, but as has been mentioned, such dyes tend to be expensive (in the region of £100's per gram). The dyes used in this research are cheap, have peak absorption within the visible spectrum, and are also complimentary as their peak absorptions are at two different wavelengths (compare fig 2.1 with fig 2.4 and fig 2.5).

Besides the absorption spectra of the dyes, they should be reasonably conductive so as not to cause a large increase in the series resistance, and be easily applied to the rough surface with good control over the dye thickness.

The powders were all measured out using a Mettler Toledo AT261 hotstage, and all liquids were measured out using a pipette of appropriate volume. It is important to note that each design was created as part of an on-going design procedure. Each design was based on another with a single change e.g. one design may have a PVK layer, and there is another design that is identical except that it does not have a PVK layer. This allowed the change in performance to be observed that was a result of the design change, and to predict a good direction of further changes.

Table 4.1. Design parameters of the 15 designs of cell. Abbreviation key shown.

Design	nc-TiO <sub>2</sub>	Dye layer	PVK layer	Contact	sintered
1	3 layers at 0.05g/ml	20ul of CuPc(C) at 10mg/ml, flood soaked	n/a	40nm of Gold	half
2	3 layers at 0.05g/ml	20ul of CuPc(C) at 10mg/ml, flood soaked	n/a	100nm of sputtered Platinum	half
3	3 layers at 0.05g/ml	25ul of CuPc(W) at 10mg/ml, flood soaked	n/a	100nm of sputtered Platinum	half
4	1 layer at 0.05g/ml	25ul of CuPc(W) at 10mg/ml, flood soaked	n/a	100nm of sputtered Platinum	half
5	1 layer at 0.05g/ml	25ul of CuPc(W) at 10mg/ml, flood soaked	n/a	200nm of sputtered Platinum	half
6	n/a	25ul of CuPc(W) at 10mg/ml, flood soaked	n/a	100nm of sputtered Platinum	not sintered
7	1 layer at 0.01g/ml	25ul of CuPc(W) at 10mg/ml, flood soaked	n/a	100nm of sputtered Platinum	all
8	1 layer at 0.01g/ml	CuPc(W) at 10mg/ml, bath soaked	n/a	100nm of sputtered Platinum	all
9	1 layer at 0.01g/ml	CuPc(W) at 10mg/ml, bath soaked	3 layers of PVK at 10mg/ml, bath soaked	100nm of sputtered Platinum	all
10	1 layer at 0.01g/ml	RB (W) at 10mg/ml, bath soaked	n/a	100nm of sputtered Platinum	all
11	1 layer at 0.01g/ml	RB (W) at 10mg/ml, bath soaked	3 layers of PVK at 10mg/ml, bath soaked	100nm of sputtered Platinum	all
12	1 layer at 0.01g/ml	3 layers of CuPc(W) at 10mg/ml, bath soaked	n/a	100nm of sputtered Platinum	all
13	1 layer at 0.01g/ml	3 layers of CuPc(W) at 10mg/ml, bath soaked	3 layers of PVK at 10mg/ml, bath soaked	100nm of sputtered Platinum	all

Design	nc-TiO <sub>2</sub>	Dye layer	PVK layer	Contact	sintered
14	1 layer at 0.01g/ml	3 layers of RB (W) at 10mg/ml, bath soaked	n/a	100nm of sputtered Platinum	all
15	1 layer at 0.01g/ml	3 layers of RB (W) at 10mg/ml, bath soaked	3 layers of PVK at 10mg/ml, bath soaked	100nm of sputtered Platinum	all

key

PVK = poly(9-vinylcarbazole) in chloroform

CuPc(C) = chloroform soluble CuPc

CuPc(W) = water soluble CuPc

RB (W) is water soluble Rose Bengal

The chemical structures of the compounds listed in table 4.1 are given in fig 4.5 to 4.8.

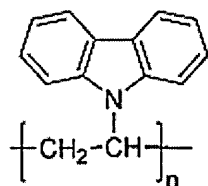


Figure 4.5. poly(9-vinyl carbazole)

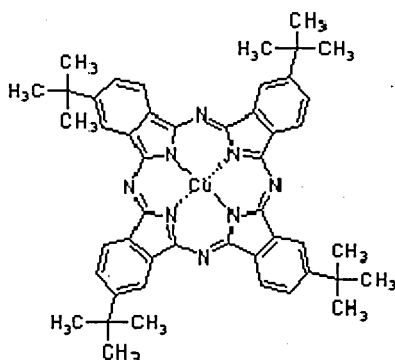


Figure 4.6. Copper(II) 2,9,16,23-tetra-tert-butyl-29H,31H-phthalocyanine (chloroform soluble CuPc).

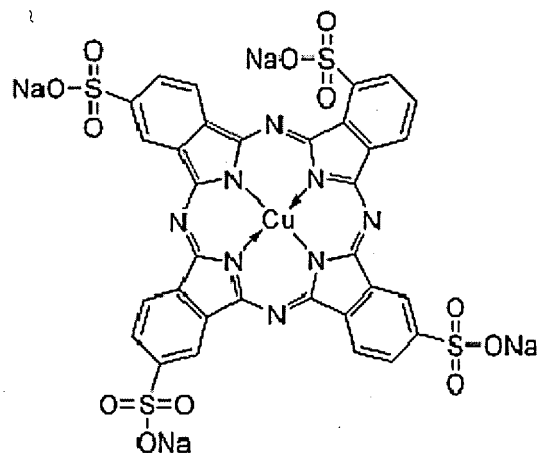


Figure 4.7. Copper phthalocyanine-3,4',4'',4'''-tetrasulfonic acid Tetrasodium salt (water soluble CuPc).

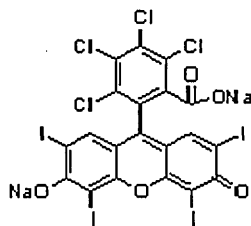


Figure 4.8. Rose Bengal.

All solution and suspensions were vigorously shaken before use and all except the chloroform solution were also ultrasonically agitated (again using the Kerry PUL55) to ensure that the solutions or suspensions were homogeneous (the chloroform might have evaporated too much through the heating effect of the agitation).

## 4.2. Structural Measurements

In this section, the methods of measuring the structural characteristics of samples are given. Such characteristics are the size of grains visible in the nano scale, or the type of chemical bonds present in a deposited material. Only the practical aspects of the methods are presented below as the theory of the methods is given in chapter 3.

### 4.2.1. Atomic Force Microscopy

The AFM measurements were performed using a Nanoscope IIIA on samples of TiO<sub>2</sub> on silicon wafer (for the sputtered samples) or on a glass slide (for the nc-TiO<sub>2</sub> samples). The sample size was kept to below 7mm square to ensure that they could fit in the AFM microscope. Great care was taken not to let anything touch the surface of the sample, or to let anything warm it up (e.g. by manhandling it), as this would otherwise produce trenches from scratches or smears from thermal drift respectively, in the scanned image. The tapping mode was used with an oscillation frequency of around 300kHz and drive amplitude of around 200mV, and a new tip was only installed if the existing tip started giving bad results. A scan area of 1μm square was used with a scan

time of 2 seconds per line. This was found to give good results (when the inevitable small amount of thermal drift had disappeared) that showed fine detail. Scans were subsequently plane-fitted to show remove large-scale (around  $1\mu\text{m}$  size) deviations. Roughness was calculated over the full area using the software and given as Ra (mean surface deviation from the mean height) and Rq (root of the mean of the square of surface deviation from the mean height). Grain size was measured by using the zoom and drawn line coordinated within Microsoft Paint. Using Microsoft Paint to measure the grain size is simple;

- The draw line tool shows the X and Y dimensions of the line being drawn - this can be used as a measure of distance in pixels
- Find the width of the scan picture in pixels and calculate nm per pixel
- Measure each grain size in pixels (best to do so in the same dimension each time e.g. width)
- Calculate grain size in nm
- Repeat for many (more than 20) grains and calculate grain size statistics for the sample

AFM has, in the past, been used to obtain images of such samples as; amorphous silicon posts etched from PDMS resist layer (7) and human lymphocyte metaphase chromosomes (8).

#### **4.2.2. Scanning Electron Microscopy**

The SEM scans were done on samples of sputtered  $\text{TiO}_2$  on Si wafer, using a Phillips XL40 ASEM/EDS instrument. The secondary electron emission mode was used with typical accelerating voltages of 10 - 20 kV. Samples were analysed for surface details including micro-cracks, particles on the surface, and homogeneity. This was kindly performed by Dr. Nabok of Sheffield Hallam University with my gratitude. SEM is a

very versatile imaging technique and can produce images of thick, delicate biological structures such as the detail of the head of a cat flea (9) and the spiny claw of a black widow spider (9).

#### **4.2.3. X-Ray Diffraction**

XRD patterns were obtained for the TiO<sub>2</sub> samples on Si wafer in order to determine their crystallographic phase. X-Ray diffraction patterns of resulting films were obtained using a Phillips PW1820 diffractometer with an 1130 generator. Radiation from a CuK $\alpha$  source, of wavelength  $\lambda=0.1540\text{nm}$  was incident on the sample. The 2-theta scan speed was kept very slow to allow a good measurement of the thin (200nm) films. The diffraction patterns were analysed for interplanar distance and miller indices, and phase was assigned.

#### **4.2.4. X-Ray Photoelectron Spectroscopy**

X-Ray photoelectron spectroscopy (XPS) analysis was performed in a vacuum of around  $5 \times 10^{-9}$  mbar using a Kratos Axis 165 XPS spectrometer equipped with an Al K $\alpha$  (1486.6eV) radiation source. The samples were annealed sputtered TiO<sub>2</sub> on Si wafer. Survey scans were performed at pass energy of 80eV. High-resolution scans were performed at pass energy of 20eV, and in this configuration the full width at half maximum (FWHM) peak of the Ag 3d 5/2 peak is around 0.6eV. The energy analyzer was calibrated using the Ag 3d and Auger lines prior to use. Scans were charge-corrected assuming a C-C peak position of 285eV. The data gave the types of oxide present. All the work on the samples including measurements and analysis was kindly performed by Dr. Mike Simmons with my gratitude.

#### **4.2.5. Surface 2-D Profilometry**

2D surface scans were performed using a Taylor Hobson Laser Form Talysurf MK1 to determine the thickness of the deposited films. The resolution of the Talysurf is 10nm over a 6mm long scan. Tip radius is approx 1.5 $\mu$ m to 2.5 $\mu$ m. Tip force is approx 0.7mN to 1mN. The samples were mounted on plasticene on the machine bed to give stability. Simple line fitting was done to remove any tilt on the sample, but no other filtering was performed. The measurements showed sample thickness and surface roughness on the micron scale.

#### **4.3. Electrical Measurements**

In this section, the methods by which the electrical characteristics of devices are obtained are presented. The characteristics usually come from analysis of commonly measured data, and such characteristics are conductivity of a material or the resistance added to the device by of the top metal contact.

##### **4.3.1. DC Voltage Characteristics**

Samples were subjected to a voltage stepped up from a negative lower limit up to a positive higher limit and the current for each voltage was measured. The measurement system comprises a Kiethley 6517a controlled by computer with a GPIB link.

Measurements were taken at intervals of more than 2 seconds to enable the sample characteristics to become steady at each voltage, if they would be otherwise. The samples were tested at room temperature and pressure, and where necessary, in a dark box, or under various illumination up to full simulated sunlight.

### **4.3.2. Load Resistance Characteristics**

To enable the fill factor of the solar cells to be determined, the cells were subjected to a variable load at room temperature and pressure and under full sunlight illumination. It is important to note that the tests were performed as quickly as possible, but with a five minute rest period between each test. This was done because the cell parameters degraded within the time frame of tens of seconds and didn't recover until after some time had elapsed. The duration of five minutes was arbitrarily chosen as a time that gave quite good recovery without the length of time being impractical. The parameter measured was the photovoltage, which was simply easier to measure due to being a larger value the photocurrent (which is close to the resolution limit of the equipment). For any given load, upon illumination of the sample, the photovoltage would climb swiftly to its maximum, and then die away slowly. This phenomenon was observed on an oscilloscope, with a slow time axis scan. The measured photovoltage was that at the maximum of the plot. The photocurrent can subsequently be calculated knowing the load resistance, by using Ohm's law.

## **4.4. Optical Measurements**

In this section, the methods by which the optical characteristics of samples are obtained are presented. Optical characteristics are those that are involved in some way with light, whether by absorbing the light, or even changing the polarisation of the light. Such characteristics are the absorption spectra of materials, and surface details in the micron scale.

### **4.4.1. Optical microscopy**

An optical microscope (Carl Zeiss Photomicroscope) with an attached digital camera (connected to a PC running capture and editing software) was used to take pictures at

the tens of microns to hundreds of microns level. Different magnifications were used to get details at different size regimes. The pictures were edited to improve contrast and sharpness of details. This allowed for very good pictures of the nanoparticle films, and the metal contacts applied to them.

#### **4.4.2. UV-Vis Absorption Spectroscopy**

The UV/Vis spectrometry was performed using a Unicam UV-visible Spectrometer, which is a dual beam spectrometer, and the baselines were normally set with glass slides. Absorption spectra were obtained for samples of TiO<sub>2</sub> and dyes (and mixes of the two) on cleaned glass slides and on F:TO coated glass slides. The spectra generally began at the onset of absorption of the glass slide (about 350nm) and ended at the end of useful data (such as when the interferometric fringes become too wide – about 800nm). Measurements were repeated at several locations on the samples to account for any non-homogeneity. Sample data were analysed in many ways; fitted to the Tauc model to obtain absorption model parameters, and refractive index and extinction coefficient spectra were obtained by Swanepoel's method, etc.

#### **4.4.3. Spectroscopic Ellipsometry**

To back up the analysis of the UV/Vis data, some parameters were obtained through spectroscopic ellipsometry of samples of sputtered TiO<sub>2</sub> on Si wafer. The Si mounted samples were chosen in preference to the glass mounted sample because of the difficulty of modelling a glass layer when analysing ellipsometric data. Psi-Delta scans were obtained using a J.A. Woollam Spectroscopic Ellipsometer. Data was fitted to the layer models shown in fig 4.9. Two different versions of TiO<sub>2</sub> were used as initial guesses for the two different samples.

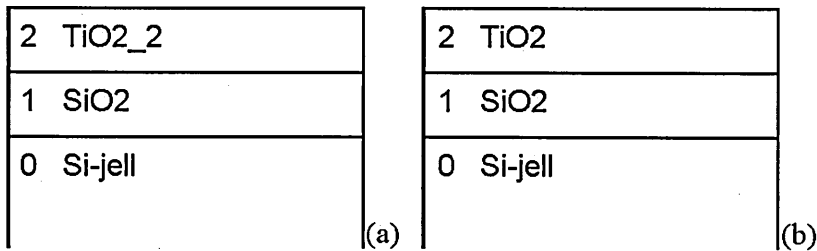


Figure 4.9. Layer models used for fitting ellipsometric data before (a) and after (b) the annealing procedure.

#### Reference List

- (1) Kron G., Egerter T., Nelles G., Yasuda A., Werner J.H., Rau U., Thin Solid Films 2002, 242–246, 403–404
- (2) Hagen J., Schaffrath W., Otschik P., Fink R., Bacher A., Schmidt H., Haarer D., 1997, 89, 215-220
- (3) Ma T., Inoue K., Yao K., Noma H., Abe E., IEEE Nano, 2001, 522-527
- (4) Sharma G.D., Sharma S., Roy M.S., Materials Science and Engineering 2003, B100, 13-17
- (5) Saito Y., Fukuri N., Senadeera R., Kitamura T., Wada Y., Yanagida S., Electrochemistry Communications 2004, 6, 71–74
- (6) Ravirajan P., Haque S.A., Poplavskyy D., Durrant J.R., Bradley D.D.C., Nelson J., Thin Solid Films 2004, 451 452, 624–629
- (7) <http://cmm.mrl.uiuc.edu/Gallery/AFM/AFMGallery.htm>. Accessed 7th September 2005
- (8) [http://www.jpk.com/spm/metaphase\\_chrom2\\_h.htm](http://www.jpk.com/spm/metaphase_chrom2_h.htm). Accessed 7th September 2005
- (9) <http://www.mos.org/sln/sem/sem.html>. Accessed 7th September 2005

## Results And Discussions

---

### 5.1. Sputtered TiO<sub>2</sub> Layer

The sputtered TiO<sub>2</sub> layer is the first layer deposited on the bottom electrode. Its purpose is to ensure that subsequent layers, especially the dye layer, do not make contact with the bottom electrode. The sputtered TiO<sub>2</sub> layer has been thoroughly tested to determine its structural, electrical and optical characteristics.

#### 5.1.1. Structural Characteristics

AFM scans of 200nm of sputtered TiO<sub>2</sub> on silicon wafer before and after annealing are shown in fig 5.1 and fig 5.2 for sample 1 and sample 2 respectively. The Z scale is shown for all scans. The two samples were prepared on 7mm square silicon wafer pieces and were touching each other and both near to the centre of the plasma stream in the sputtering chamber, so in principle, the films should be identical.

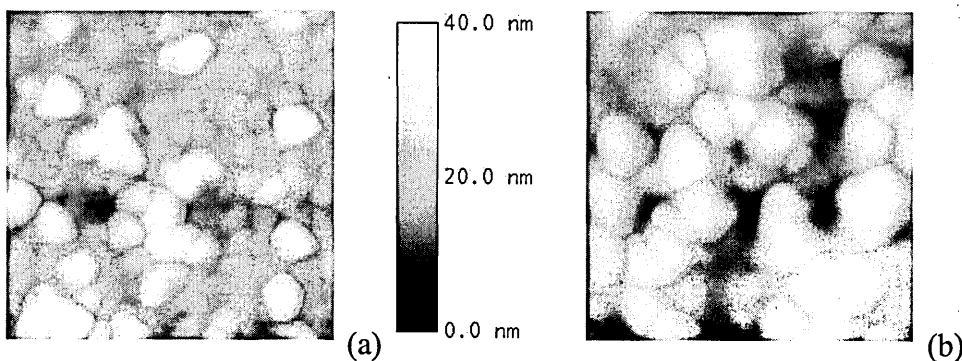


Figure 5.1. 0.5 $\mu$ m wide AFM scans of 200nm thick sample 1 of TiO<sub>2</sub> on Si wafer

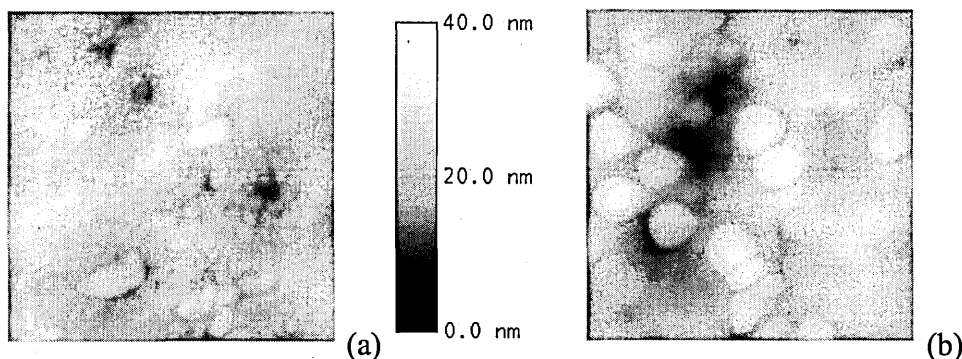


Figure 5.2. 0.5 $\mu$ m wide AFM scans of 200nm thick sample 2 of TiO<sub>2</sub> on Si wafer

The roughnesses calculated by the Nanoscope software across the entire 1 $\mu$ m by 1 $\mu$ m scan area of the samples, and the grain size statistics manually calculated are given in table 5.1. Both representations of roughness are shown for completeness.

Table 5.1. Calculated roughness and grain size statistics values for AFM images. All units in nm.

Sample	Roughness		White grain size		Grey Grain size	
	Ra	Rq	Mean	Std dev	Mean	Std dev
1 before	4.649	5.803	64.2	13.8	36.7	7.6
2 before	3.241	3.991	38.1	18.8	17.9	4.0
1 after	4.979	5.846	81.7	15.8	n/a	n/a
2 after	3.017	3.857	62.2	23.6	n/a	n/a

Since the AFM scans appear to contain 'white' and 'grey' grains (actually grains higher and lower on the surface respectively), which are quite different in size, statistics for each type are presented. In the annealed samples the only grains present are the 'white' type, so statistics for only these are shown. The white grains of sample 1 increase by 27.15% during annealing, whilst the white grains of sample 2 increase by 63.47%. The much larger increase of sample 2 is due to the very small initial size. In both cases, the grey grains have mostly disappeared or have aggregated so that their boundaries are not distinct. The grain sizes are in the same range as some published work (1;2) on DC sputtered films. It is interesting to note that the AFM images shown in fig 5.1 and fig 5.2 are of samples that should have identical properties. They were on identically

prepared substrates of silicon, they were positioned near to touching each other and near to the centre of the plasma beam, so they should experience the same deposition rate, etc. They appear to be more similar after annealing, and perhaps with extended annealing (1 hour or more for example), they will become the same. It will be seen later that there is evidence of a dispersion of deposition rates across samples, which is greatest near the centre of the beam, and decreases with distance away from the centre.

Overhead view SEM scans of a sample of 200nm of TiO<sub>2</sub> on silicon were performed and are presented in fig 5.3. The scale bars are 5 $\mu$ m (a), 50 $\mu$ m (b) and 100 $\mu$ m (c). In fig 5.3(c), the border between bare and coated silicon can be seen as a faint borderline sloping slightly up towards the right, which is marked out by the two arrows. The only details that can be seen elsewhere are particles of material probably laying on the surface, and aside from these, the sample is perfectly smooth and flat at these magnifications. Published work has shown (3;4) that the cross section of DC sputtered films is highly detailed with a thin columnar growth pattern prevalent. However, the surface is usually very smooth and only the slightly rounded tops of the columns may be seen. If images are taken perpendicular to the surface, the tops of the columns may not be seen clearly, as is the case in fig 5.3. This is a good attribute as the sputtered TiO<sub>2</sub> films are to be used as blocking layers and any defects or cracks would be detrimental.

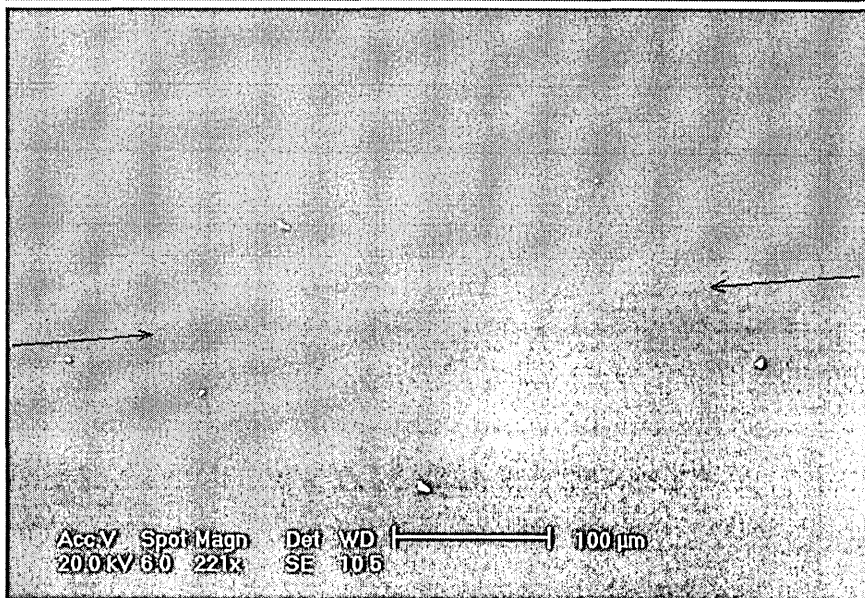
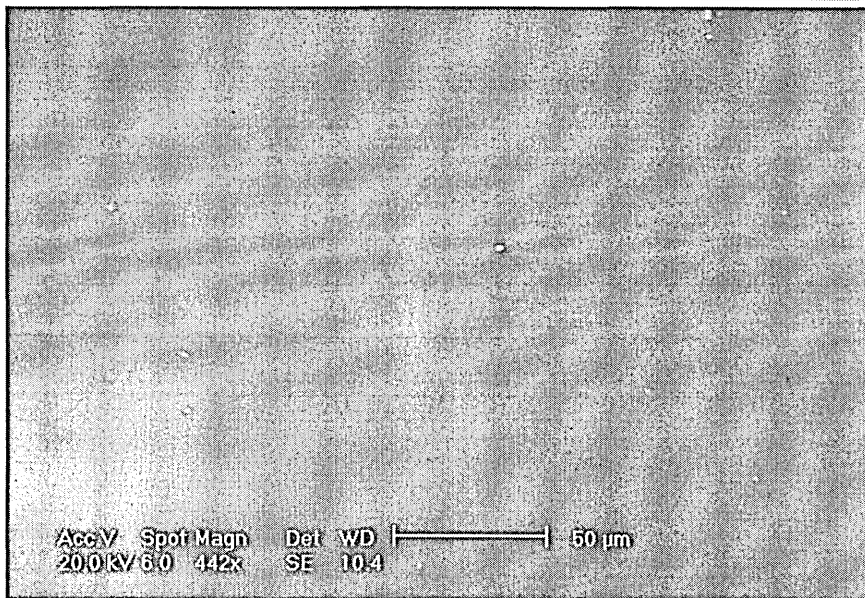
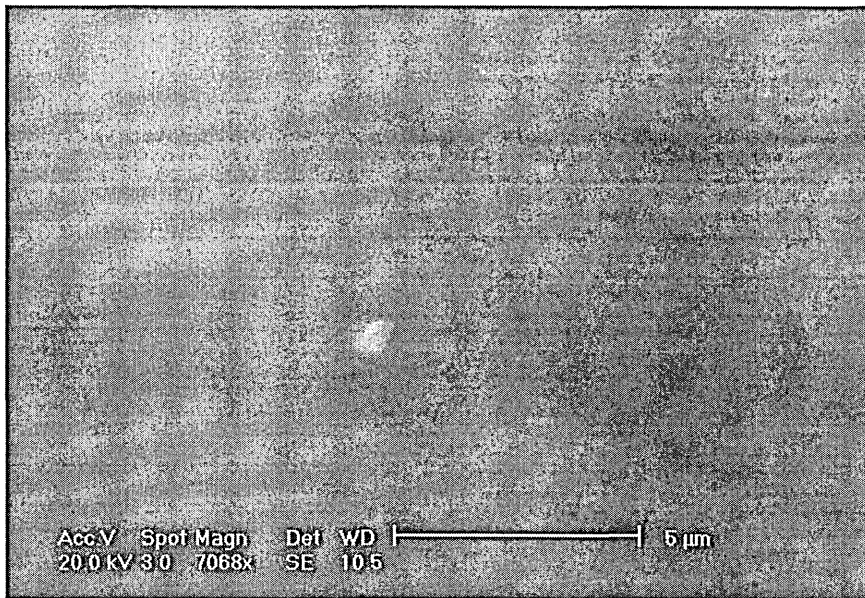


Figure 5.3. SEM scans of 200nm sputtered  $\text{TiO}_2$  on silicon. 5 $\mu\text{m}$  (a), 50 $\mu\text{m}$  (b), and 100 $\mu\text{m}$  (c).

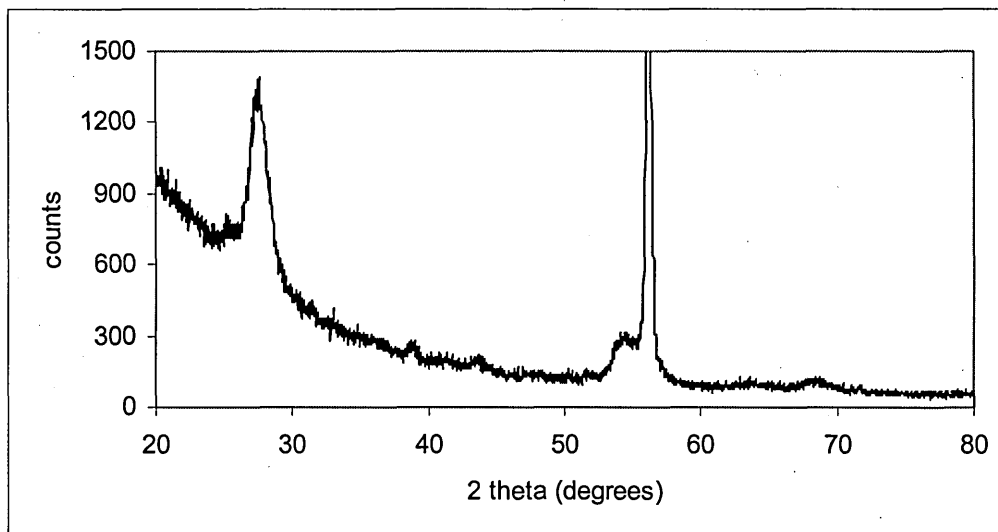


Figure 5.4. XRD spectrum of 200nm TiO<sub>2</sub> on silicon

A XRD diffractograph of a 200nm thick sample of sputtered TiO<sub>2</sub> is shown in fig 5.4. The off scale, narrow spike in fig 5.4 is attributed to the silicon substrate. The peak positions were calculated as the exact maximum of a third order polynomial fitted to the top points of the peak. The spectra on silicon had low intensity (due partly to a fast scan rate and partly to some proportion of amorphous material), and some peaks were very small, and were also on a curve. To make it easier to find the peak positions, a portion of the diffractograph, which was believed to contain four small peaks, was fitted to a 2<sup>nd</sup> order polynomial. The polynomial data was subtracted from the XRD data to give a near-horizontal diffractograph. This allowed the peaks to be easily identified, as only the heights of the peaks would be changed, leaving the critical x-position unaltered. The calculated peak positions, along with standard patterns for Anatase and Rutile TiO<sub>2</sub> are shown in table 5.2. The calculated lattice parameters are shown with the percentage error in table 5.3. It is clear that the measured pattern is closest to the rutile pattern, and thus the Rutile phase is assigned to the TiO<sub>2</sub> film. The standard XRD cards shows that the Rutile phase has a tetragonal atomic arrangement with dimensions of a and c being 0.45933nm and 0.29592nm respectively. The tetragonal crystal is based on a cuboid cell

with a square base and all internal angles being  $90^\circ$ . The peak marked “unclear” in table 5.2 is the one that lies at the same angle as the silicon peak ( $56.122^\circ$  according to the standard XRD cards) and is dominated entirely by the silicon peak. Published work shows (5-8) that to get the rutile phase dominating, one must either heat the substrate during deposition, or anneal the sample after deposition, or pulse the DC supply. None of these took place with the deposition of  $\text{TiO}_2$  films for this research, yet the films were Rutile dominant. This is a most interesting achievement.

Table 5.2. Comparison of experimental peak 2-theta positions and standard patterns

standard Rutile	standard Anatase	experimental values
27.446	25.281	27.482
36.085	36.946	36.287
39.187	37.800	38.746
41.225	38.575	41.204
44.050	48.049	43.604
54.322	53.890	54.444
56.640	55.060	unclear
62.740	62.119	68.223
64.038	62.688	
65.478	68.760	
69.008	70.309	
69.788	74.029	
72.408	75.029	
74.409	76.017	
76.508		
79.819		

Table 5.3. Comparison of experimental lattice parameters with true Rutile parameters.

	'a' on silicon	'c' on silicon
mean value (nm)	0.46226	0.29262
true value (nm)	0.45933	0.29592
error (%)	0.6382	-1.1149

X-ray Photoelectron Spectroscopy (XPS) was kindly performed by Dr. Mike Simmons of Sheffield Hallam University, to determine if it was indeed  $\text{TiO}_2$  that was being deposited and not some other oxide of Titanium. Dr. Simmons also performed the fitting procedure to extract the data. High resolution scans of the Ti 2p core level shown

in fig 5.5 revealed a Ti 2p<sub>3/2</sub> peak position of 459.0eV and a full width at half maximum (FWHM) of 0.91eV. This data showed good agreement with the work of Farfan-Arribas et al, who reported a value of 459.2eV and 1.19eV for the peak position and FWHM respectively. These values were ascribed to Ti<sup>4+</sup> in TiO<sub>2</sub>. There is no evidence for the existence of Ti<sup>3+</sup> at 457.4eV as has been reported in the literature. The O 1s peak was also well defined at 530.2eV, which showed good agreement with the value of 530.1eV reported by Zhang et al. Many published work (9;10) presented films with a deviation from stoichiometry due to various reasons. The films produced for this research were perfectly stoichiometric without having to use e.g. ceramic or sub-oxide targets for sputtering. Departure from stoichiometry can manifest itself as a dulling of the sample due to absorption by unoxidised metal in the film. This would lead to less light reaching the interface.

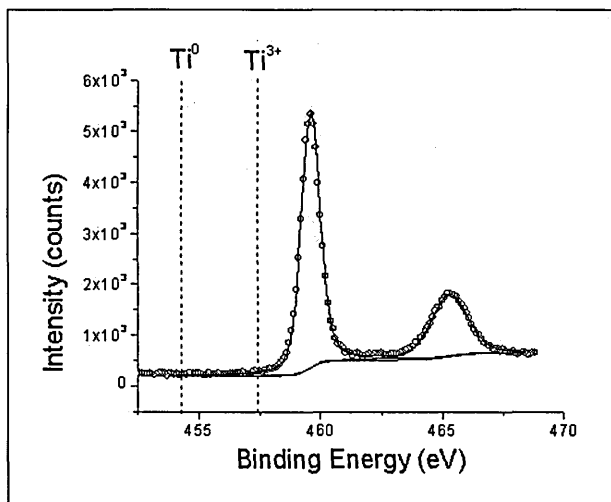


Figure 5.5. High resolution XPS scan of the Ti 2p core level

To demonstrate the lack of flatness on the microscopic scale of a standard glass slide (which was used as the substrate of many samples), a 2D profile scan was obtained and is shown in fig 5.6. As can be seen, the height of the slide above the lowest point varies by about 4 $\mu$ m across its length. Any deviations of height due to a film must have this artefact removed by some sort of fitting procedure.

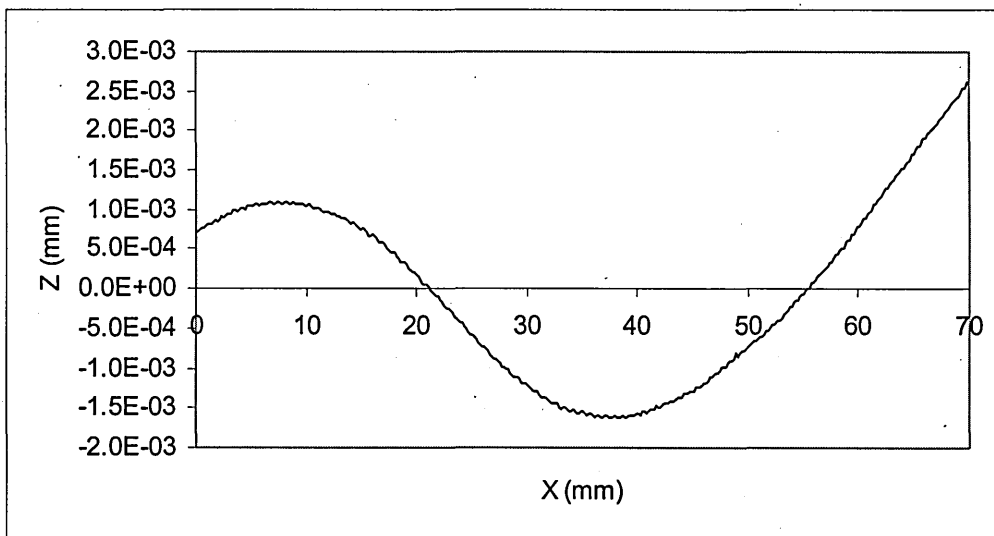


Figure 5.6. Microscopic 2D profile of a glass slide

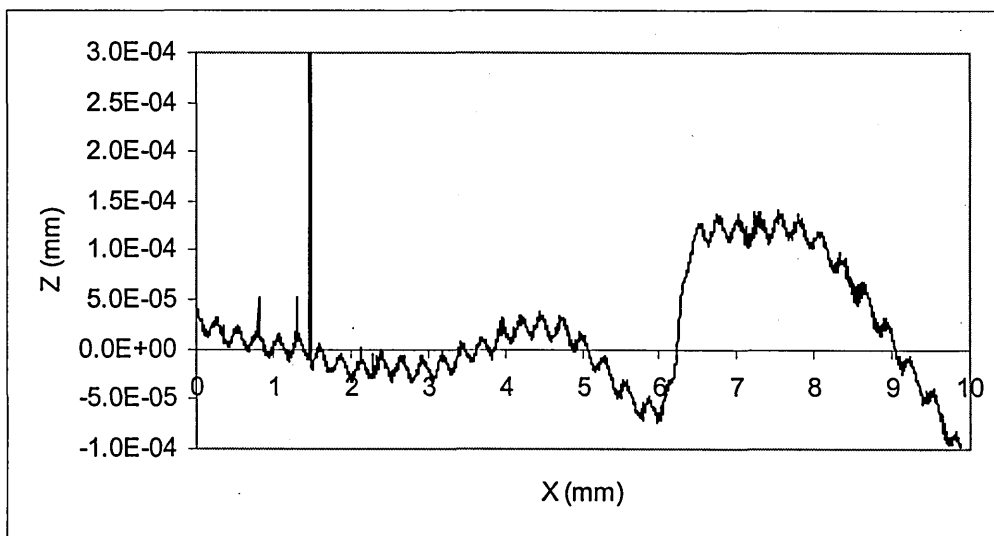


Figure 5.7. Microscopic 2D profile of 200nm sputtered TiO<sub>2</sub> on glass

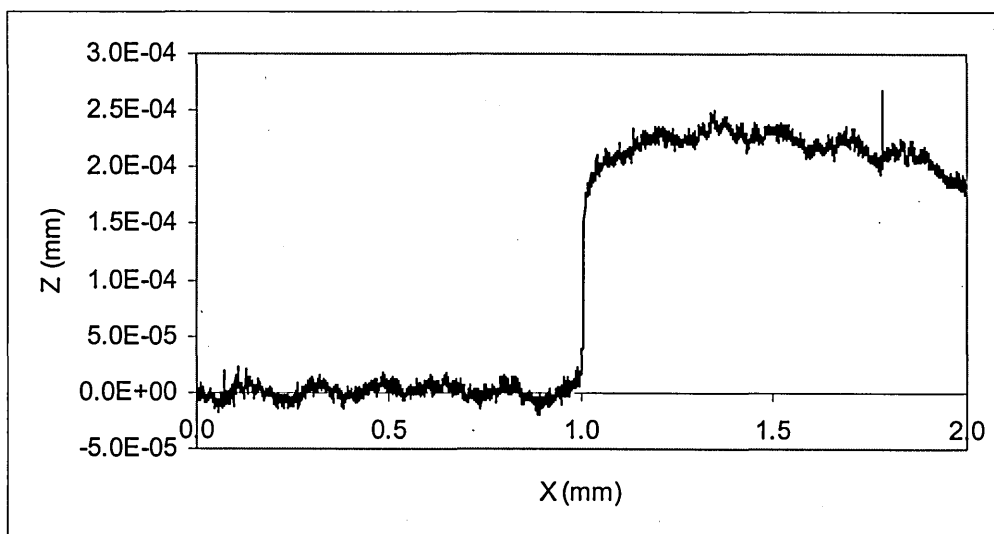


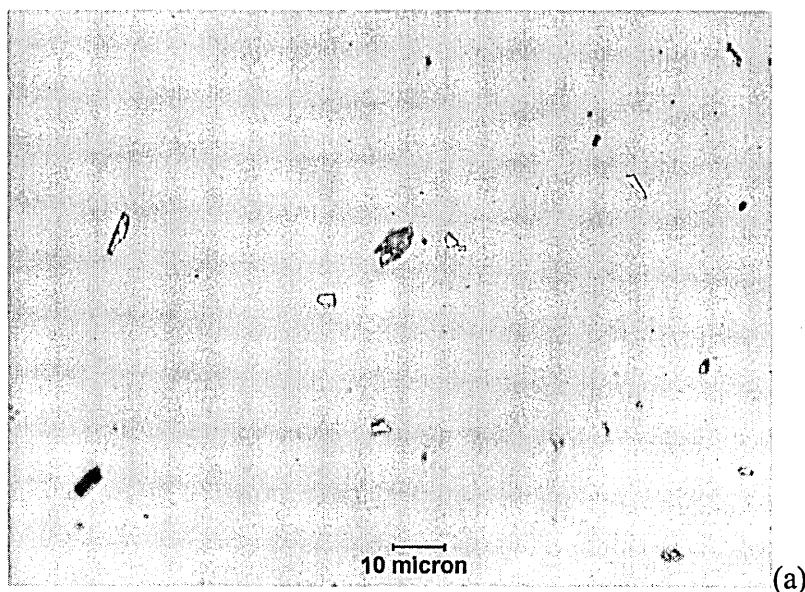
Figure 5.8. Microscopic 2D profile of 200nm sputtered TiO<sub>2</sub> on Silicon

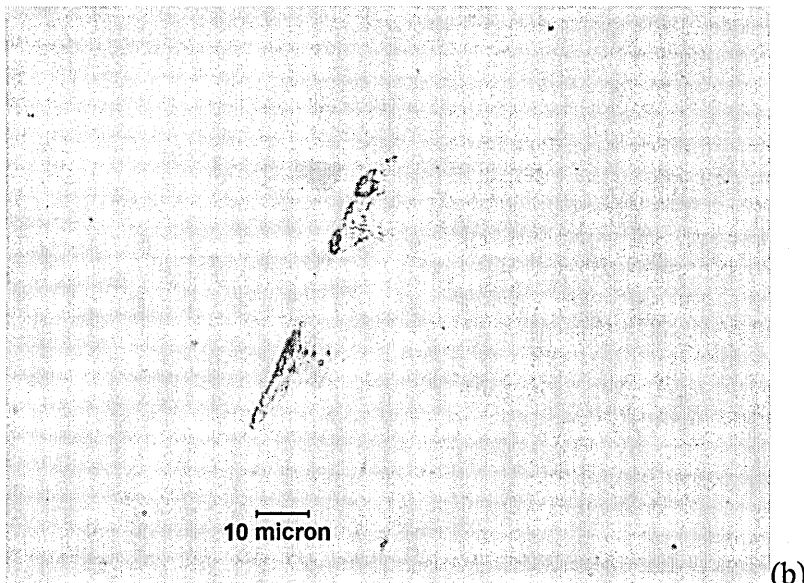
A profile of a sample of sputtered TiO<sub>2</sub> film on glass is shown in fig 5.7. Even after some fitting, the plots were far from the ideal situation of a sharp step up from one horizontal level to another, where the deposited film starts. A profile of a sample of sputtered TiO<sub>2</sub> on silicon wafer is shown in fig 5.8. Due to the extremely flat surface of the wafer, negligible large-scale deviations were seen, and the step was much clearer. The thickness of the TiO<sub>2</sub> film was easily determined to be about 200nm, which corresponded well with the in-situ QCM reading during deposition of 200nm.

The limit of height measurement resolution for the profilometer was around 10nm, so the thickness being measured (around 200nm) was approaching the limit of the equipment, which accounted for the noise oscillations seen in the thin film profiles.

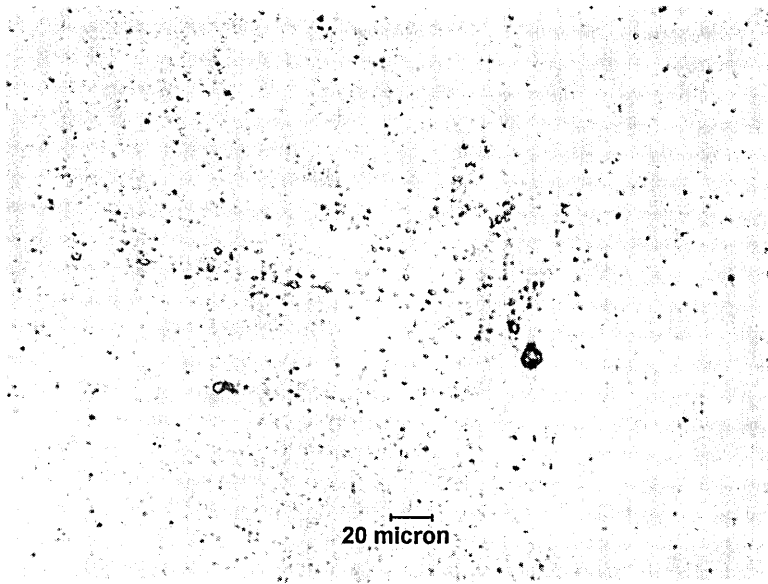
### 5.1.2. Optical Characteristics

The details shown in fig 5.9 are some of the *very* few patches of details on the samples' surfaces. The approximate sizes of the details are 3.0μm (a), 0.7μm, with larger details of around 21μm long (b), and 2.1μm (c).





(b)



(c)

Figure 5.9. Optical microscope pictures of three separate samples of 200nm sputtered TiO<sub>2</sub> on silicon

As with the SEM pictures presented earlier, a film lacking in details like microcracks and holes would do an excellent job of covering other layers and blocking any metal filaments. At this scale, as with the SEM, the sputtered TiO<sub>2</sub> films are virtually devoid of details, and can be assumed to be perfectly flat. The different colours seen in the optical microscope pictures are probably due to some sort of interference phenomenon as TiO<sub>2</sub> is transparent in the visible spectrum.

The amount of light that reaches the dye layer depends first on how much light is incident on the 'top side' (the side opposite the opaque metal contact), as some sunlight is lost due to absorption in the atmosphere and angle of incidence of the cell to the sun, and secondly it depends on how much light is absorbed by all the layers leading up to the dye layer e.g. glass substrate, F:TO layer,  $\text{TiO}_2$  layer etc. To determine the light losses, it is necessary to measure the absorption spectra of each layer. The sample substrates (plain glass slide and F:TO coated thick glass slide) were measured first and their UV-Vis absorption spectra are shown in fig 5.10 and fig 5.11. The wavelength ranges are all kept the same, for ease of comparison. Each substrate was measured at three positions for repeatability, and as is common with commercial products, there is very little dispersion between them. The F:TO coated thick glass slide shows signs of oscillations. This might have been due to interferences effects in the coating, or a result of actual absorption in the coating. Clearly, a glass slide absorbs (or reflects, it does not matter because either way the light is lost) 10% in the 'transparent region' and increasing amounts of light lower than about 350nm. The F:TO coated glass is much worse; at least 20% is lost in the transparent region and increasing amounts past about 350nm partly due to the F:TO and partly due to the (thicker) glass substrate. This will ultimately result in at least 20% loss in efficiency. Other types of solar cells such as those based on Silicon wafer can use a fine grid of metal contacts to carry away the photocurrent. The grid is fine enough so as not to block the light by very much and all of the rest of the light can be incident on the cell (there would probably be a protective glass covering of high band gap to let through most of the light as well). The grid design would not be practical for the dye sensitised cell, as the planar resistance is huge and would produce devastatingly high series resistance. It works for the Silicon cell as the Silicon is of low resistivity.

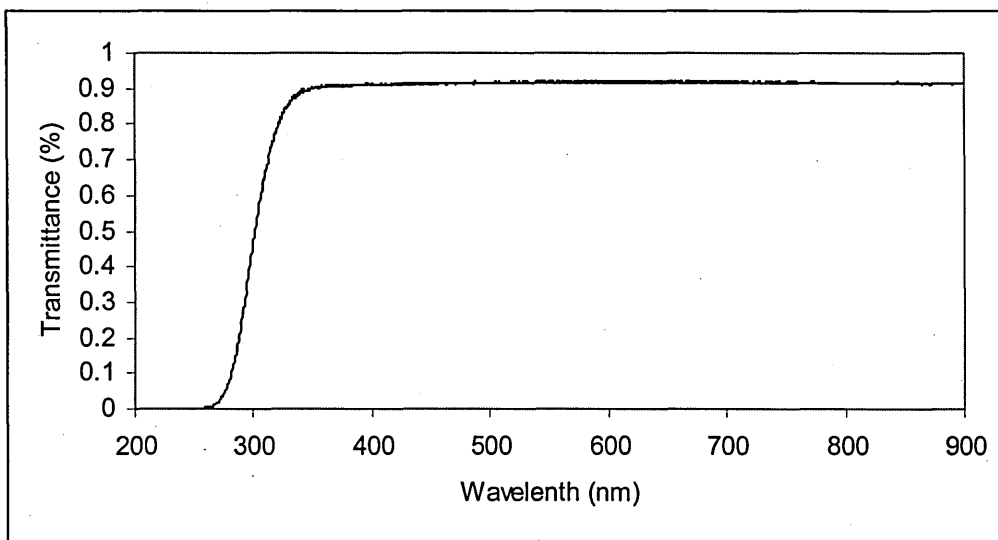


Figure 5.10. Transmittance spectra of a glass slide

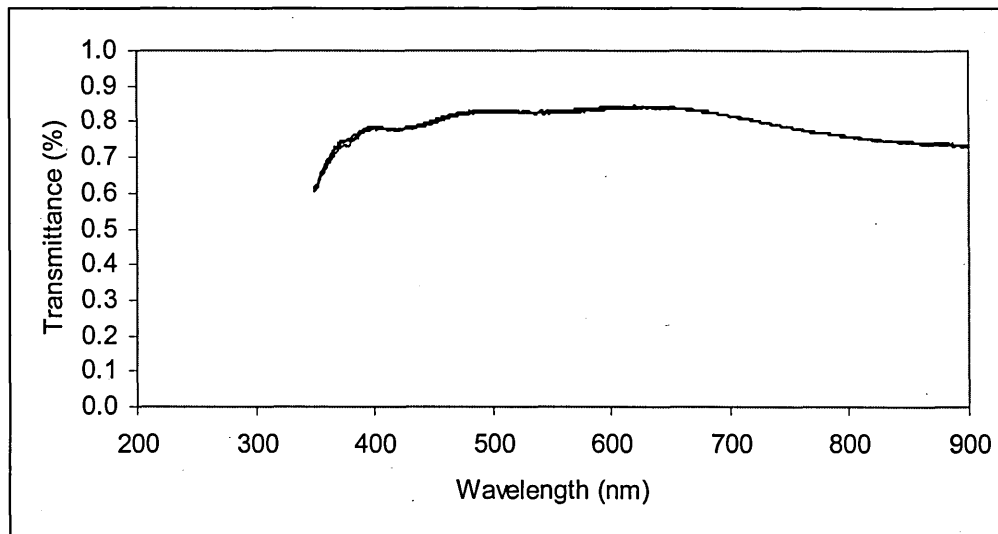


Figure 5.11. Transmittance spectra of a commercial FTO coated glass slide

Several parameters can be obtained from the UV-Vis spectra of the  $\text{TiO}_2$  films such as refractive index spectra and film thickness. The effect of the absorption by the glass slide substrate has been removed from all the data. Two samples (A and B) were both tested at two different positions, to account for any changes due to the slight inhomogeneity in the film (the clip used to attach the substrate to the holder partly shadowed the deposition and it was believed that the UV-Vis spectrometer would pick up part of the shadowed area as well as the fully coated area). One sample was annealed

and tested twelve times at different locations, as the annealing process had exaggerated the inhomogeneity. Several Uv-Vis spectra for the unannealed samples (A and B) and the annealed sample are shown in fig 5.12 and fig 5.13 respectively (several spectra were taken to observe repeatability). The spectra in fig 5.12 and 5.13 show significant variation in the heights and positions of the fringes, although the number of fringes remains constant. There appears to be more variation in the spectra of fig 5.13, despite the fact that they were all obtained from a single sample (at many points along its length), which would suggest that the annealed sample suffers from lower homogeneity. One spectrum for each sample was analysed by the Swanepoel method and the results are shown in fig 5.14 for the unannealed sample, and fig 5.15 for the annealed sample respectively.

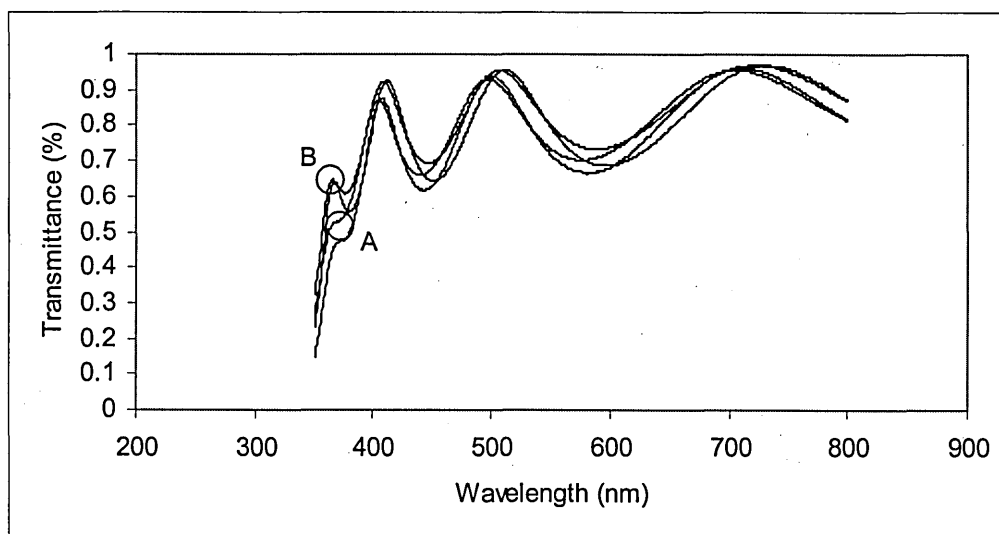


Figure 5.12. Transmittance spectra of sputtered TiO<sub>2</sub> on glass slides (unannealed)

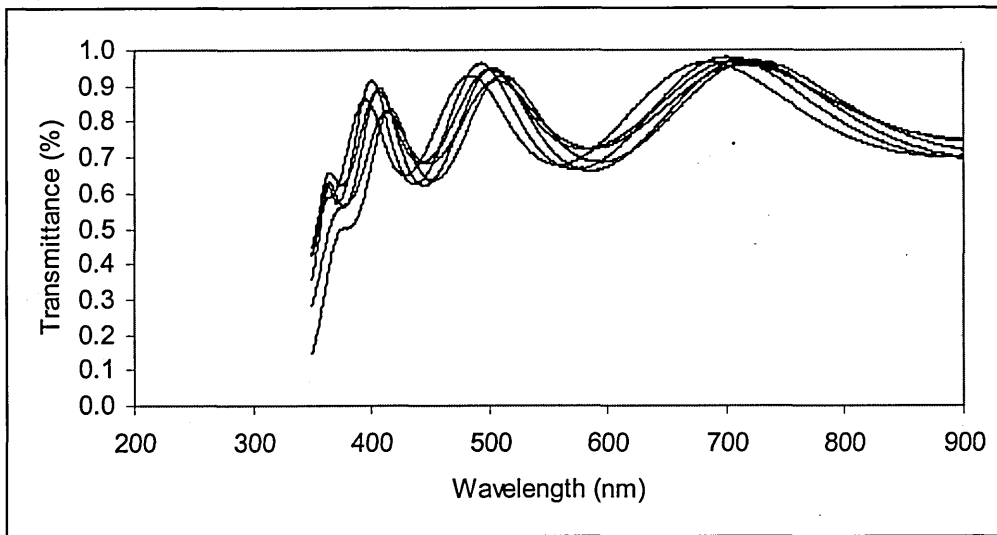


Figure 5.13. Transmittance spectra of sputtered TiO<sub>2</sub> on glass slide (annealed)

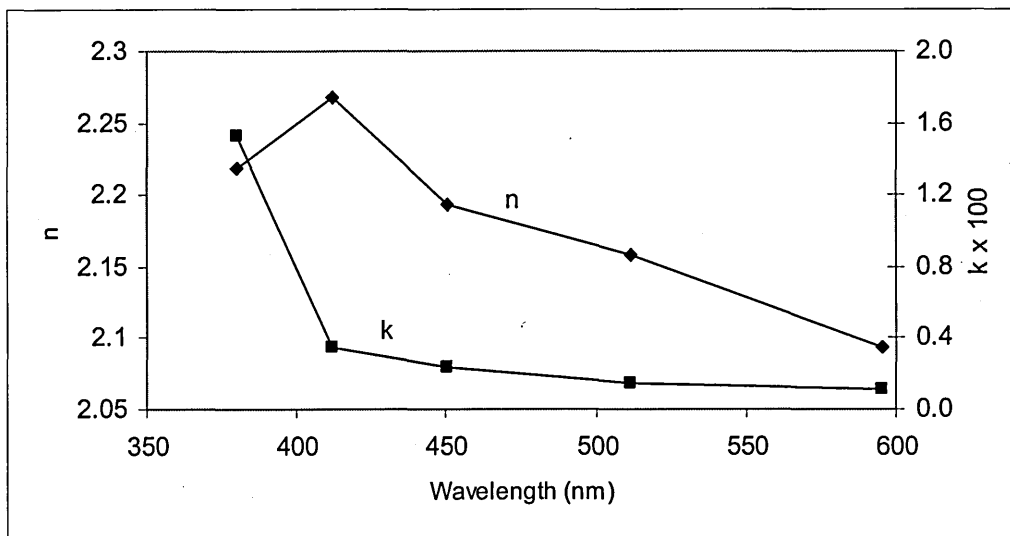


Figure 5.14. Swanepoel fitting of a spectrum from sputtered TiO<sub>2</sub> before annealing

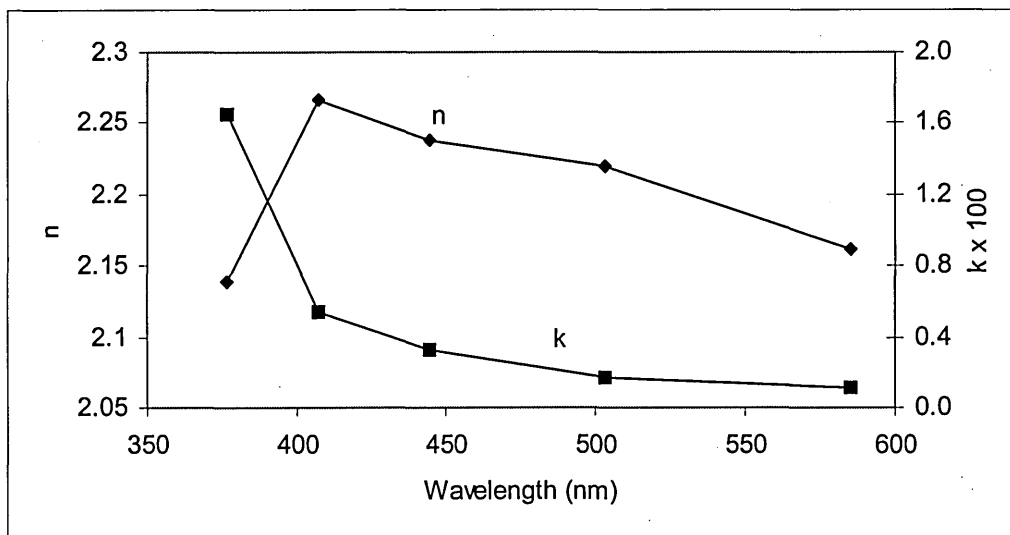


Figure 5.15. Swanepoel fitting of a spectrum from sputtered TiO<sub>2</sub> after annealing

The values of refractive index and extinction coefficient are well within the ranges presented in some published work (11;12). From equation 3.31, the thicknesses for the unannealed and annealed samples were found to be 359.5nm and 400.9nm respectively. It is interesting to note that the thicknesses obtained via the Swanepoel method are all much larger than that shown by the QCM during deposition and the 2D profiles. The samples were laid flat against an aluminium support during deposition, so there should not be any material deposited on the back of the glass slides, which might have appeared to add to the effective thickness. The procedure was tested with the parameters given in Swanepoels's published work (13), and the results obtained matched very well with his results, and therefore, the author is confident of the results obtained for this research. The refractive indices for all samples are close to those for the material files from the WVase software. Because the thickness is derived from wavelength and  $n$ , if  $n$  is accurate, and wavelength is accurate (there is no reason why it should not be), then  $d$  should be accurate. The reason for the discrepancy is unknown at the present.

Table 5.4. Results of the fitting of absorption spectra to the Tauc model

Spectra	C	EO (eV)	n	R squared	Assigned transitions
A 1 (unannealed)	32.5999	3.0179	3.0	0.999802	indirect forbidden
A 2 (unannealed)	54.3523	3.1903	2.0	0.999726	indirect allowed
B 1 (unannealed)	39.5757	3.3019	1.6	0.999689	direct forbidden
B 2 (unannealed)	34.6172	3.3658	1.1	0.999858	ambiguous
1 (annealed)	7.8439	3.3821	0.55	0.999455	direct allowed
2 (annealed)	8.6618	3.3601	0.65	0.999224	direct allowed
3 (annealed)	28.8916	3.1868	2.0	0.999833	indirect allowed
4 (annealed)	28.1218	3.2009	1.9	0.999723	indirect allowed
5 (annealed)	25.6622	2.9009	3.0	0.999718	indirect forbidden
6 (annealed)	24.5944	2.8826	3.1	0.999679	indirect forbidden
7 (annealed)	16.0931	2.9690	2.3	0.999483	ambiguous
8 (annealed)	177.7503	3.3187	2.1	0.999640	indirect allowed
9 (annealed)	13.8250	3.2753	1.2	0.999369	ambiguous
10 (annealed)	14.5140	3.2573	1.3	0.999819	ambiguous
11 (annealed)	11.8899	3.2539	1.1	0.999297	ambiguous
12 (annealed)	8.5547	2.8334	3.0	0.998388	indirect forbidden

All of the spectra, both annealed and non-annealed were fitted to the Tauc model (by the Vale Tauc model fitting method). The results of the entire fitting, including the error statistic,  $R^2$ , are shown in table 5.4. The Tauc parameters for the unannealed samples are labelled A1, A2, B1 and B2. The Tauc parameters for the annealed sample are labelled 1 to 12.

The index  $n$  represents the type of band gap present in the material. It is interesting to see from table 5.4 that the index varies dramatically between different spectra from the same sample even though the Tauc model fits are very good (the  $R^2$  values are very close to 1.000). This implies that different regions of the material have quite different optical characteristics in terms of their band structure. It is believed by some researchers that materials with a degree of amorphicity will show some variance in the index  $n$ . The variety of indices in table 5.4 includes values presented in some published work (14;15). The bandgap of the materials is show by column  $E_0$ . Ignoring the values of  $E_0$  that are far from the mean, the mean value is 3.27eV. This value is in good agreement with published work (14;15).

To compliment the analysis of the absorption spectra, the  $n$  and  $k$  spectra and thickness of sputtered  $TiO_2$  films on silicon wafer, were determined by spectroscopic ellipsometry and subsequent model fitting. Various Phi-Delta spectra of the samples were obtained at different angles of incidence and location to account for any nonhomogeneity and to observe repeatability. The results of the fitting are shown in fig 5.16, fig 5.17, fig 5.18, and fig 5.19, for sample B and C before annealing and then sample B and C after annealing respectively. The spectra in fig 5.16 and fix 5.17 are labelled according type ( $n$  or  $k$ ) and number e.g.  $n(1,2)$  refers to refractive index spectra 1 and 2. Clearly, the

fitting results are not consistent because the  $k$  spectra varies wildly, and the  $n$  spectra has a shift that is thickness-guess dependent.

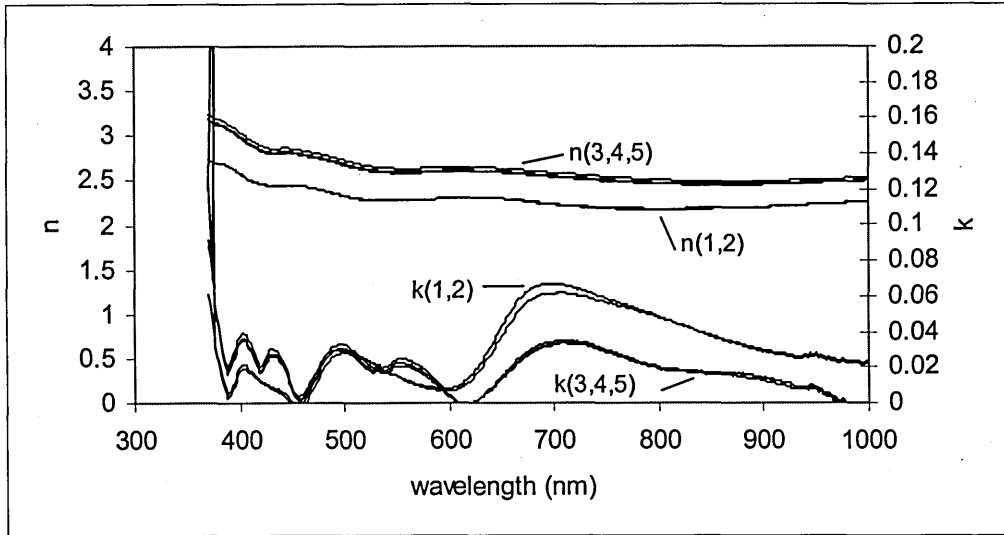


Figure 5.16.  $n$  and  $k$  spectra of sample B before annealing.

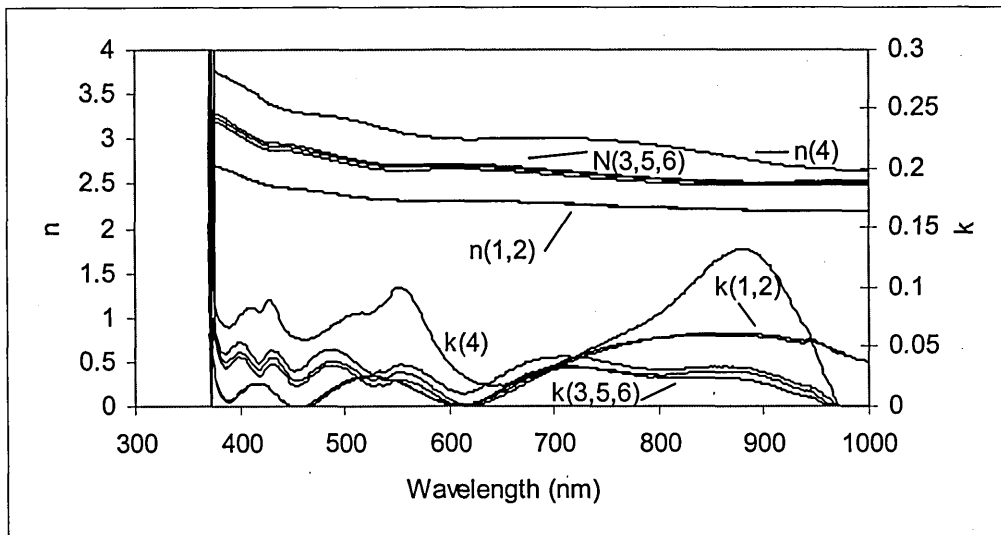


Figure 5.17.  $n$  and  $k$  spectra of sample C before annealing.

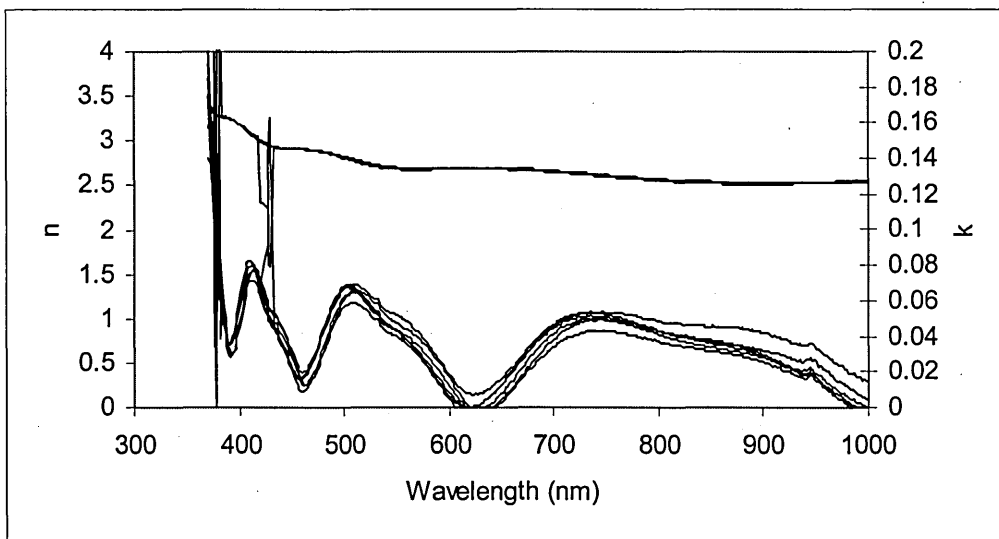


Figure 5.18. n and k spectra of sample B after annealing.

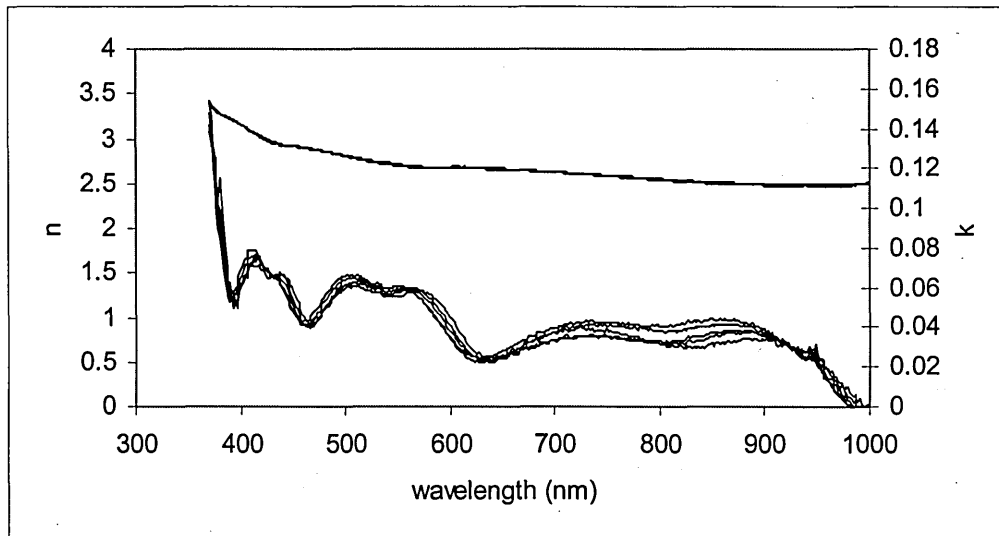


Figure 5.19. n and k spectra of sample C after annealing.

The thickness values of the  $\text{TiO}_2$  and  $\text{SiO}_2$  films obtained from the fitting procedure are shown in table 5.5. The numbering in table 5.5 is the same as that in fig 5.16 and fig 5.17.

It is clear from the table and figures that a large refractive index gave a low fitted thickness and vice versa. The thicknesses after fitting are close to the initial guesses.

Therefore, neither set of data was reliable. The extinction coefficient is inappropriate as the spectra should be smooth and flat past the band gap, which is not seen in the spectra obtained. The thickness obtained for the  $\text{SiO}_2$  layers vary by an order of magnitude and

vary inversely with the thickness of the TiO<sub>2</sub> layers. It is most unfortunate that none of the ellipsometric data can be relied upon.

Table 5.5. Comparison of thicknesses of TiO<sub>2</sub> and SiO<sub>2</sub> obtained from ellipsometry for samples 1 and 2 each with 5 or 6 ellipsometric fits.

Spectra	TiO <sub>2</sub> (nm)	SiO <sub>2</sub> (nm)
1 before 1	313.4	10.04
1 before 2	313.1	10.70
1 before 3	256.8	27.11
1 before 4	258.5	26.40
1 before 5	251.7	28.59
2 before 1	314.7	3.09
2 before 2	314.6	3.29
2 before 3	251.1	24.65
2 before 4	202.4	46.48
2 before 5	241.5	29.84
2 before 6	245.7	27.07
1 after 1	248.3	29.56
1 after 2	247.2	33.76
1 after 3	248.0	30.30
1 after 4	248.0	30.36
1 after 5	247.4	33.65
1 after 6	247.2	34.64
2 after 1	247.4	33.23
2 after 2	247.2	33.54
2 after 3	247.0	33.74
2 after 4	247.2	35.58
2 after 5	247.0	36.76

### 5.1.3. Electrical Characteristics

Two samples of sputtered TiO<sub>2</sub> were tested for the resistance in the planar direction (not down through the film) as the resistance between two adjacent fingers of platinum that were sputtered on through a mask. The devices are labelled according to what pair of fingers isolates them, e.g. device 3-4 is comprised of TiO<sub>2</sub> with contacts formed by finger 3 and finger 4. The fingers are numbered 1 to 6 along the length of the sample. A diagram of a sample is shown in fig 5.20. One sample was annealed before the fingers were applied. The I(V) spectra for each device are shown in fig 5.21 and fig 5.22 for before annealing, and fig 5.23 for after annealing. Two spectra are obtained for each device to observe repeatability. There is significant noise in fig 5.21, and variation

within pairs of spectra for devices in fig 5.21 and 5.23. The consistency of the spectra improves with increasing current from the pA range to the  $\mu\text{A}$  range.

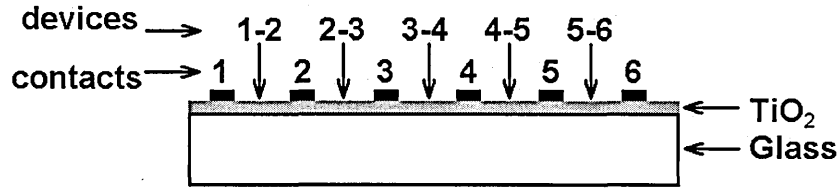


Figure 5.20. Schematic of a planar TiO<sub>2</sub> sample.

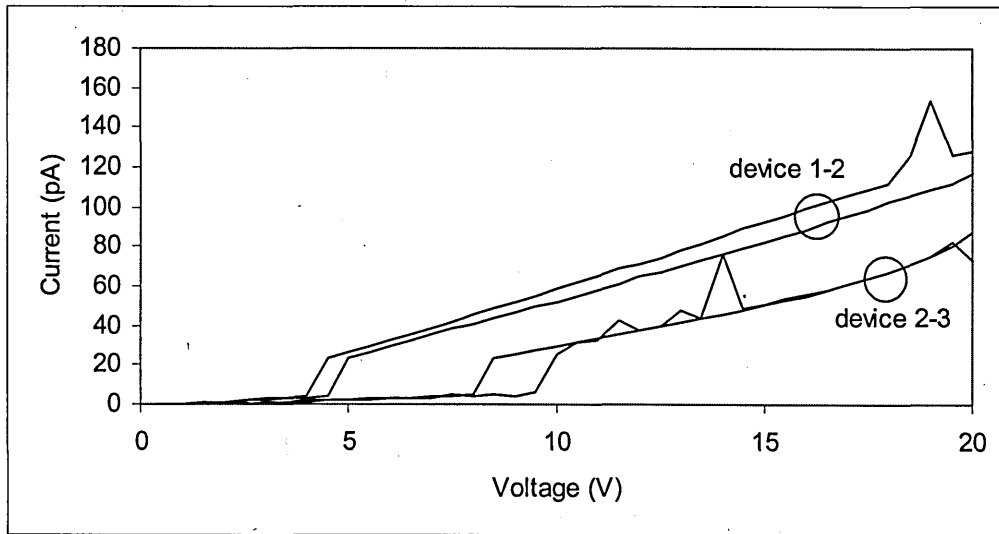


Figure 5.21. Devices 1-2 and 3-4 of TiO<sub>2</sub> before annealing.

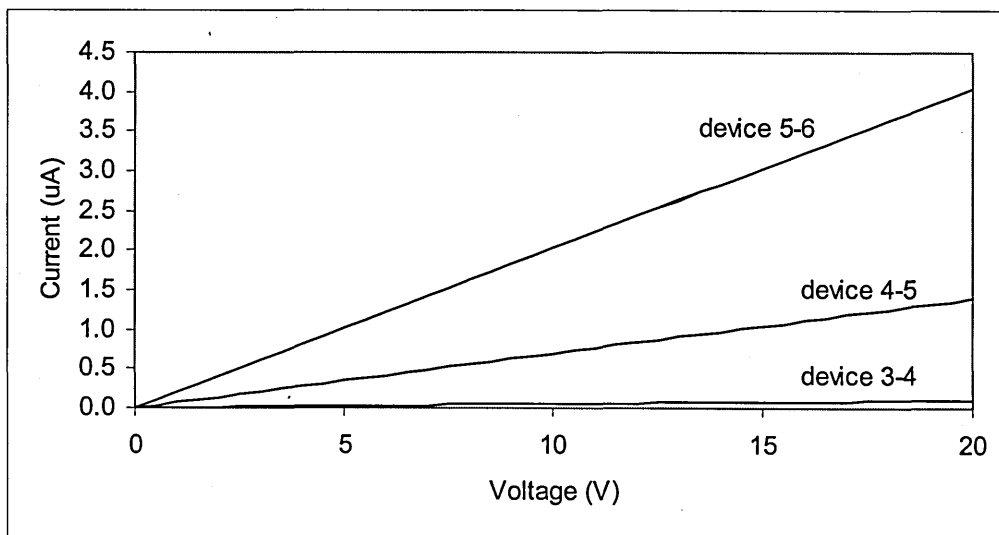


Figure 5.22. Devices 3-4, 4-5, and 5-6 of TiO<sub>2</sub> before annealing.

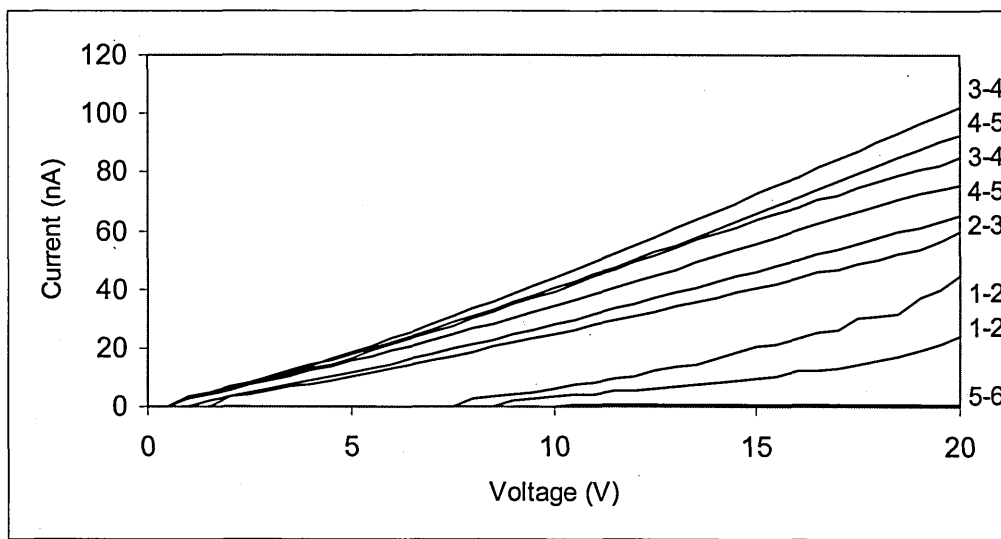


Figure 5.23. All devices of TiO<sub>2</sub> after annealing.

The resistance of the devices was calculated by a linear fitting of the current. The average planar resistance and conductivity of the films, given in table 5.6, were calculated as the mean resistance of the device 3-4 (the devices in the centre of the film and more likely to represent the typical thickness) for before and after annealing. The conductivity was calculated from;

$$R = \frac{L}{\sigma A} \quad (5.1)$$

This assumes the devices are cuboids with dimensions given in below. The calculated conductivities are several orders of magnitude smaller than that published for TiO<sub>2</sub> sputtered films (1;2). The values may be slightly inaccurate as evidenced by the noise in the I(V) graphs. Device dimensions are; length  $3 \times 10^{-3}$  m, area  $1.8 \times 10^{-9}$  m<sup>2</sup>.

Table 5.6. Comparison of average planar resistance and conductivity of TiO<sub>2</sub> before and after annealing

Annealing	resistance (Mohm)	conductivity (1/ohm m)
before	191.509	0.00870
after	207.358	0.00804

As with the bridge tests shown below, there is evidence of thickness dispersion. The resistance of the devices tends towards higher values at the centres of the samples. It is likely that the centres were nearer the sputtering source and got more of the material, giving a thicker film. The dispersion of thickness in the fingers will not affect the results as the device resistances is five orders of magnitude greater than the finger resistance.

## **5.2. Nano Powder TiO<sub>2</sub> Layer**

The porous TiO<sub>2</sub> layer is the second layer deposited in the device. Its purpose is to create a massive increase in the surface area of the TiO<sub>2</sub> layers to give a greatly extended area of interface between the TiO<sub>2</sub> and the dye. The porous TiO<sub>2</sub> layer has been analysed in various ways to determine its structure.

### **5.2.1. Structural Characteristics**

To study the nanoscopic details of Degussa P25 films, AFM scans were obtained of P25 powder films on glass, which are shown in fig 5.24 for before annealing (a), and after annealing (b). Roughness values (calculated by the Nanoscope software) and grain size statistics are given in table 5.7. The grain sizes, which are much larger than the actual stated particle size of the commercial powder, probably due to aggregation, are about half that of some published work (16) using P25, suggesting less aggregation in samples produced for this research. The roughness given in some published work (16) is less and the general homogeneity is better than the samples produced for this research, although good homogeneity in the porous films is not the aim of the work. The Z range has been included because the variance in height of the powder films is substantial. The two images are of different points on the sample, as trying to relocate the point after removing the sample to a furnace and reinstalling it is virtually impossible, and any specific differences are due to this fact as opposed to being due to the annealing process.

General differences may be due to the annealing process. It is interesting to note the large difference in appearance between the two samples. The image (a) seems to be made of rows of particles lying diagonally across the image and terminating around certain locations. It is not believed that these are due to particles on the scanning tip as the details would be mostly horizontal lines with sharp changes (such as when a particle drops off the tip), or due to thermal drift as the details would have a smeared appearance and the ends of the rows would taper gradually instead of ending in a round shape. It could be that in this area, the particles are dragged across the sample (considering the tipping action during the flood printing process) and line up as rows in the direction of the global (or local) movement of the particle suspension during deposition. The image (b) is more like what was expected of a particle film, as there are general clumps and pits and caverns within the structure, which gives the film its large surface area.

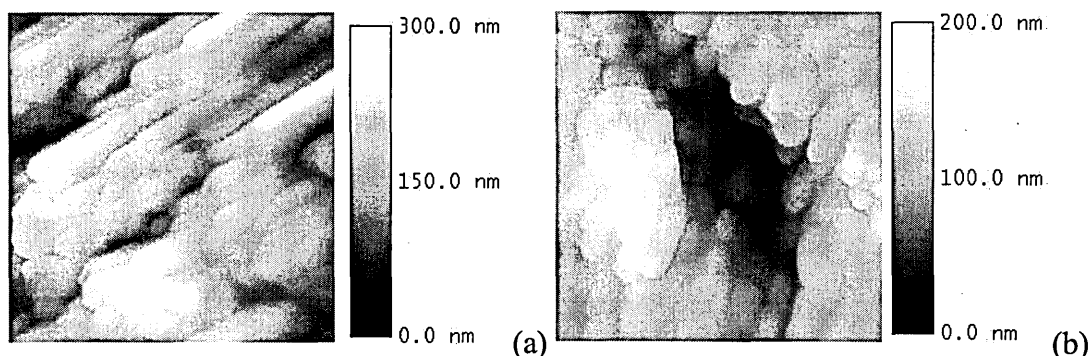


Figure 5.24. 0.5µm wide AFM scans of nanoparticle films of TiO<sub>2</sub>

Table 5.7. Grain size statistics and calculated roughness values for AFM scans of unannealed and annealed P25 films on glass. All dimensions are in nm.

Annealing	Ra	Rq	Z range	mean grain size	std dev grain size
before	38.17	47.21	311.67	41.54	7.47
after	28.42	36.59	335.24	45.38	6.92

The data in table 5.7 show a highly rough film (less rough after annealing) with a particle size that has a small range of variation that increases slightly with annealing.

The stated particle size for the nano TiO<sub>2</sub> is around 25nm - about half of that which can be seen in fig 5.24. It is either the case that the commercial powder used had larger

particles than stated (unlikely), or that the particles formed tight clusters of several particles that themselves formed up randomly into the observed films.

Samples of P25 films on glass slides were produced with varying concentrations of P25 to Millipore water to see if the concentration may change the thickness or roughness of the film. Typical profiles for concentration are shown in fig 5.25, fig 5.26, and fig 5.27 for 25mg/ml, 50mg/ml, and 100mg/ml respectively. The mean height of the film is shown as a thick horizontal line on each profile.

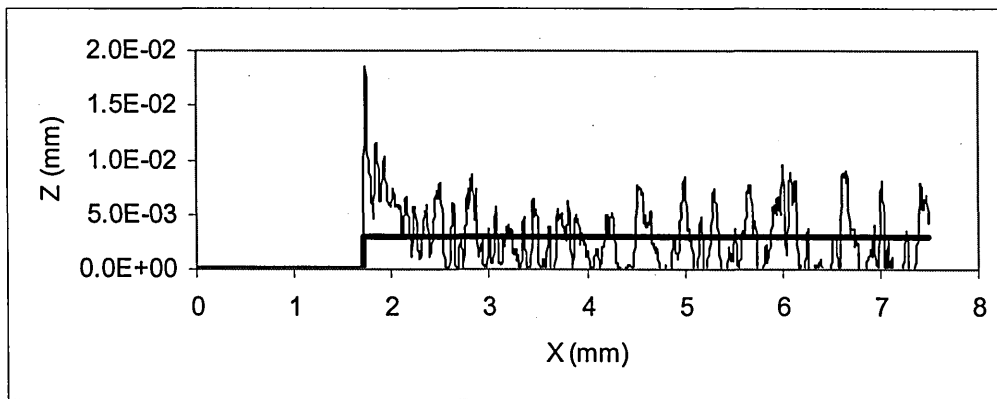


Figure 5.25. Microscopic 2D profile of 25mg/ml P25 film on glass

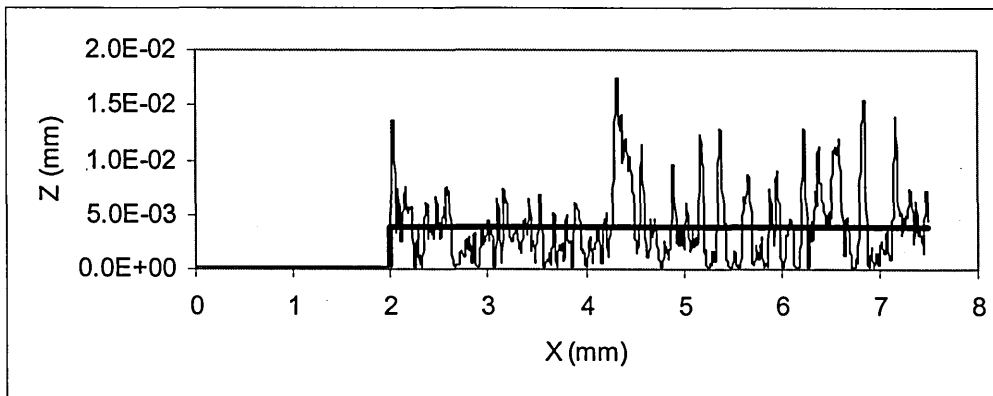


Figure 5.26. Microscopic 2D profile of 50mg/ml P25 film on glass

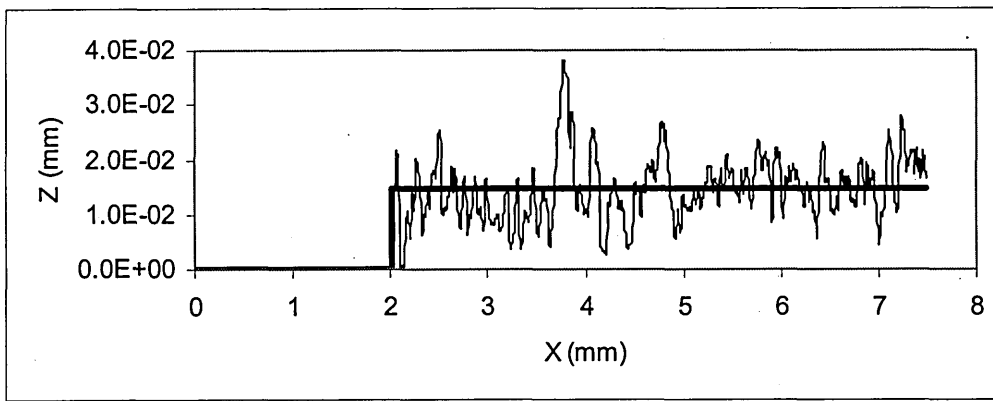


Figure 5.27. Microscopic 2D profile of 100mg/ml P25 film on glass

Each concentration was tested as a pair of samples (A and B), and each sample was tested in three locations; near the left edge, near the centre, and near the right edge, to see if the height varied macroscopically across the sample, but only one profile for each concentration is shown to make them easier to see. The summarised data for the mean heights of the samples at each location are shown in table 5.8. The column headings refer to the concentration and either sample A or B.

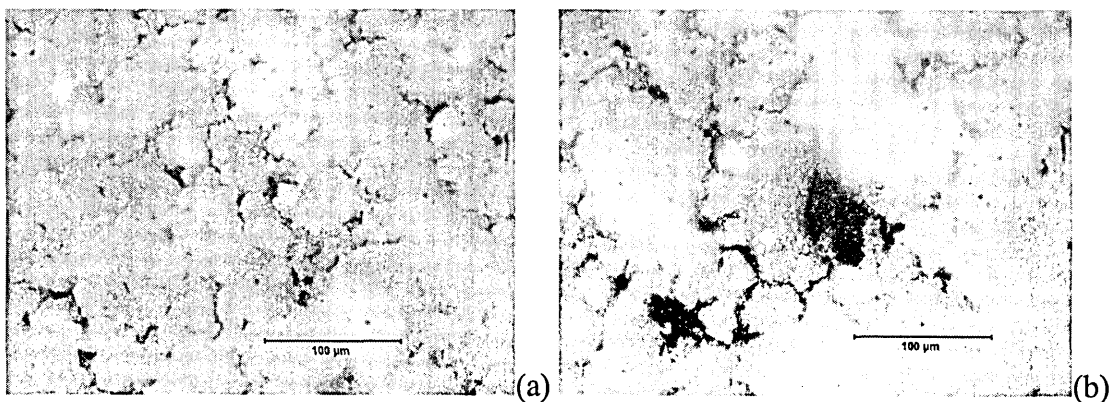
In a very general way the thickness is higher at higher concentrations. The thickness does not appear to be significantly dependent on concentration at lower concentrations. The thickness is clearly quite random at all points of a sample (which is a good characteristic as the films are meant to have a high surface area). The thickness is superficially controllable with concentration.

Table 5.8. Summary of mean thickness variation with position and concentration of P25/water. Dimensions in mm

Position	0.25A	0.25B	0.5A	0.5B	0.1A	0.1B
Centre	0.004331	0.002957	0.003221	0.003929	0.011813	0.010855
Left edge	0.004825	0.004915	0.004671	0.003446	0.016189	0.019424
Right edge	0.006214	0.002957	0.004693	0.005614	0.012669	0.014561

### 5.2.2. Optical Characteristics

To study the microscopic details of P25 films on glass, optical microscope pictures were obtained for two samples (for repeatability) before and after annealing. These are shown in fig 5.28 for unannealed sample (a,b), and annealed samples (c,d). The scale bars are all 100 $\mu$ m long. It should be noted that it is extremely unlikely that the regions shown before annealing were the same as those after annealing, and any specific differences were due to the fact that the two regions were different locations. It is the general patterns of differences that were observed. Both samples had similar characteristics; a cloud-like appearance with smooth regions of material separated by deep lines of about 5 $\mu$ m wide. The surface of the powder film appeared to undulate randomly. The annealed films also had all of these qualities, and no others missing to the unannealed films. It was apparent that no visible change (at least at this scale) had occurred. It should be noted that the annealing process had a dramatic effect on the mechanical ruggedness of the film; unannealed films could be easily brushed off with a gentle stroke of the finger, whilst annealed films had to be firmly rubbed to remove them. This ruggedness made the film much easier to work with; the films were less likely to be damaged or washed off when subsequent layers were applied and thus any devices based on annealed films were more likely to succeed.



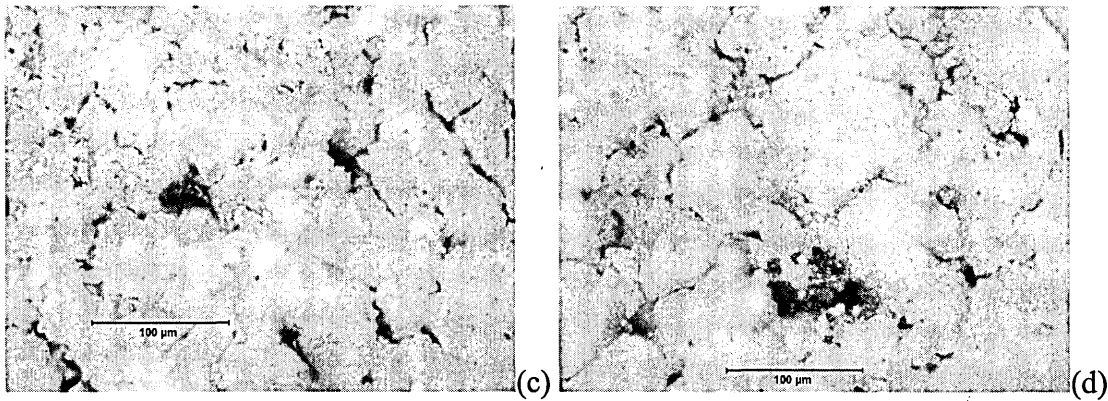


Figure 5.28. Two samples of P25 on glass before (a,b) and after (c,d) annealing.

The thickness variation of P25 films on glass was observed by taking high magnification microscope pictures of two samples (for repeatability) seen end-on. This gave the cross section of the films at different distances from the edge to the centre of the films. The microscope pictures are shown in fig 5.29 and fig 5.30 for two samples of 10mg/ml P25/water. The main difference between the two samples is that the sample in fig 5.30 shows greater homogeneity, but this could be due to the randomness of the deposition method (which is also evident in fig 5.25 to 5.27). It is clear that the films began thick (around  $1.6\mu\text{m}$ , ignoring lumps) at the edge and gets quite thin towards the centre. This could be due to the fact that a shallow trough was built on top of the substrate, and the surface tension of the water created a meniscus at the edges. Perhaps a greater amount of film settled at the point of a meniscus than in the bulk fluid. This may be a way to increase the deposition speed; if the substrate is pulled out of a bath at a shallow angle, the meniscus will slowly move down the sample creating the thicker film seen here. It is also possibly that the glass slide curvature (in the order of a few  $\mu\text{m}$ ) created a slight hill and that the fluid ran away from the hill just enough to create the dispersion of thickness.

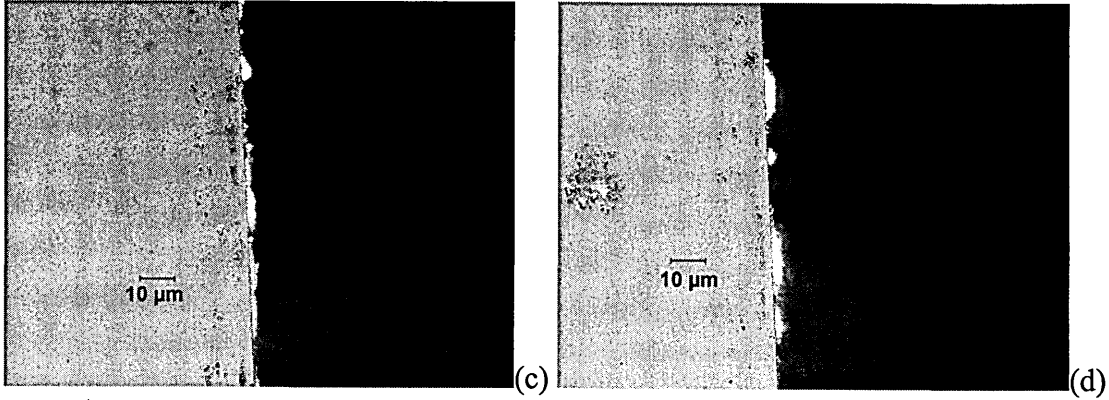
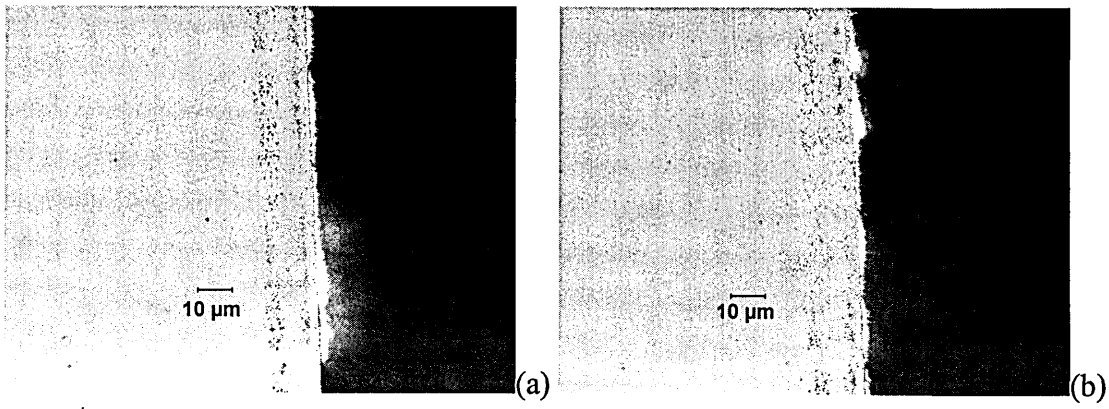


Figure 5.29. Cross-sectional optical microscope pictures of P25 on glass. Edge of film (a), short way in (b), longer way in (c), centre (d)

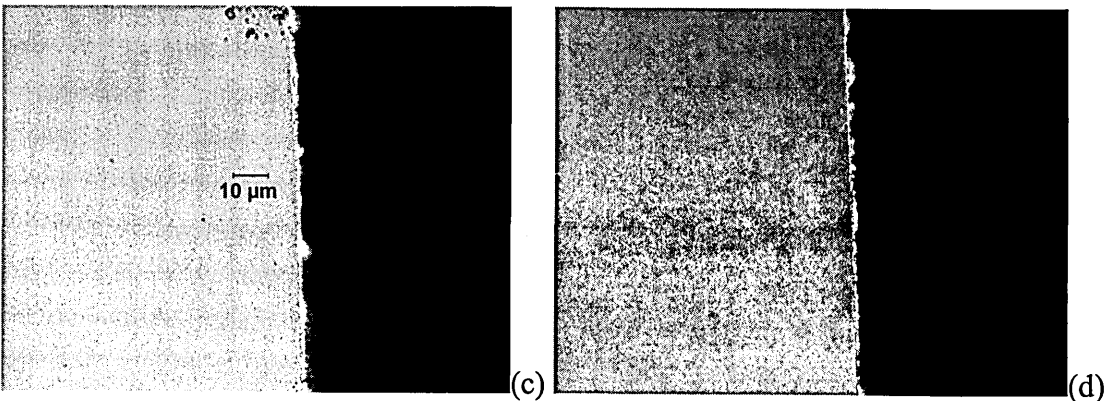
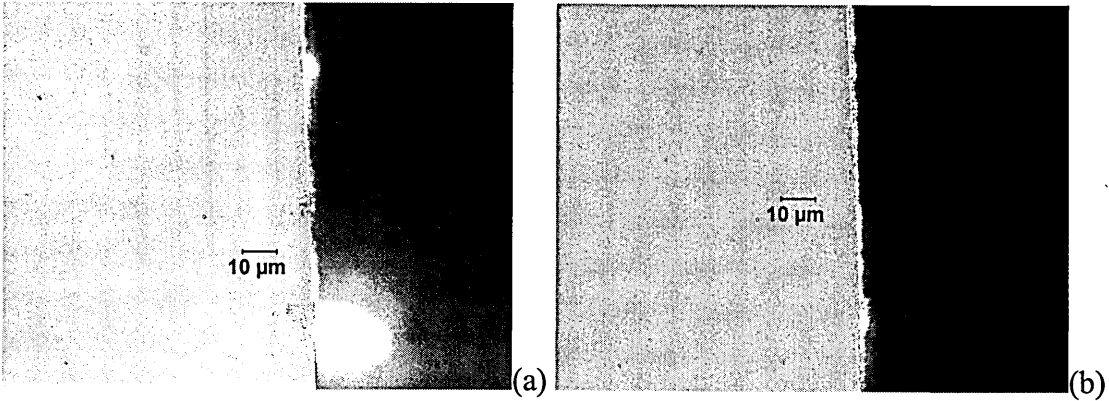


Figure 5.30. Cross-sectional optical microscope pictures of P25 on glass. Edge of film (a), short way in (b), longer way in (c), centre (d)

Whatever the reason for the variation in depth, there existed a change in thickness (ignoring the lumps) of that at the edge being approximately twice that in the middle. It is expected that the thickness of the powder will have some effect on the efficiency of the cell, and therefore the dispersion of thickness is expected to cause a dispersion of photovoltaic effect across the cells.

### 5.3. Dye Layer Optical Characteristics

It was thought that the absorption spectra of the two dyes might change slightly when applied to the  $\text{TiO}_2$ , due to some sort of shift caused by chemical bonding, so absorption spectra of dyes on glass, dyes on  $\text{TiO}_2$  on glass, and dyes on  $\text{TiO}_2$  on F:TO on glass were measured at various locations on the samples (for repeatability), and are shown in fig 5.31 for CuPc, and fig 5.32 for Rose Bengal. The spectra were normalised so that the largest peak equals 1.

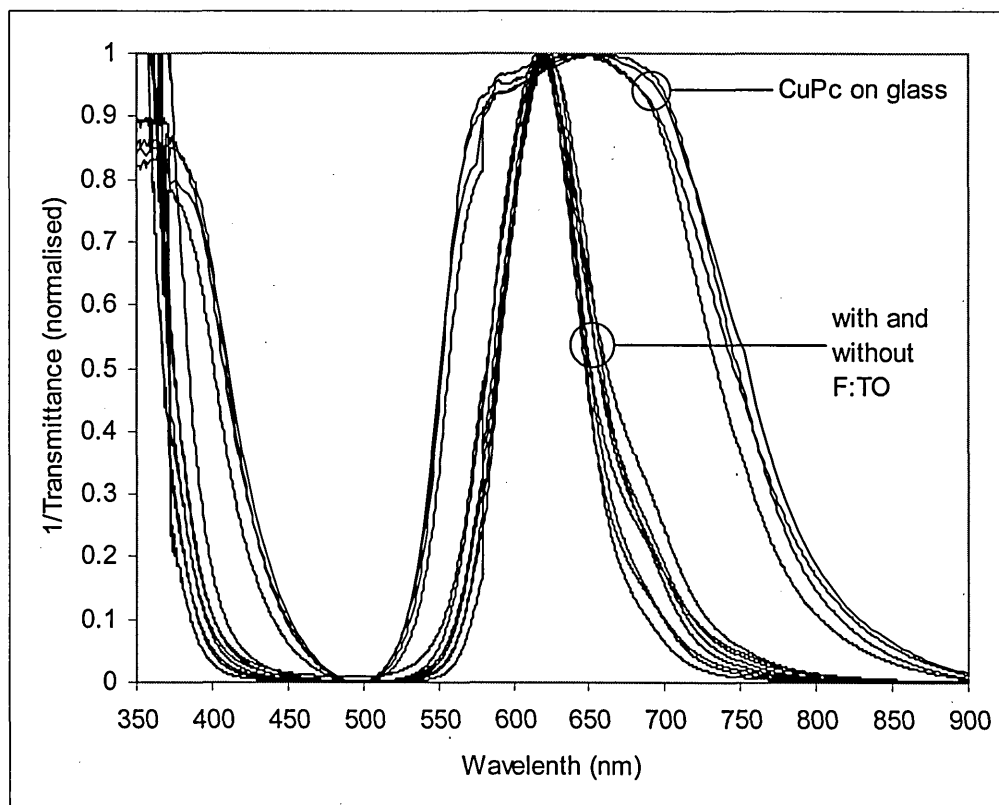


Figure 5.31. Comparison of various CuPc normalised 1/transmittance spectra

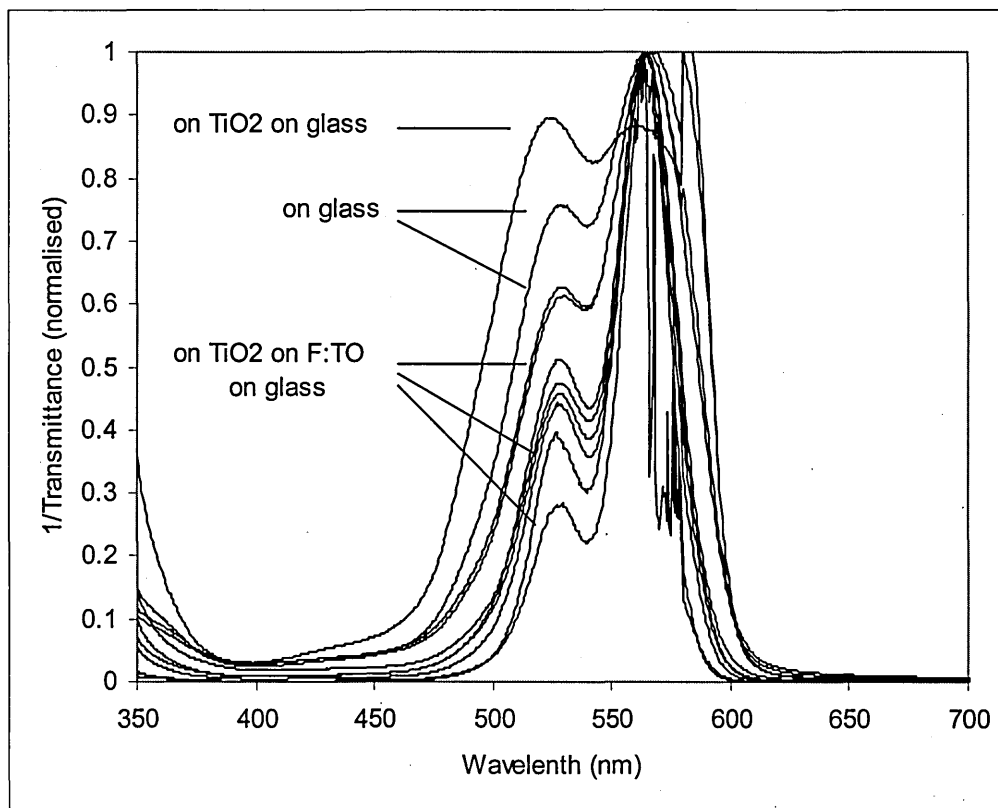


Figure 5.32. Comparison of various Rose Bengal normalised 1/transmittance spectra

The UV-Vis spectra of CuPc films on glass were somehow truncated. These made it look like a single, very broad peak at about 650nm. This result was repeated for several spectra and for two different measurement machines, so the results are real. The remaining spectra of CuPc on TiO<sub>2</sub> with and without the F:TO layer are more like the normal spectra of CuPc, but show little change between types of sample over and above the changes between different spectra of the same sample. The UV-Vis spectra of Rose Bengal films are all quite similar in terms of the main peak at about 560nm, but the secondary peak at about 530nm varies greatly depending on the substrate used (and also within each of the sets, e.g. the spectra of Rose Bengal on glass have a variety of peak heights showing some inhomogeneity in the films). The variations described suggest that the CuPc films are more homogeneous than the Rose Bengal films. The Rose Bengal film on TiO<sub>2</sub> without F:TO gives the highest secondary peak (only one spectra on TiO<sub>2</sub> without F:TO is shown as the others were too noisy), the films on plain glass

show the second highest secondary peaks, and the films on TiO<sub>2</sub> with F:TO show the lowest secondary peak. Unfortunately, the solar cells all have a layer of TiO<sub>2</sub> on an F:TO layer and will therefore suffer this loss in absorbance around 530nm. This loss would not be covered by using a tandem cell of CuPc and Rose Bengal, as the absorbance peaks do not overlap enough. These sorts of changes in the absorption spectra of dyes in different chemical environments were shown in published work (17-20), and were therefore believed to be real effects and not simply bad samples.

#### **5.4. Solar Cells Electrical Characteristics**

I(V) characteristics for several devices of each of the fifteen designs of solar cells were obtained for at least three repeated measurements (to observe changes in the spectra with time) and up to three different light levels from total darkness to full sunlight. The graphs for one device each of designs 2 to 15 are shown in fig 5.33 to fig 5.46 respectively, and the designs are shown in table 4.1 in the previous chapter. Graphs for design 1 are not shown, as the design did not work due to poor top metal contact.

Individual graphs are highlighted where they appeared to be different from others under the same conditions. Designs two and three both degraded under higher light levels as either the rectification was poorer and/or the current in forward bias was lower whereas design four did not alter much with light level or time. Design five was inconsistent in dark (first spectra) but became repeatable in full sunlight (last spectra). It is possible that this was caused by filaments of the top metal contact being burned out with current over time. Designs six, seven and nine showed slight improvement with time, but were mostly unchanged. Design eight remained consistent. Design ten to twelve showed little change over time, whereas designs thirteen to fifteen showed some change over time.

Designs two to seven all appeared to have quite good diode-like characteristics, but only nine and fifteen of the second half of the designs have a diode-like response. The other

odd-numbered designs of the second half (eleven and thirteen) appear to have a slight diode-like response when compared to the even-numbered designs of the second half. All the odd-numbered designs of the second half have a PVK layer whereas the even-numbered designs of the second half do not. This suggests that the PVK layer greatly improves the quality of the designs. Designs twelve and thirteen (3 layers of CuPc) were not as good as designs eight and nine (1 layer of CuPc). This was unexpected, as it was believed that a thicker layer of dye should give a better coverage and higher light absorption and thus a better diode and photo response. The diode fitting and photo tests show a slightly higher series resistance and worse photo response for designs eleven and twelve. The parallel resistance for designs eleven and twelve (and also eight) were two orders of magnitude less than for design nine. The low parallel resistance was believed to be the reason for the poor results for these designs. Low parallel resistance can be caused by microfilaments through the device created by the platinum filling micropores in the structure. These filaments would manifest as a low resistance in parallel with the device effectively turning the diode into a resistor with some or no diode effect observed. Poorer quality devices (in terms of diode-like response) tended to have higher ideality factors. Designs eight to fifteen tend to be comprised of thinner devices whether by fewer layers of P25 (1 layer instead of three) or by the thinner dye layer (bath soaked instead of flood soaked) and this increased the likelihood of filaments reaching the bottom contact (or at least the sputtered  $\text{TiO}_2$  layer). There is none of the expected negative shift in the current axis with increasing light levels. This is due to the fact that the photovoltage rose sharply when the device is first exposed to light, and then dropped away to nothing in a few tens of seconds. Designs eight to fifteen only had graphs obtained in the dark, as there was no light response. The I(V) graphs were obtained in the order of two minutes per device, and with each device being illuminated at the same time, the photo-response was nullified before it can be seen in the I(V) graph. There is

normally a general relaxing of the devices when graphs are obtained one immediately after the other, which stops after several sweeps. The low current (in forward bias) but relatively good diode response of design fifteen is due to a low (relative to other devices) ideality factor and a high reverse saturation current. The ideality factors of all devices fell well outside the normally stated range of about 1 to 2. This is attributed to poor diode quality caused by e.g. filaments and poor electrical contact with the dye. Some devices from designs six and seven had reverse saturation current in the range of nanoamps, which is similar to those in some published work (21). Designs eight and fourteen have reverse saturation currents six orders of magnitude larger than published (21) showing poor diode response. Series resistance varied from about  $15\Omega$  to about  $500\Omega$  (lowest for design 6 which had a flat structure and therefore the best top contact). This is in a similar range to that published (21). Parallel resistance varies from about  $100\Omega$  (such as for designs eight and fourteen) up to about  $1M\Omega$ , which is a larger range than for some published work (21), but the maximum is much greater.

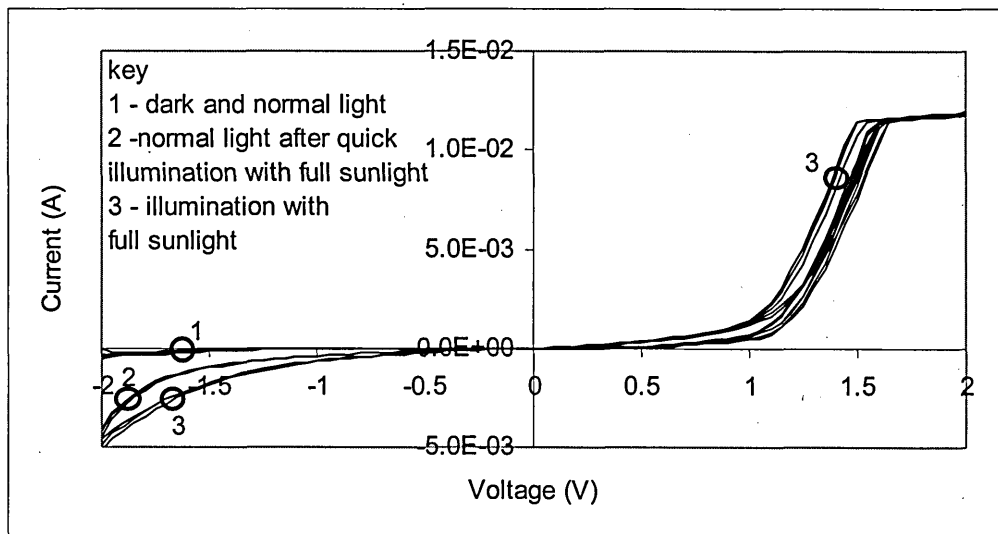


Figure 5.33. I(V) characteristics of solar cell design two.

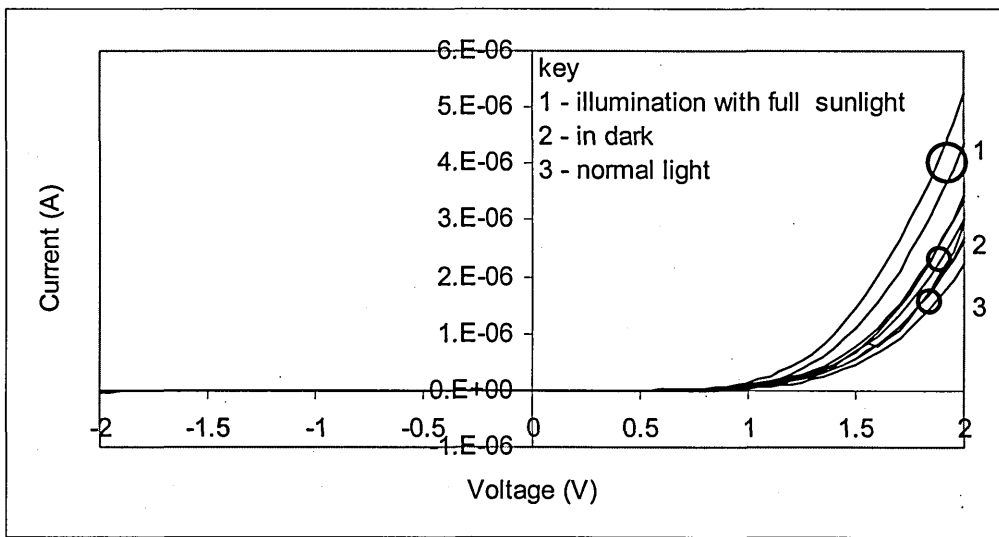


Figure 5.34. I(V) characteristics of solar cell design three.

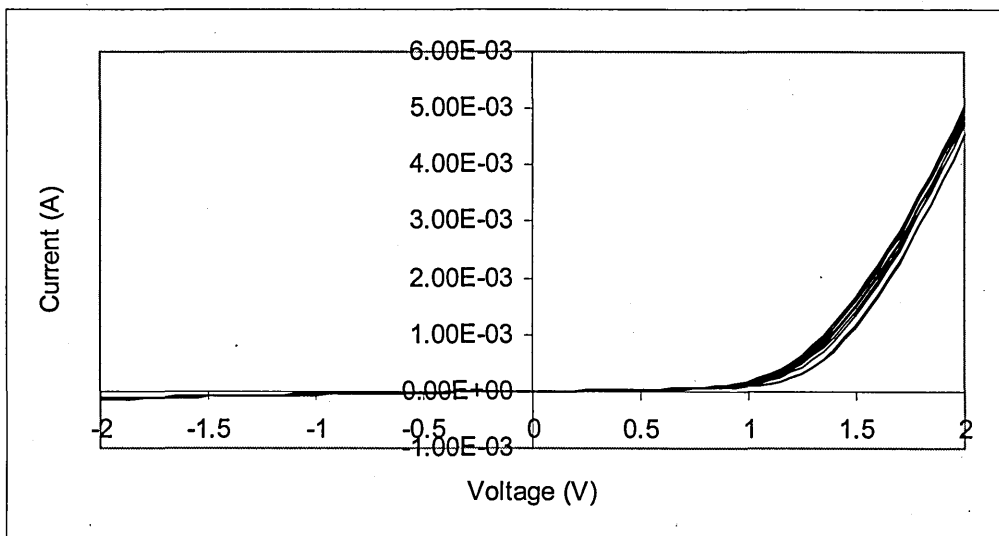


Figure 5.35. I(V) characteristics of solar cell design four.

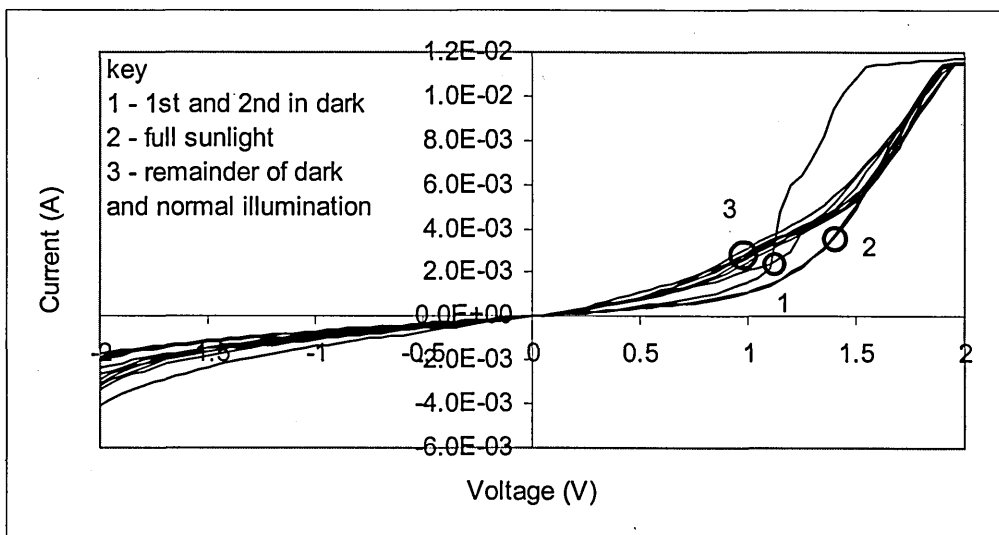


Figure 5.36. I(V) characteristics of solar cell design five.

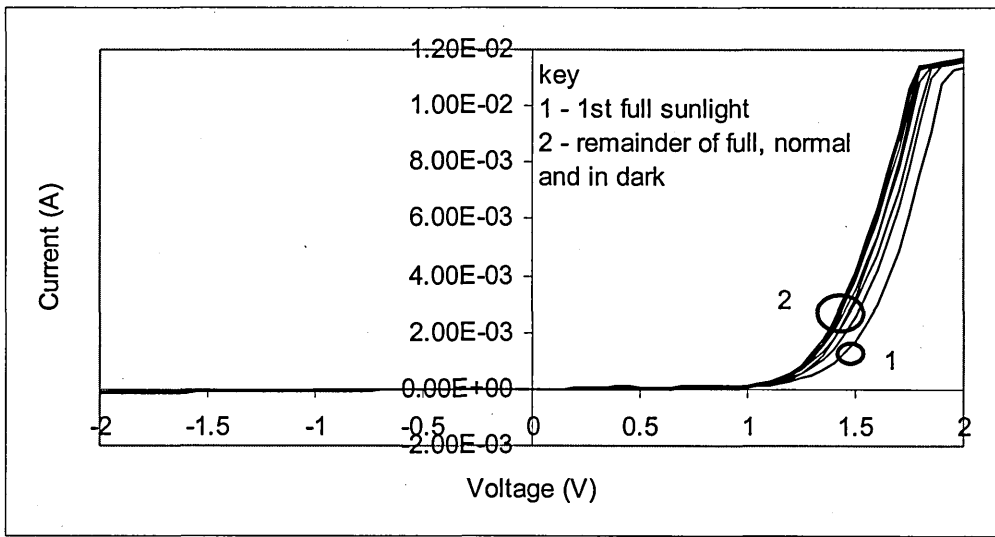


Figure 5.37. I(V) characteristics of solar cell design six.

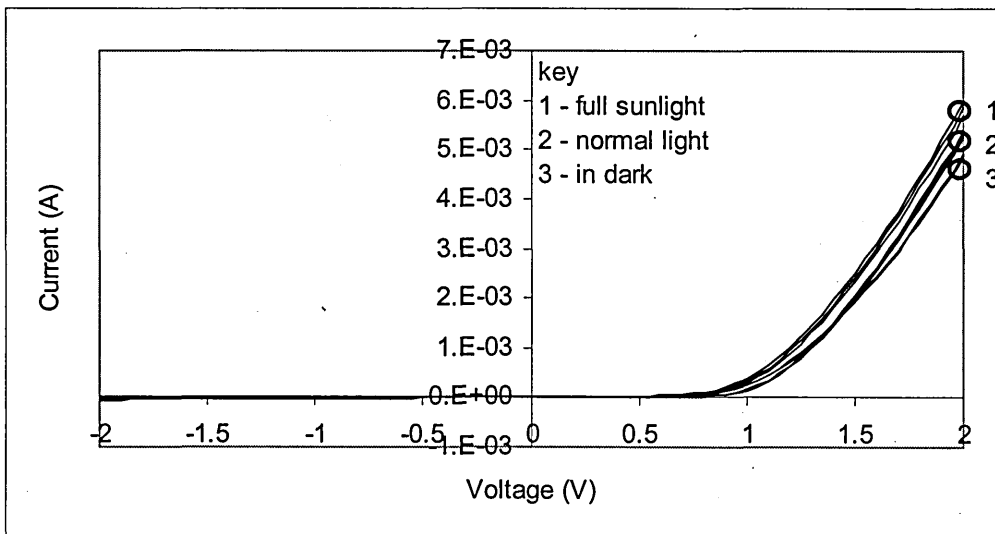


Figure 5.38. I(V) characteristics of solar cell design seven.

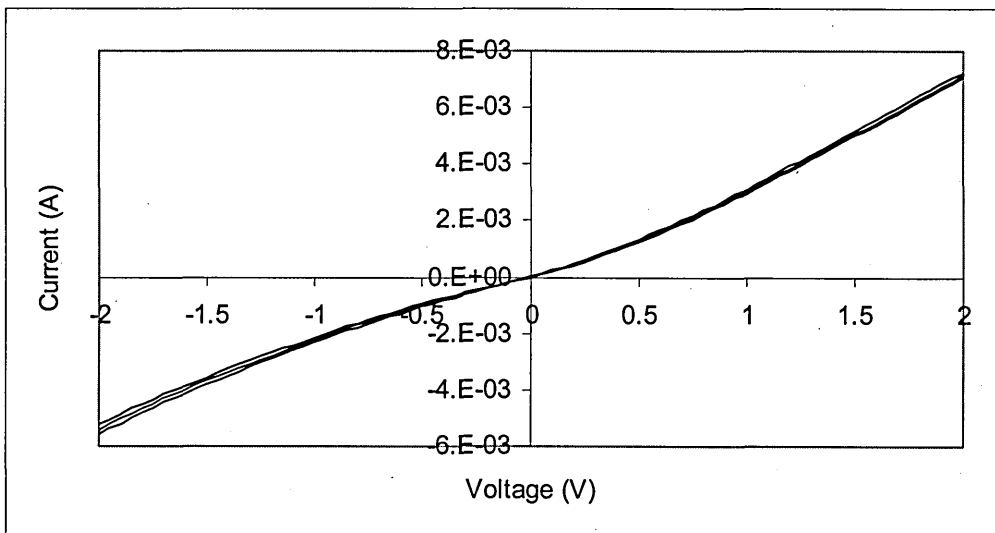


Figure 5.39. I(V) characteristics of solar cell design eight (all in dark).

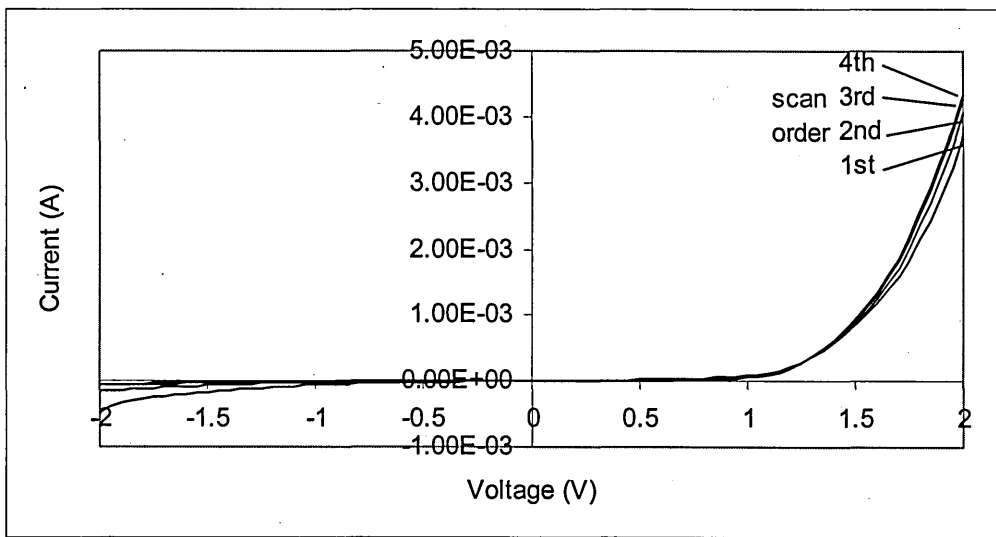


Figure 5.40. I(V) characteristics of solar cell design nine (all in dark).

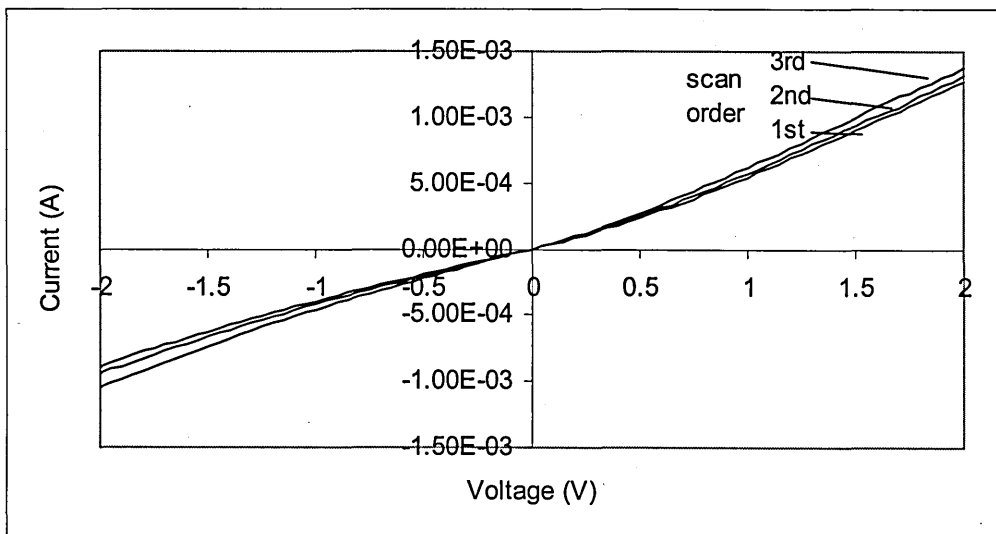


Figure 5.41. I(V) characteristics of solar cell design ten (all in dark).

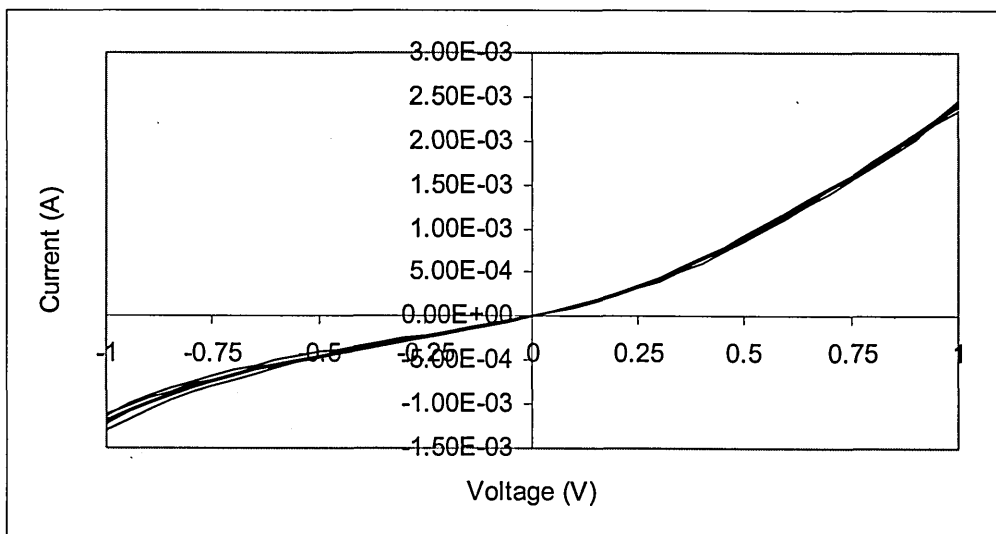


Figure 5.42. I(V) characteristics of solar cell design eleven (all in dark).

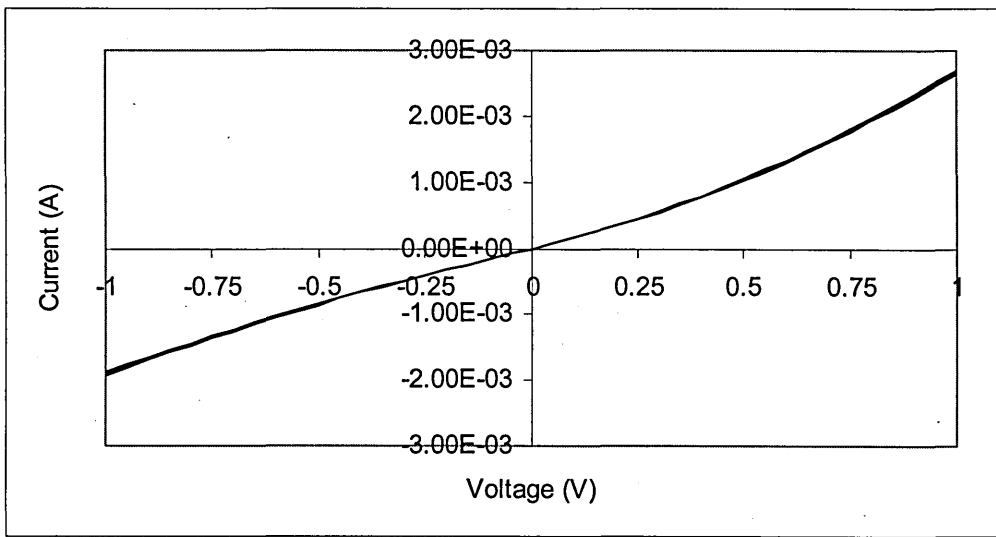


Figure 5.43. I(V) characteristics of solar cell design twelve (all in dark).

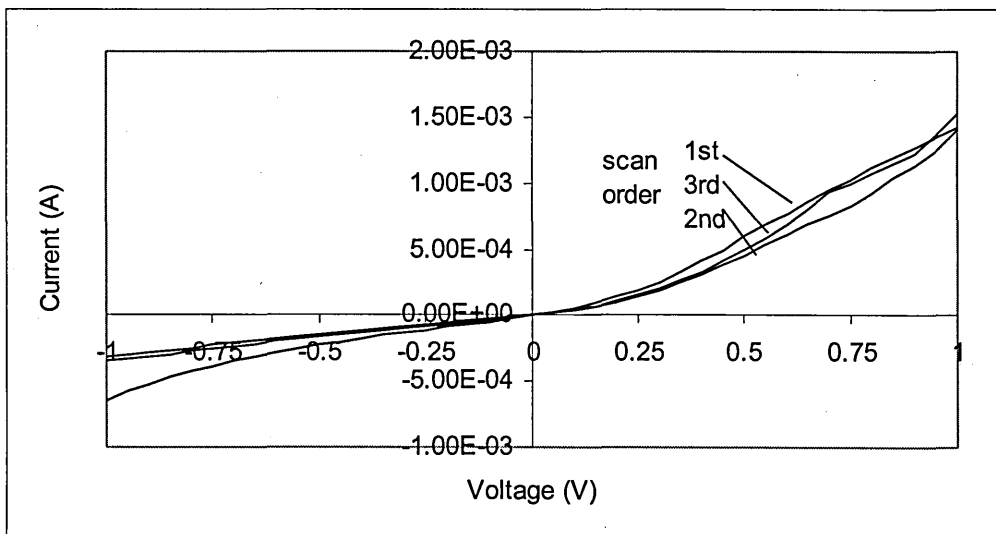


Figure 5.44. I(V) characteristics of solar cell design thirteen (all in dark).

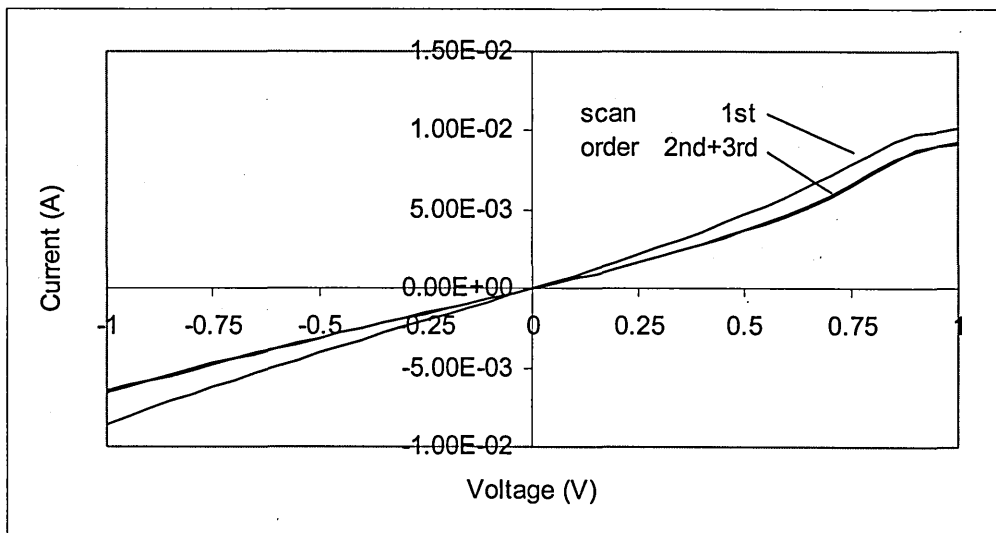


Figure 5.45. I(V) characteristics of solar cell design fourteen (all in dark).

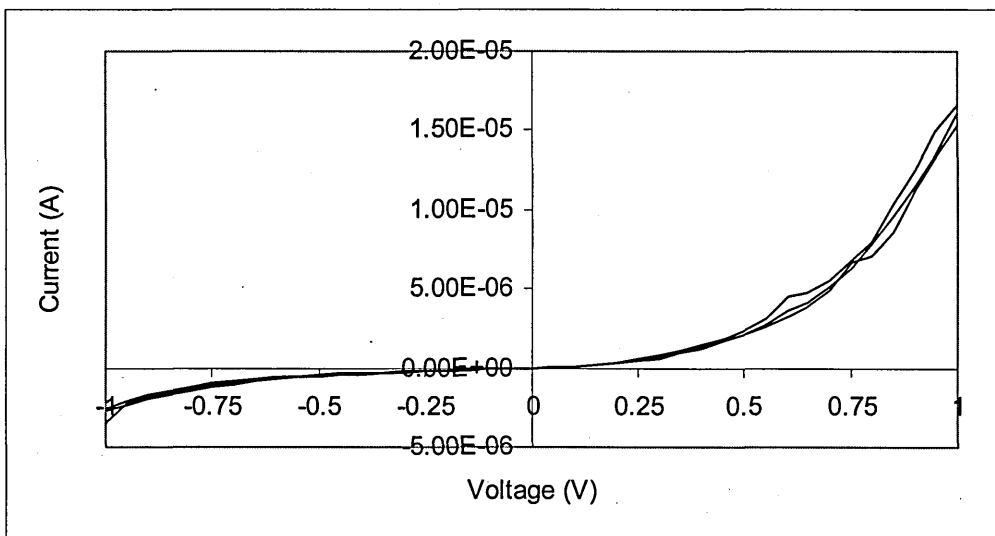


Figure 5.46. I(V) characteristics of solar cell design fifteen (all in dark).

Every graph was fitted (where possible) to a single diode equation (described in chapter 3 but repeated here for ease of reading);

$$V = \left( \frac{nkT}{q} \right) \times \ln \left[ \frac{(I + I_{ph} + I_s)}{I_s} \right] + \bar{R}_s I \quad (5.2)$$

$I_{ph}$  was not fitted by equation 5.2, but was obtained as the current at zero voltage bias on the I(V) spectra for designs four to seven, and since this  $I_{ph}$  was not consistent with that measured by a multimeter, it was not obtained by graphically for the rest of the designs. The results of the fitting of the above I(V) graphs are shown in table 5.9 for design 4 to 9 and table 5.10 for designs 10 to 15.

Table 5.9. Diode model fitted parameters for designs 4 to 9.

design	illumination	test run	Is (A)	n	Iph (A)	Rs (ohm)	Rp (ohm)	
4	dark	1	1.9769E-07	6.2585	2.3980E-08	8.2710E+01	1.5144E+04	
		2	2.3000E-07	6.0000	2.8554E-08	9.5000E+01	1.5837E+04	
		3	2.8000E-07	6.0000	3.5026E-08	1.0000E+02	1.5002E+04	
		4	1.8705E-06	7.7967	3.0819E-08	8.1909E+01	1.6700E+04	
	normal	1	1.8866E-07	6.1895	1.2924E-08	8.5301E+01	1.7155E+04	
		2	8.1913E-07	7.1546	1.0553E-08	8.4302E+01	1.7079E+04	
		3	1.4081E-06	7.5844	9.6448E-09	8.3613E+01	1.6756E+04	
	full sunlight	1	5.4091E-07	6.8600	3.8922E-08	8.2318E+01	1.6328E+04	
		2	2.5482E-07	6.0912	3.7804E-08	9.2433E+01	1.6555E+04	
3		3.0322E-07	6.0242	4.0812E-08	9.6945E+01	1.5718E+04		
5	dark	1	2.0000E-07	4.0000	1.8058E-08	4.0000E+01	1.2458E+03	
		2	8.7097E-05	12.0000	2.6606E-07	4.0000E+01	5.8361E+02	
		3	8.7097E-05	11.0000	2.0836E-07	4.0000E+01	7.6124E+02	
		4	8.7097E-05	11.0000	3.1928E-07	4.0000E+01	8.3910E+02	
		5	8.7097E-05	11.0000	5.2752E-07	4.0000E+01	8.3723E+02	
	normal	6	8.7097E-05	11.0000	5.2433E-07	4.0000E+01	9.5509E+02	
		1	8.7097E-05	11.0000	4.5503E-07	4.0000E+01	8.2566E+02	
		2	8.7097E-05	11.0000	9.3044E-08	4.0000E+01	9.0575E+02	
		3	8.7097E-05	11.0000	3.0333E-07	4.0000E+01	9.6168E+02	
		3	8.7097E-05	11.0000	3.0333E-07	4.0000E+01	9.6168E+02	
	full sunlight	1	5.7097E-05	11.0000	5.3928E-07	4.0000E+01	1.1433E+03	
		2	5.7097E-05	11.0000	4.9843E-07	4.0000E+01	1.2140E+03	
		3	5.7097E-05	11.0000	5.8150E-07	4.0000E+01	1.2042E+03	
	6	dark	1	3.2212E-09	3.9940	5.9991E-08	2.2250E+01	1.8253E+04
			2	8.1552E-09	4.1682	5.3344E-08	2.2867E+01	1.8249E+04
3			1.0943E-08	4.2336	4.7802E-08	2.2916E+01	1.8163E+04	
normal		7	7.1077E-09	4.1132	2.5285E-08	2.3524E+01	1.6388E+04	
		1	4.7281E-09	4.0113	6.7149E-08	2.2824E+01	1.6384E+04	
		2	1.3392E-07	5.7329	1.4118E-07	1.6053E+01	1.5271E+04	
		3	5.8570E-08	4.9851	6.6613E-08	1.9447E+01	1.6094E+04	
full sunlight		1	7.0773E-08	5.6451	4.2368E-07	1.5432E+01	1.3525E+04	
		2	1.1816E-07	5.4804	1.9949E-07	2.0306E+01	1.4984E+04	
		3	1.2307E-07	5.3935	1.6092E-07	2.0177E+01	1.4257E+04	
7		dark	1	3.1699E-06	7.2861	7.9600E-09	9.7093E+01	5.3660E+04
			2	2.6202E-06	7.1426	2.7600E-09	9.8928E+01	1.9919E+05
	3		8.7371E-07	6.1394	4.2100E-09	1.0695E+02	2.1138E+05	
	normal	1	5.0212E-09	3.7634	5.3000E-09	1.2110E+02	2.9463E+05	
		2	2.6080E-08	4.3066	2.3100E-09	1.2166E+02	4.6499E+05	
		3	1.0379E-08	3.9984	2.4900E-09	1.2357E+02	6.0638E+05	
	full sunlight	1	3.5548E-07	5.7000	1.3700E-07	1.2300E+02	3.4555E+05	
		2	3.5548E-07	5.7000	1.6200E-07	1.2300E+02	7.3793E+05	
		3	3.5548E-07	5.7000	1.5600E-07	1.2300E+02	7.7990E+05	
8	dark	1	7.4824E-03	79.6834	0	8.1641E+01	3.6972E+02	
		2	6.8742E-03	70.1825	0	9.8059E+01	3.8262E+02	
		3	6.7817E-03	69.8227	0	1.0012E+02	3.9670E+02	
9	dark	1	7.5260E-07	8.0000	0	7.0000E+01	1.0953E+04	
		2	1.2171E-06	8.5845	0	5.0510E+01	3.0632E+04	
		3	8.9875E-07	8.1346	0	5.2000E+01	4.6348E+04	
		4	5.3875E-07	7.5000	0	6.0000E+01	5.7869E+04	

Table 5.10. Diode model fitted parameters for designs 10 to 15.

design	illumination	test run	Is (A)	n	Iph (A)	Rs (ohm)	Rp (ohm)
10	dark	1	6.9260E-04	48.0000	0	3.5000E+02	1.9423E+03
		2	6.9260E-04	48.0000	0	4.5000E+02	2.1563E+03
		3	6.9260E-04	48.0000	0	5.0000E+02	2.2974E+03
11	dark	1	7.4824E-04	20.0000	0	1.0000E+02	8.6917E+02
		2	1.1461E-03	26.2189	0	1.0093E+02	9.2519E+02
		3	1.1461E-03	26.2189	0	1.0093E+02	9.5361E+02
		4	7.4614E-04	20.0000	0	1.0093E+02	9.3864E+02
		5	6.4614E-04	19.0000	0	1.0093E+02	1.0166E+03
		6	3.8725E-04	13.1095	0	1.3255E+02	9.7971E+02
12	dark	1	6.9260E-04	14.2963	0	1.5608E+02	5.2533E+02
		2	6.9260E-04	14.2963	0	1.5608E+02	5.3273E+02
		3	6.9260E-04	14.2963	0	1.5608E+02	5.3697E+02
13	dark	1	1.5026E-04	9.4000	0	2.0000E+02	1.7664E+03
		2	9.5260E-05	9.5000	0	1.6000E+02	3.1877E+03
		3	9.5260E-05	8.9000	0	1.6000E+02	2.9164E+03
14	dark	1	2.8955E-03	10.0000	0	5.3000E+01	1.1740E+02
		2	2.4955E-03	13.0000	0	5.3000E+01	1.5561E+02
		3	2.4955E-03	12.0000	0	5.3000E+01	1.5247E+02
15	dark	1	5.2213E-07	11.0000	0	5.0000E+01	5.8786E+05
		2	4.8213E-07	11.0000	0	5.0000E+01	6.3442E+05
		3	3.7213E-07	10.0000	0	5.0000E+01	7.1081E+05

Table 5.11. Voc and Isc values for designs 4 to 7.

Design	Cell	Device	Voc (mV)	Isc (uA)	Design	Cell	Device	Voc (mV)	Isc (uA)
4	1	1	0.0	0.0	6	1	1	0.0	0.0
4	1	2	0.0	0.0	6	1	2	0.0	0.0
4	1	3	1.5	0.0	6	1	3	0.4	0.0
4	2	1	0.1	0.0	6	2	1	215.0	0.1
4	2	2	0.3	0.0	6	2	2	0.0	0.0
4	2	3	0.0	0.0	6	2	3	0.0	0.0
4	3	1	108.0	0.6	6	3	1	7.4	0.1
4	3	2	0.1	0.0	6	3	2	9.2	0.1
4	3	3	0.1	0.0	6	3	3	23.9	0.1
4	4	1	0.6	0.0	6	4	1	2.1	0.1
4	4	2	0.0	0.0	6	4	2	1.1	0.0
4	4	3	2.5	0.0	6	4	3	0.8	0.1
5	1	1	0.0	0.0	7	1	1	400.0	0.7
5	1	2	0.0	0.0	7	1	2	23.0	0.2
5	2	1	0.1	0.0	7	1	3	430.0	0.5
5	2	2	0.0	0.0	7	2	1	509.0	1.0
5	2	3	0.0	0.0	7	2	2	125.0	0.2
5	3	1	0.0	0.0	7	3	1	4.0	0.0
5	3	2	0.0	0.0	7	3	2	65.0	0.0
5	3	3	0.0	0.0	7	3	3	4.0	0.0
5	4	1	0.0	0.0	7	4	1	400.0	4.3
5	4	2	0.0	0.0	7	4	2	260.0	3.4
					7	4	3	170.0	0.0

Table 5.12. Voc and Isc values for designs 8 to 15.

Design	Cell	Device	Voc (mV)	Isc (uA)	Design	Cell	Device	Voc (mV)	Isc (uA)
8	1	1	0.0	0.0	12	1	1	0.1	0.0
8	1	2	0.1	0.1	12	1	2	0.0	0.0
8	1	3	0.0	0.0	12	1	3	0.1	0.0
8	2	1	0.1	0.0	12	2	1	0.8	0.0
8	2	2	0.0	0.0	12	2	2	0.2	0.0
9	1	1	13.5	0.2	12	2	3	0.2	0.0
9	1	2	1.1	0.3	13	1	1	12.0	0.8
9	1	3	0.3	0.2	13	1	2	3.0	1.2
9	2	1	51.0	0.7	13	1	3	30.0	1.6
9	2	2	21.0	0.7	13	2	1	12.0	0.7
9	2	3	0.1	0.0	13	2	2	5.6	1.0
10	1	1	0.1	0.1	13	2	3	0.1	0.1
10	1	2	0.0	0.0	14	1	1	0.0	0.0
10	2	1	0.0	0.0	14	1	2	0.0	0.0
10	2	2	0.0	0.0	14	1	3	0.0	0.0
11	1	1	0.1	0.1	14	2	1	0.0	0.0
11	1	2	0.1	0.1	14	2	2	0.0	0.0
11	1	3	1.0	0.6	14	2	3	0.0	0.0
11	2	1	0.1	0.1	15	1	1	0.1	0.1
11	2	2	0.0	0.1	15	1	2	12.0	0.4
11	2	3	4.7	1.2	15	1	3	31.0	0.5
					15	2	1	34.0	0.5
					15	2	2	128.0	0.5
					15	2	3	4.5	0.5

Every device was tested under full sunlight for their photovoltaic properties in terms of open circuit voltage ( $V_{oc}$ ) and short circuit current ( $I_{sc}$ ). The results of these photovoltaic tests are shown in table 5.11 and table 5.12 for designs 4 to 7 and 8 to 15 respectively.

The table shows either two or four cells per design and two or three devices per cell.

Designs one, two and, three had relatively thick layers of P25 and gave no photoresponse. Designs four and five had thinner layers and gave a small but measurable photoresponse. Designs six and seven had either a still thinner P25 layer or no layer at all and gave good photoresponse. These two designs also had the best diode characteristics, but design seven had both higher series and parallel resistances due to the extra powder layer (higher series resistance due to rough structure, and higher parallel resistance due to a thicker structure). Designs eight to fifteen kept the same P25 thickness as design seven but reduced the dye thickness by different application in a bid to reduce the series resistance. The photoresponse suffered severely. The odd-numbered

designs all had a layer of PVK below the top contacts and all gave better response than the even-numbered designs, which lacked the PVK layer. The designs with a single dye layer worked better if the dye was CuPc. The designs with three dye layers worked better if the dye was Rose Bengal. This may be due to different dye conductivities and opposing effects of increase light absorption and increased series resistance with increased dye thickness.

The five devices that gave the best photovoltaic response were tested for their response to a varying load. The I(V) and Power(V) graphs are shown in fig 5.47 to fig 5.51 for designs 7 to 15 respectively (filled squares represent power, empty squares represent current). The photovoltage was measured at different resistances from kilo ohms to mega ohms, and the resultant current and power calculated. The current was obtained by calculation as the values were near the bottom limit of the measurement equipment, and therefore were subject to large errors. The calculated fill factors and efficiency values are shown in table 5.13. The device area was 9mm by 0.5mm and the light input was  $1000\text{W/m}^2$ . The results for designs eleven and thirteen were affected significantly by noise, possibly due to the fast decay/slow recovery of the photocurrent. As the result is much better for design nine, which has a much smaller photovoltage, the noise for designs eleven and thirteen is unlikely to be due to low signal to noise ratio. The fill factor results general show a decrease of current with increasing voltage (as should have been seen reflected in the bottom right quadrant of the I(V) spectra of illuminated cells) and a peak power somewhere in the middle of the voltage scale corresponding to the ideal load resistance for the cell and the point from which can be calculated the fill factor of the device. The fill factor results were not fitted to some equation, instead, the data point giving maximum power was chosen and the fill factor and efficiency calculated from this point.

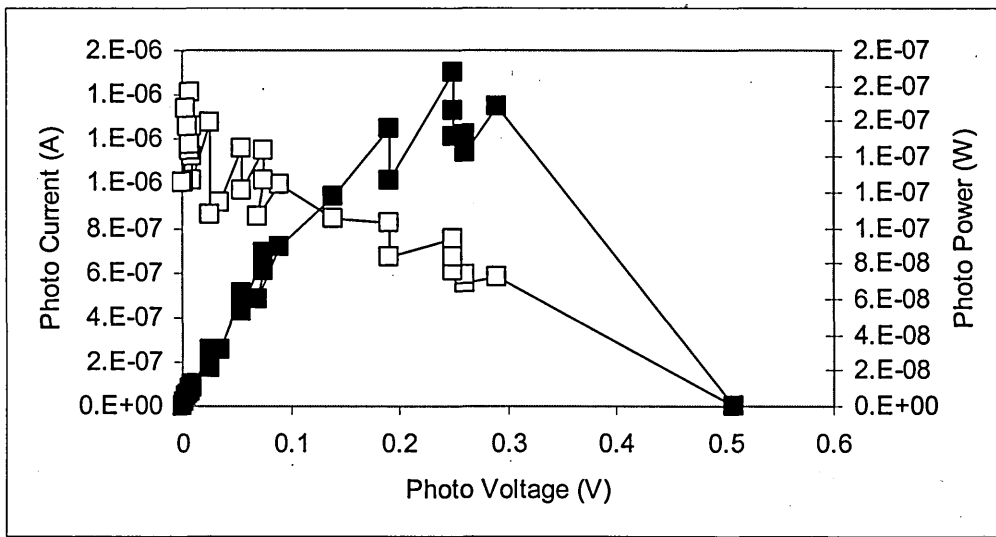


Figure 5.47. I(V) and P(V) graph of design 7 under load

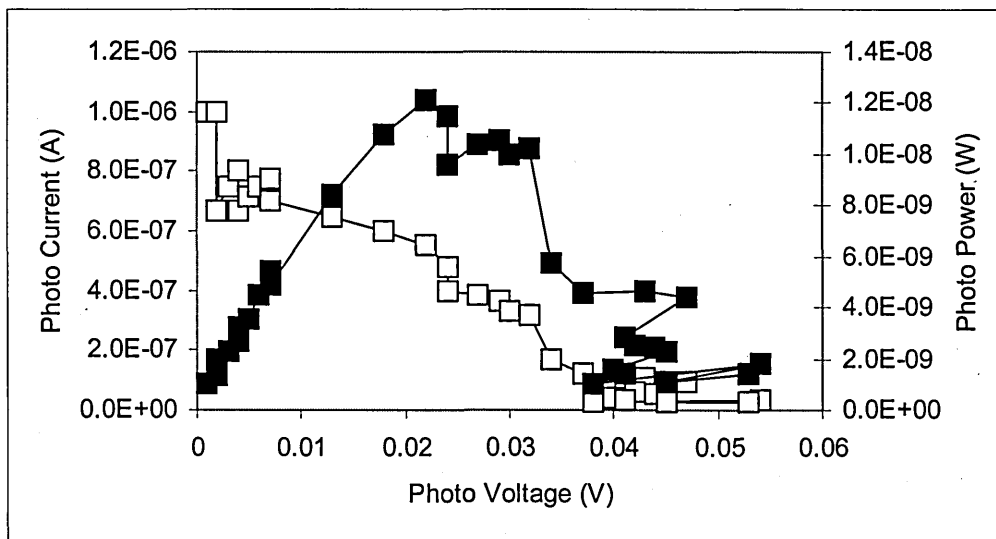


Figure 5.48. I(V) and P(V) graph of design 9 under load

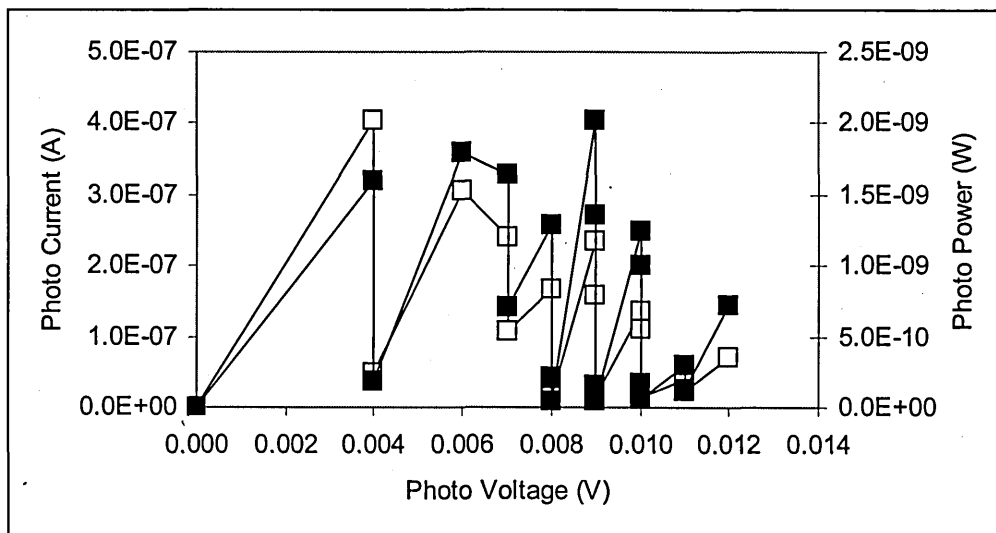


Figure 5.49. I(V) and P(V) graph of design 11 under load

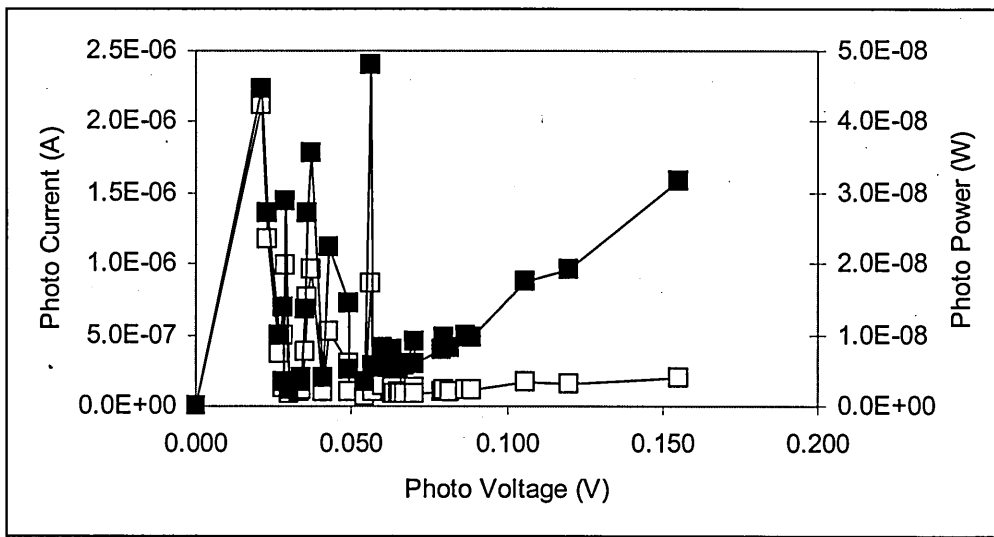


Figure 5.50. I(V) and P(V) graph of design 13 under load

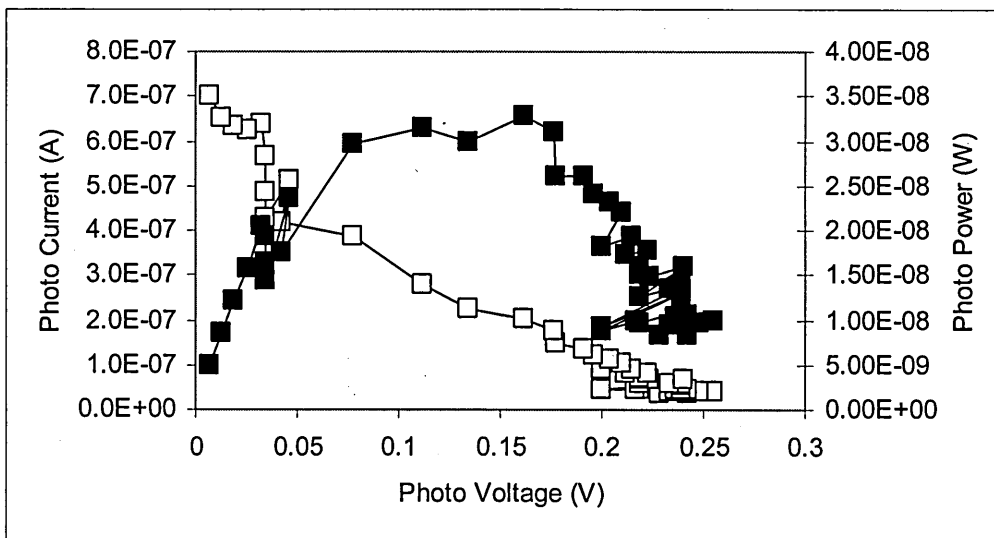


Figure 5.51. I(V) and P(V) graph of design 15 under load

Table 5.13. Summary of fill factor and efficiency of five designs.

Design	Fill factor(%)	Efficiency (%)
7	35.5248	4.1667E-03
9	33.8936	2.6889E-04
11	35.9043	4.5000E-05
13	45.1613	9.9556E-04
15	29.4215	7.2900E-04

The efficiencies obtained in this research are within the range of values given in published work, but still three orders of magnitude behind the best of the wet dye sensitised cells (22). The fill factors obtained in this research are also within the range of values of some published work (23), but again some way behind the best of the wet cells.

## 5.5. Top Cell Contact

The top contact is the last layer to be deposited and consists of a thin metal film around 100 nm thick into which flows the electrons from the load. The top contact must connect well with the layer onto which it is deposited (either dye, or PVK), or else the efficiency will be reduced as a result of e.g. increased resistance.

### 5.5.1. Optical Characteristics

Optical microscope pictures of the bridge test devices are shown in fig 5.52 to fig 5.63 for bridge designs 1 to 12 respectively. The magnification is represented by scale bar of 100 $\mu$ m (a), and 50 $\mu$ m (b). (a) shows the finger contact as a broad, brighter, vertical stripe. (b) shows the left edge of the finger contact and the beginning of the underlying films. All of (a) have similar characteristics; a general appearance of tree bark with the occasional ripple or wave passing through. There are very few smooth patches of any great size (they would show up as a shiny patch in the otherwise rough film) which means that even with the greatest number of layers applied to the P25 film, the surface is still incredibly rough and caused the top metal contact to be effectively spread over a very large area. With the volume of metal remaining constant at  $9 \times 10^{-13} \text{ m}^3$ , the effective thickness is much reduced and the effective length of the contact is much increased (another reason as to the high series resistance caused by the contact). The ripples observed are due to ripples in the underlying films (most likely in the P25 film as this is the thickest layer by far). All of (b) have similar characteristics; they all appear to be comprised of a continent and several islands of metal in a sea of dye covered P25. Quite why there are islands of metal that appear to be isolated from the rest is unknown, as the metal should be deposited across the entire area exposed by the finger mask regardless of what the metal comes to rest upon. It may be the case that the metal actually *is* applied onto the areas between the islands and it is just that the metal is spread so thin

that it is translucent (10nm of Platinum would look translucent), and the colour of the dye is shining through. As with all of (a), the high roughness of the P25 films is still apparent and it did not appear that the extra layers of PVK applied to the P25 had made any visible difference to the roughness. Fig 5.64 shows two finger contacts applied to a bare glass slide. It is clear that the finger in (a) had not been applied well and had come away from the glass slide in little ripples and bulges. If this finger were applied to a cell, the efficiency would suffer, as the area under each ripple would be out of contact with the metal and photogenerated electrons would have to travel along the massive resistance of the P25 film in a planar direction. Effectively, the area under each ripple would not contribute to the photocurrent.

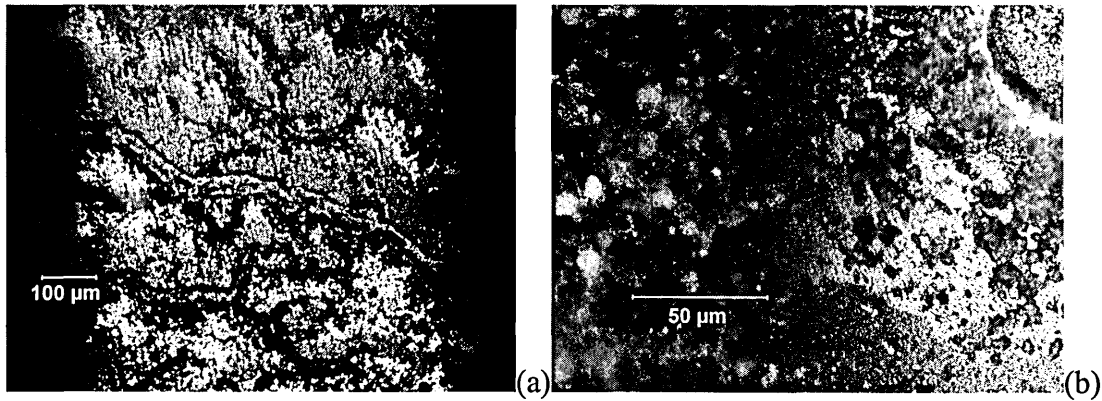


Figure 5.52. Optical microscope pictures of bridge design 1 at two scales

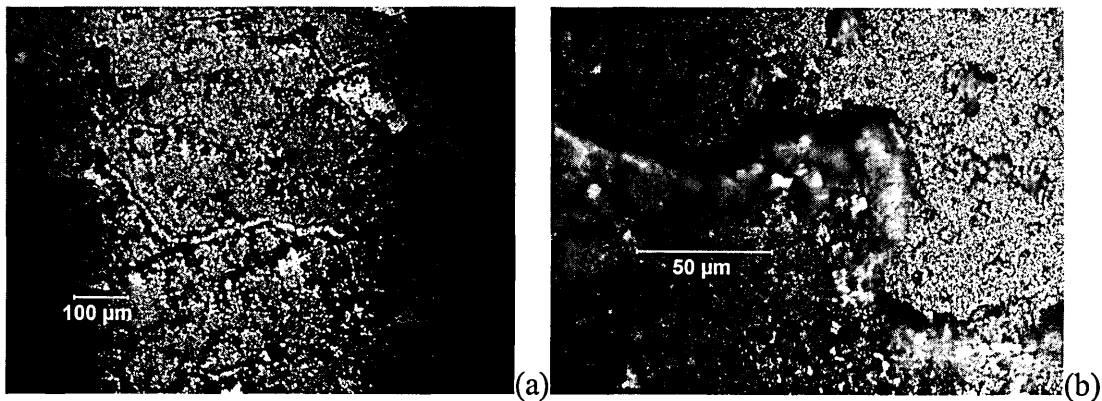
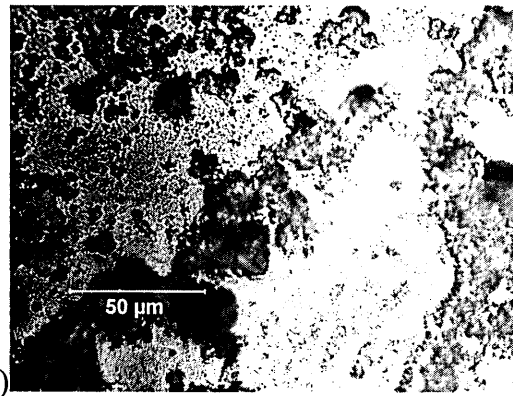
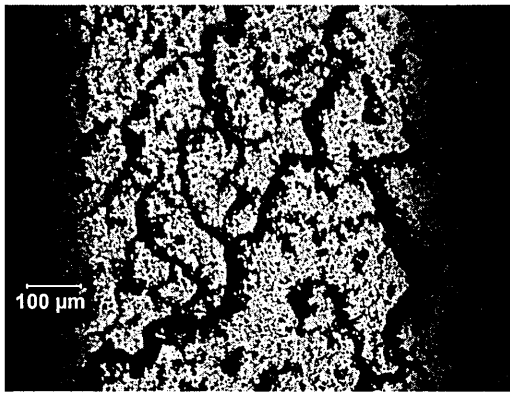


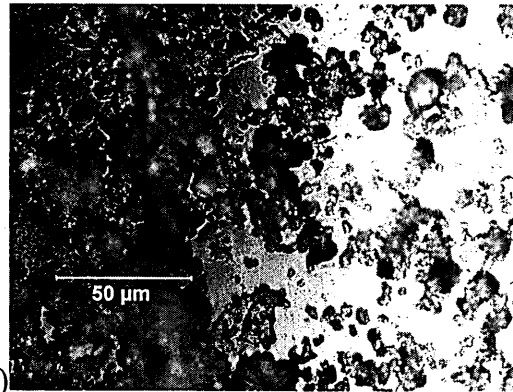
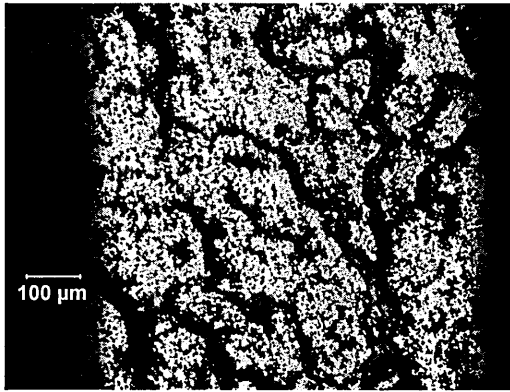
Figure 5.53. Optical microscope pictures of bridge design 2 at two scales



(a)

(b)

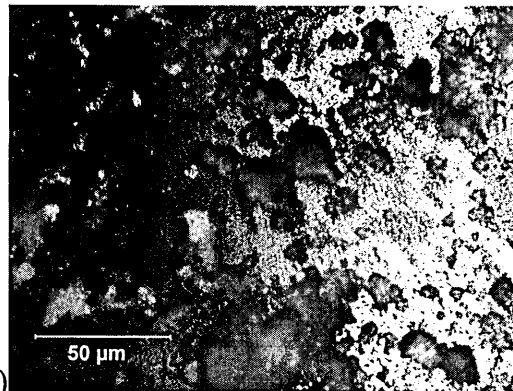
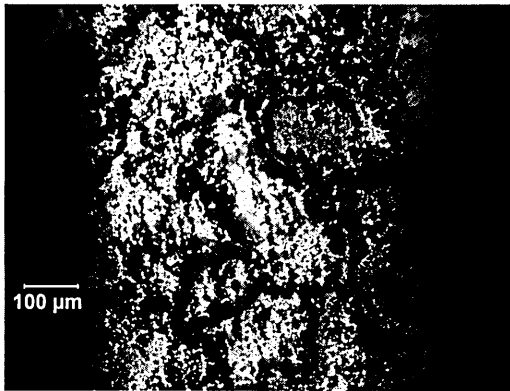
Figure 5.54. Optical microscope pictures of bridge design 3 at two scales



(a)

(b)

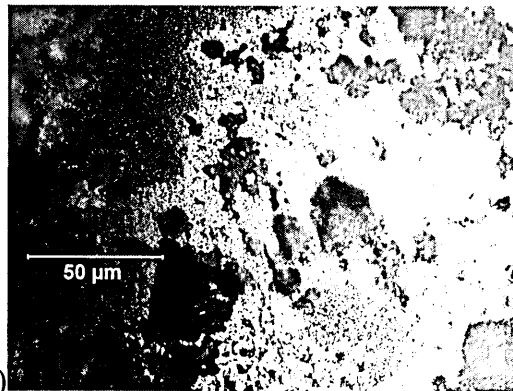
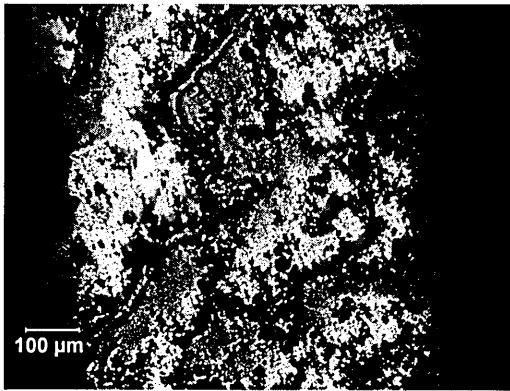
Figure 5.55. Optical microscope pictures of bridge design 4 at two scales



(a)

(b)

Figure 5.56. Optical microscope pictures of bridge design 5 at two scales



(a)

(b)

Figure 5.57. Optical microscope pictures of bridge design 6 at two scales

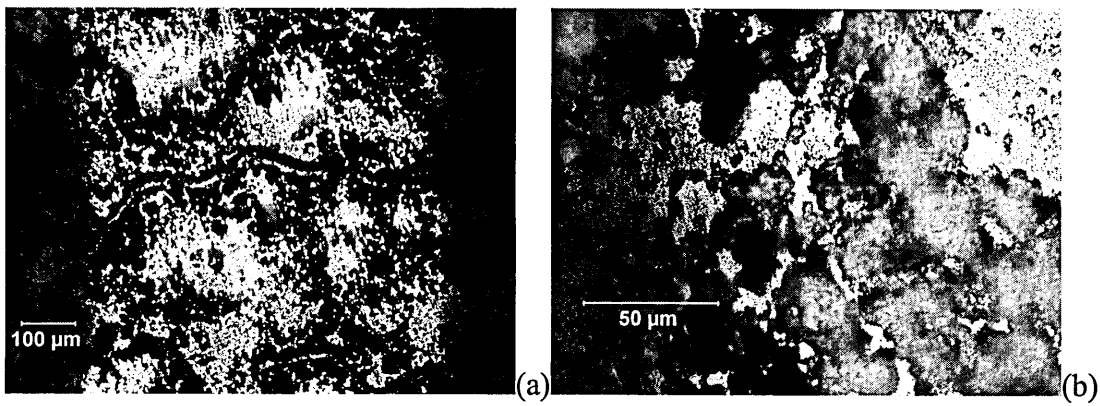


Figure 5.58. Optical microscope pictures of bridge design 7 at two scales

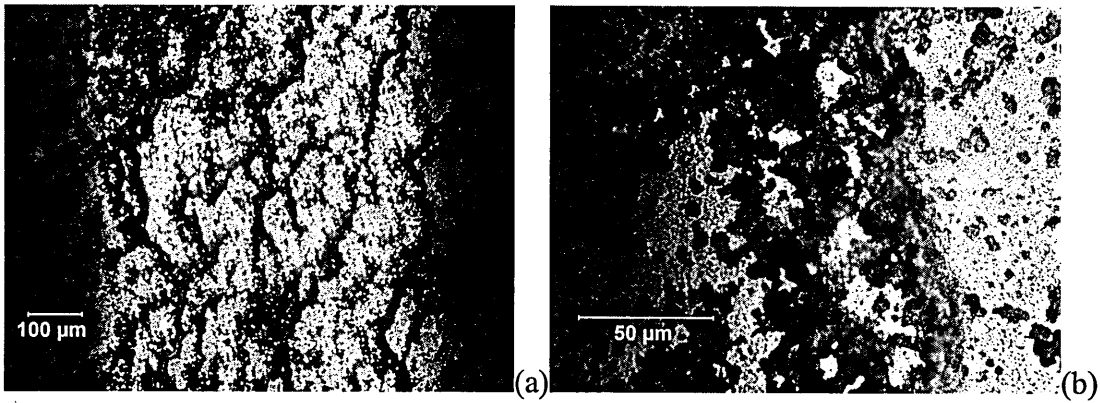


Figure 5.59. Optical microscope pictures of bridge design 8 at two scales

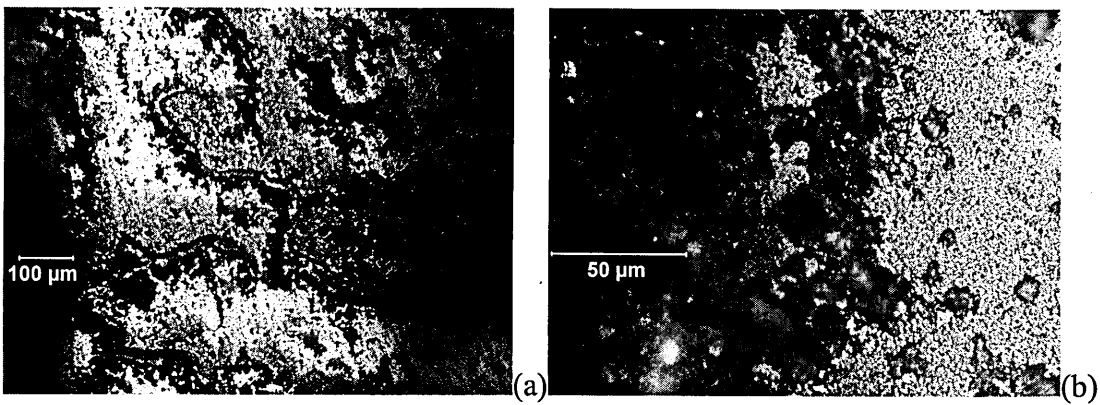


Figure 5.60. Optical microscope pictures of bridge design 9 at two scales

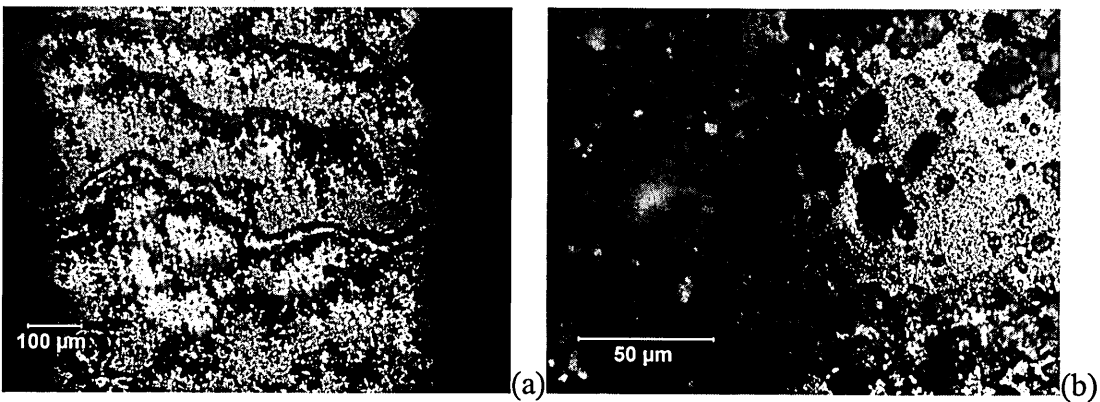


Figure 5.61. Optical microscope pictures of bridge design 10 at two scales

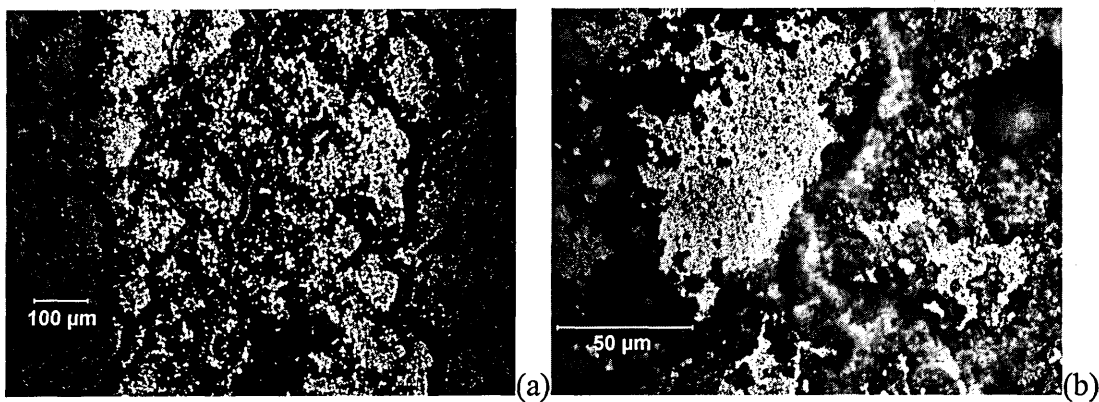


Figure 5.62. Optical microscope pictures of bridge design 11 at two scales

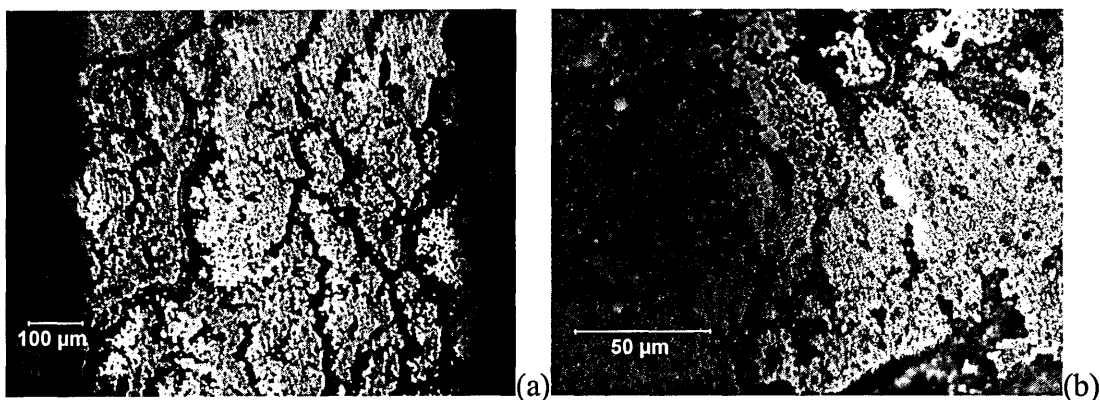


Figure 5.63. Optical microscope pictures of bridge design 12 at two scales

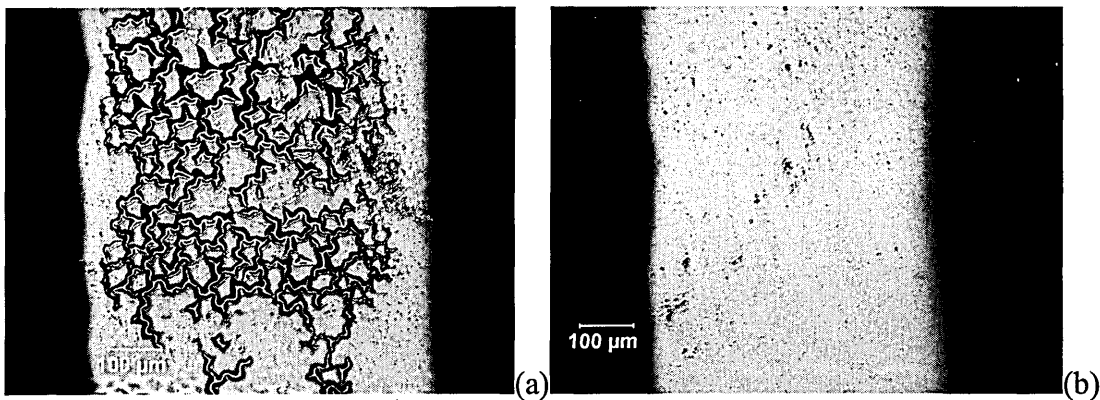


Figure 5.64. Optical microscope pictures of two samples of Platinum on glass

### 5.5.2. Electrical Characteristics

It was thought that the finger contacts were adding large series resistance to the cell, and possibly having some breakages that would isolate portions of the cell and further reduce the output by there being effectively a smaller device. Several samples each containing sixteen platinum fingers bridging a film of P25 were made and tested for their resistance. The bridges were made of varying length to determine if there was a

maximum length before significant breakage occurred (if the bridge was broken laterally, the two ends of the finger would be open circuit). The mean resistance of each bridge length is shown in fig 5.65. It is clear that there was a linear relation between the length of the bridge and its resistance, whilst there were no short circuits observed. This meant that large area devices, where current must pass through a long length of top contact, would have a low output for the large area. The device would have to be split into strips with thick "bus-bars" between them to carry away the current and prevent a large series resistance. Any generated electrons travelling just 6mm along the top contact would see in excess of 3000 ohms. This is devastating to the efficiency of the device and holds a clue as to the low output of the designs in this research.

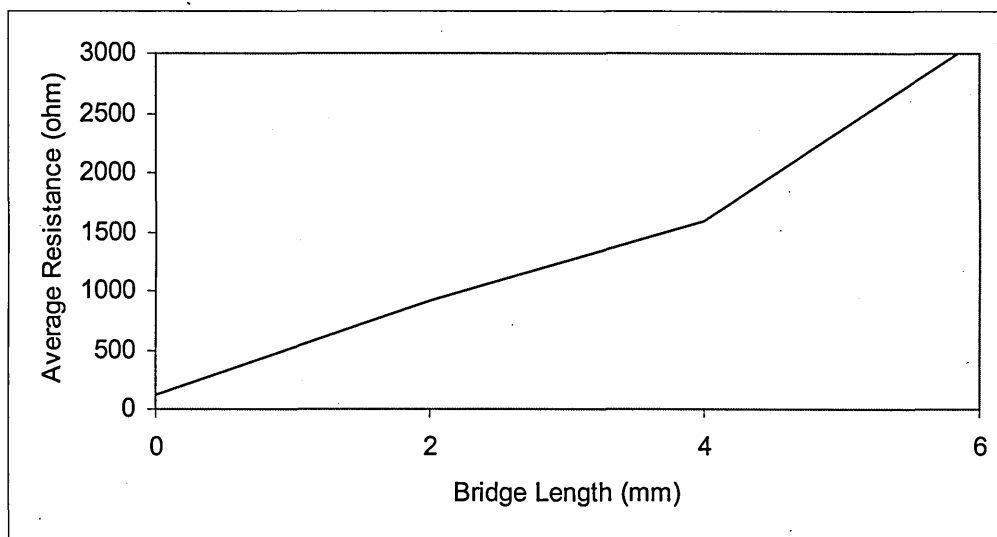


Figure 5.65. Mean resistances of sixteen bridge devices of length from 0mm to 6mm

In addition to a varying length of bridge across a rough layer, a study was performed of a constant length of bridge across a varying rough layer to observe the effects on the surface roughness of adding different layers on top of the P25 layer. I(V) graphs were obtained for each bridge test device to observe the effect of conduction through a thin metal film applied on top of a rough porous structure. The designs of the bridges are shown in table 5.14.

Table 5.14. List of bridge designs. All solutions are bath soaked. P25 is flood printed.

Design	Layer 0	Layer 1	Layer 2	Top contact
1	P25 10mg/ml	CuPc 10mg/ml	nothing	Platinum 100nm
2	P25 10mg/ml	CuPc 10mg/ml	nothing	Platinum 100nm
3	P25 10mg/ml	CuPc 10mg/ml	PVK 10mg/ml X 3	Platinum 100nm
4	P25 10mg/ml	CuPc 10mg/ml	PVK 10mg/ml X 3	Platinum 100nm
5	P25 10mg/ml	CuPc 10mg/ml X 3	nothing	Platinum 100nm
6	P25 10mg/ml	CuPc 10mg/ml X 3	nothing	Platinum 100nm
7	P25 10mg/ml	CuPc 10mg/ml X 3	PVK 10mg/ml X 3	Platinum 100nm
8	P25 10mg/ml	CuPc 10mg/ml X 3	PVK 10mg/ml X 3	Platinum 100nm
9	P25 10mg/ml	Rose Bengal 10mg/ml X 3	nothing	Platinum 100nm
10	P25 10mg/ml	Rose Bengal 10mg/ml X 3	nothing	Platinum 100nm
11	P25 10mg/ml	Rose Bengal 10mg/ml X 3	PVK 10mg/ml X 3	Platinum 100nm
12	P25 10mg/ml	Rose Bengal 10mg/ml X 3	PVK 10mg/ml X 3	Platinum 100nm

The resistance of each bridge test device was obtained by a calculating R as the reciprocal of the gradient of the data. The resistances for every device are shown in table 5.15, to show again the effect of dispersion of thickness.

Table 5.15. Calculated mean resistances of the bridge test devices.

Design	Device	Mean R(ohm)	Design	Device	Mean R(ohm)	Design	Device	Mean R(ohm)
1	1	1.3165E+02	5	1	2.6853E+02	9	1	2.0510E+04
	2	1.7521E+02		2	3.9949E+03		2	1.2111E+05
	3	2.7295E+02		3	9.6517E+03		3	1.5703E+04
	4	3.7723E+02		4	4.2965E+03		4	2.0812E+03
	5	5.4988E+02		5	4.1701E+03		5	4.1123E+03
	6	4.9470E+08		6	1.6275E+03		6	2.1959E+03
2	1	3.9106E+02	6	1	1.3710E+02	10	1	1.2303E+02
	2	7.3001E+02		2	1.8673E+02		2	2.4003E+02
	3	7.5064E+02		3	2.0192E+02		3	5.3573E+02
	4	1.1606E+03		4	3.4734E+02		4	2.9018E+02
	5	1.3823E+03		5	2.3240E+02		5	2.3499E+02
	6	1.5320E+03		6	1.8814E+02		6	2.4334E+02
3	1	4.0186E+01	7	1	7.8272E+01	11	1	5.3329E+02
	2	5.3970E+01		2	1.0162E+02		2	7.1950E+02
	3	4.9547E+01		3	5.7937E+02		3	6.0457E+02
	4	7.8232E+01		4	2.1051E+02		4	4.3431E+02
	5	7.7939E+01		5	9.9053E+01		5	2.3106E+02
	6	1.5333E+02		6	6.9654E+01		6	2.5678E+02
4	1	2.6936E+01	8	1	9.8810E+01	12	1	9.3771E+01
	2	2.6455E+01		2	1.2516E+02		2	6.3561E+01
	3	3.1743E+01		3	9.8452E+01		3	8.1421E+01
	4	2.8104E+01		4	5.3115E+01		4	1.1964E+02
	5	4.8716E+01		5	1.2217E+02		5	4.1657E+02
	6	6.2560E+01		6	7.8675E+01		6	1.4994E+02

Each device was tested three times to observe repeatability, and only a few devices showed signs of changes with tests. All of the designs have bridges of various resistances, and this can only be due to different thicknesses of the top metal contact as every top contact is made of an identical area finger, and all of the samples have a flat glass slide as a substrate and therefore the layers will be flat (but not smooth) and of nominally homogenous thickness. A variation of thicknesses of top metal contact within individual devices was produced because of the peculiarity of the sputtering system in that it deposited material at a range of rates, depending on the distance away from the centre of the beam (both vertically and horizontally). A thicker finger contact gives a lower resistance along the contact and this can be seen most clearly in table 5.15, as the calculated resistances tend to get lower towards the centre or towards one edge of the sample. This thickness dispersion manifests itself in several measurements in this research. The designs with the PVK layer tend to be an order of magnitude of resistance less than identical designs without the PVK layer, showing that this layer has a large effect on the quality of the cells, something which is evidenced by the general improvement in the photovoltaic response with designs containing a PVK layer over those that do not. There is not much of a change in the resistance of designs with increased layers of dye, and there is not much of a change in the density of colour in the samples. It may be possible that dyes cannot be built up as multi layers by the bath soaking method, perhaps because subsequent layers of dye just washed out previous layers and left one layer thickness on the P25. It is important to note that the samples were also translucent, meaning that only a portion of the light incident on the sample would be absorbed and could lead to photocurrent. This is yet another reason as to the low efficiency of the solar cells.

## 5.6. Optical Modulator

The modulator setup was developed to illuminate samples with very short trapezoidal pulses that have a very fast cut-off time to allow for the measurement of the photogenerated carrier lifetime. Basic theory of the phenomena of recombination has been presented and the stages of design and testing that resulted in the final system are shown below.

### 5.6.1. Development

After a review of what is commercially available for the modulation of light with the required parameters, it was decided that nothing could be purchased that was sufficiently fast and cost within a few hundred pounds, and so an optical modulator had to be developed.

The simplest method of chopping a beam of light is to use a thin, black, slotted disk, rotating at high speeds of about one hundred rotations per second, which regularly and neatly intercepts a beam creating pulses of light from a continuous source. The time taken for one of the blades of the disk to chop a beam is the time taken for the blade to move a distance equal to the width of the beam as shown in fig 5.66. The cut-off time is the time from 'full light' to 'zero light'.

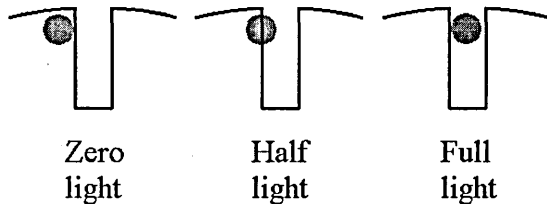


Figure 5.66. Description of chopper action.

If a 10cm wide (0.314m circumference) chopper disk is rotating at 100Hz, and is chopping a 1mm wide beam, then the cut-off time would be  $31.85\mu\text{s}$ , which is far too slow to be of use for lifetime measurements. However the response of such a modulator (fig 5.67) is thought to be better than that of laser pulse generators, which give such a pulse as that in fig 5.68, which would be more difficult to model.

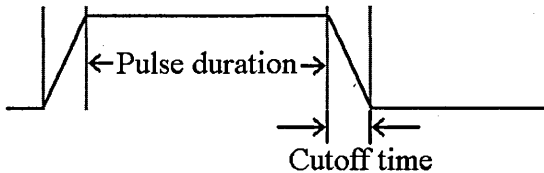


Figure 5.67. Trapezoidal pulse

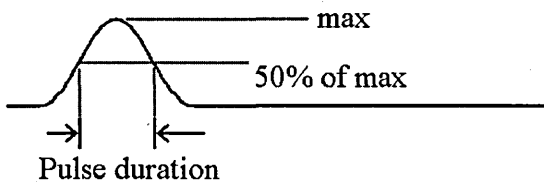


Figure 5.68. Rounded pulse.

If the size of the chopper is increased to 20cm wide, the beam is focused down to  $10\mu\text{m}$ , and the cut-off time required is set to 10ns, the required speed of the chopper can be calculated as 95,541rpm. This is quite impractical, since focusing down to  $10\mu\text{m}$  is difficult without expensive lenses, and at such high speeds, the chopper is very likely to fly apart in a highly dangerous fashion. It shows that this simple chopper arrangement is unsuitable for the requirements of the project, and must be improved upon.

The speed or the spot focusing could be halved by using two disks spinning in opposite direction so that the (in phase) slots close at a speed twice as that for one slot, meaning they only need to move half as far in the same time and thus for the same speed, the cut-off time is halved. The major problem with this method is that the phase difference of the disks must be controlled to a high precision, when the disks are spinning at a high

rate. If one disk were to lag behind by even a small amount (e.g. up to the spot width -  $10\mu\text{m}$ ), then cut off will degrade to that of a single disk ('cut off too late' in fig 5.69). The disks cannot be simply mechanically linked when running at tens of thousands of rpm, and electronically controlling the phase will also be difficult at the stated speeds, so a multiple disk solution is not practical.

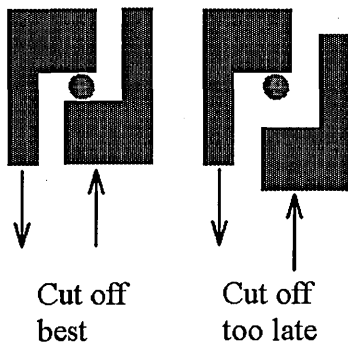


Figure 5.69. Demonstration of the criticality of relative phase of the disks.

It was first thought that moving the light beam (by, for example reflecting the beam from a rotating mirror) in the opposite direction to the slot movement could increase cut-off speed, but the spinning mirror idea could work by itself as shown in fig 5.70.

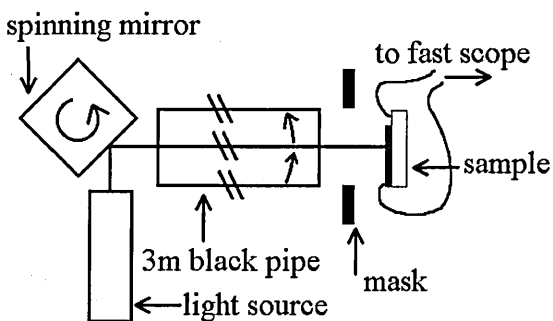


Figure 5.70. Chopper based on spinning mirror.

If the mirror is spinning at 30,000rpm (500Hz) then the reflected beam will sweep at 60,000rpm (1000Hz) due to  $\theta-2\theta$  angles, and if the spot remains at 1mm wide at the mask position, the mask is 3m from the mirror, and then the cut-off time can be easily calculated as 53ns. This system is much better than the spinning disk design, because

the spot does not need very fine focusing (although it will help) and the mirror is small, so it can be driven at high speeds safely. The only real problem with the system is that instead of the sample being exposed to a pulsing spot of light, the spot will scan across the sample for the duration of the pulse width. This effect is shown in fig 5.71, and is undesirable since the sample will not achieve a steady illumination across its surface and thus will not achieve a steady concentration of free carriers throughout.

The trapezoidal light pulse shown in fig 5.71 assumes that the spot is square, when it is actually round. A round spot will give a slightly different shape of roll off as shown in the comparison in fig 5.72. Converting the round spot to a square one accurately can be done quite simply by enlarging the spot with a lens, passing the spot through a square hole in a mask, before refocusing and recollimating the square spot.

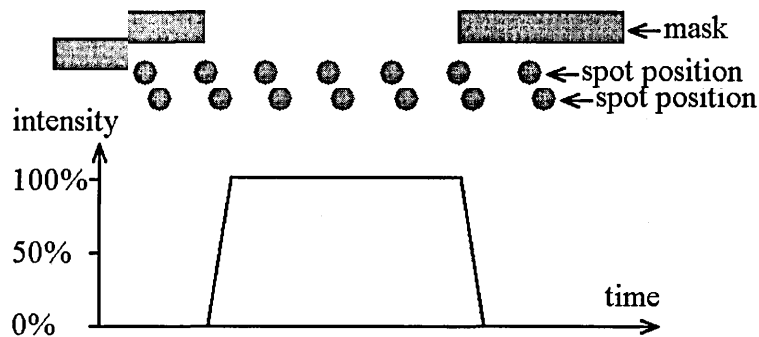


Figure 5.71. Problem of the spot scanning effect.

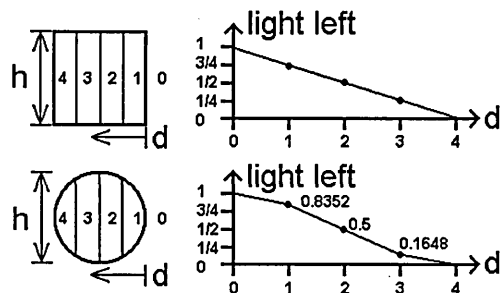


Figure 5.72 Square spot vs round spot light cut off. 'd' represents the slot/mask edge position over time.

The new system design is much better than the old disk design, but still needs to be improved; the cut off time is too large (but in the right order of magnitude) and the spot scanning must be corrected.

To increase the cut-off speed, the spot size could be decreased, and/or the spot speed could be increased. If the spot were brought to a sharp focus (say 0.1mm) at the mask position, this would increase the speed by ten times. It would be best to limit the number of lenses in the system as good lenses are expensive and each set would have to be adjusted for each wavelength. The spot speed may be increased by increasing the speed of the mirror (already at a practical limit for inexpensive - £100 - drives) or by increasing the rate of angular change of the beam.

If a ray of light passes through a concave lens, it is bent away from the normal, so that small changes in the beam position would be amplified as shown in fig 5.73.

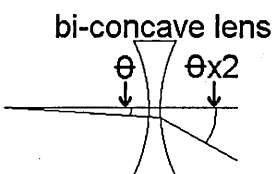


Figure 5.73. Amplification of the beam angle by using a concave lens.

This idea however is useless for this system as each ray is bent through a different angle causing the small spot input to change to a huge spot output, a change that cannot be rectified with extra optics.

The basis of the new design is that a beam incident on a mirror that has undergone an angle change has the reflected beam changed by double the angle. However, if the reflected beam is incident on another mirror that has also undergone the same angle change then the total beam angle change is four times the mirror angle change. This can

be repeated indefinitely, to provide all of the angle amplification needed (or possible, since there is some light loss on each reflection). The numerous spinning mirrors must be positioned so that the beam angle change increases with each reflection and none of the mirrors cancel out. Fig 5.74 and fig 5.75 show two possible mirror set-ups for multiple reflection angle amplification.

Both multiple mirror set-ups would work, but the series design is better because there are only two moving parts. The series design could be simplified by having two long polished sections of bar linked in the same way (there is no need to have separate mirrored sections). It can also be simply shown that by having only one mirrored section reflecting the light off a stationary mirror, the beam angle is increased by half as much as with two mirrored sections. This would have the benefit of only having a single moving part driven straight from the drive, whilst still allowing many reflections and thus a fast sweeping beam.

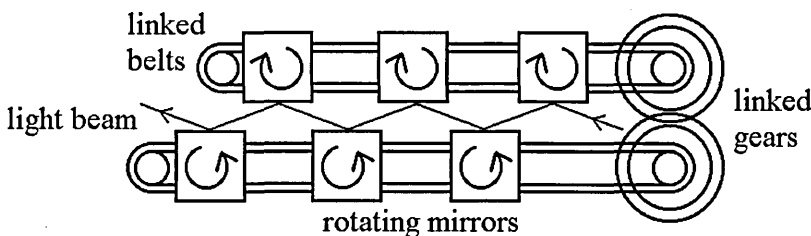


Figure 5.74. Multiple rotating mirror system – mirrors are parallel

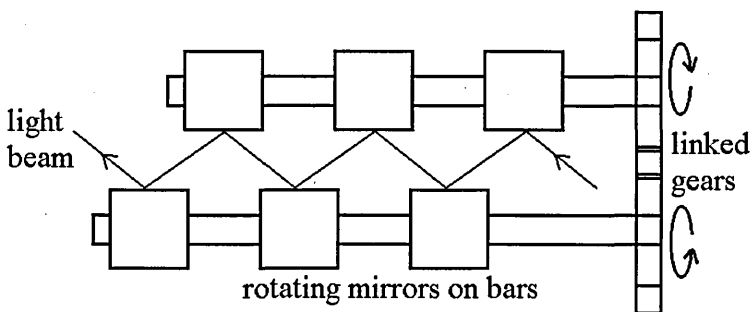


Figure 5.75. Multiple rotating mirror system – mirrors in series

With a single long spinning bar and a stationary mirror, the rate of angle change of the beam becomes;

$$\frac{d\theta_{beam}}{dt} = 2 \times n \times \frac{d\theta_{bar}}{dt} \quad (5.3)$$

where  $n$  is number of reflections with the spinning bar,  $\frac{d\theta_{bar}}{dt}$  is the speed of rotation of the bar, and  $\frac{d\theta_{beam}}{dt}$  is the speed of rotation of the laser

The limit of the number of reflections is set by the length of the bar, the width of the spot (and thus reflections per unit length of bar), and the light loss per reflection (which can be reduced by using optical quality mirrors). The spot has some width, and must pass the edge of the stationary mirror at least as far away as this width, and must be reflected, and reincident on the stationary mirror as least a spot width in from the edge, and therefore the maximum number of reflection can easily be calculated as;

$$n_{max} = \frac{L_{bar}}{W_{spot}} \quad (5.4)$$

Say for a bar length of 10mm (a good length that does not need supporting at the other end with a bearing), and a spot width (at the point where it leaves the source) of 1mm, a maximum number of reflections of ten is practically possible. With the above example of use of a spinning mirror, the cut-off time would be reduced with ten reflections to 5.3ns, which is an appropriate time.

The time can also easily improved further by increasing the distance from the mirror to the mask, a solution that can be made more practical by 'folding down' the distance with parallel mirrors (which must reflect from the surface, and not from the back of mirrored glass which would produce multiple reflections). A distance of 12 metres or more can easily be produced on a relatively small table, reducing the cut-off time still further,

down to say, 1.3ns - perfectly acceptable. If the other end of the bar is held with a bearing of the same quality as that used by the driving motor the rotating mirror could be made up to, say, 150mm, giving up to 150 reflections and reducing the cut-off time to 88ps, which easily rivals some of the best commercial systems, but has the added bonus of being able to take any single wavelength source, is cheap to make, and produces a trapezoidal pulse.

A problem with the distance folding down is that there are now several points where the beam intersects the plane in which the mask is fixed. As the spinning mirror rotates, each point in turn will move along towards the mask, and scan across it. Each point moves slower than the last (because it is a smaller effective distance from the source), so the sample would be exposed to a series of successively slower pulses, which may be undesirable (although the scientist using such a system would have instant access to several speeds of pulse at once). To solve this, the whole beam must be cut off using a matt black triangular block, after the first point has scanned across the sample, which can be simply done as shown in fig 5.76.

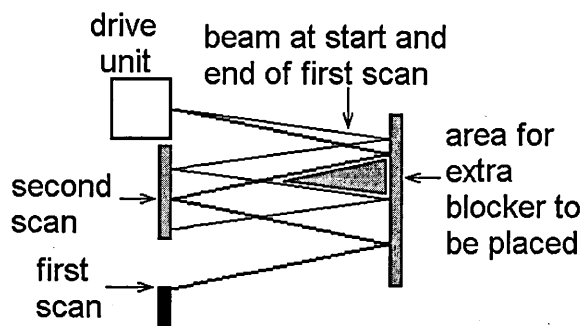


Figure 5.76 Position of matt black light blocker to stop beam after one full-speed pulse.

If a bi-convex lens is placed after the mask, with its optical axis in line with the mid point of the beam swing, then all angles of the beam will intersect at the focal point of the lens, creating a small, stationary, pulsing spot. If a glass slide coated with a thick

film of TiO<sub>2</sub> nanocrystals (such as P25) is positioned at the focal point of the lens, then the light scattering effect of the film turns the small spot in to a large diffuse spot (that still pulses as before) which is suitable to illuminate a small (e.g. 5mm square) sample. An optical modulator is thus produced that gives stationary, trapezoidal pulses, with variable duration (change speed/mask gap width), with fast cut-off, and which can illuminate a small sample, as shown in fig 5.77

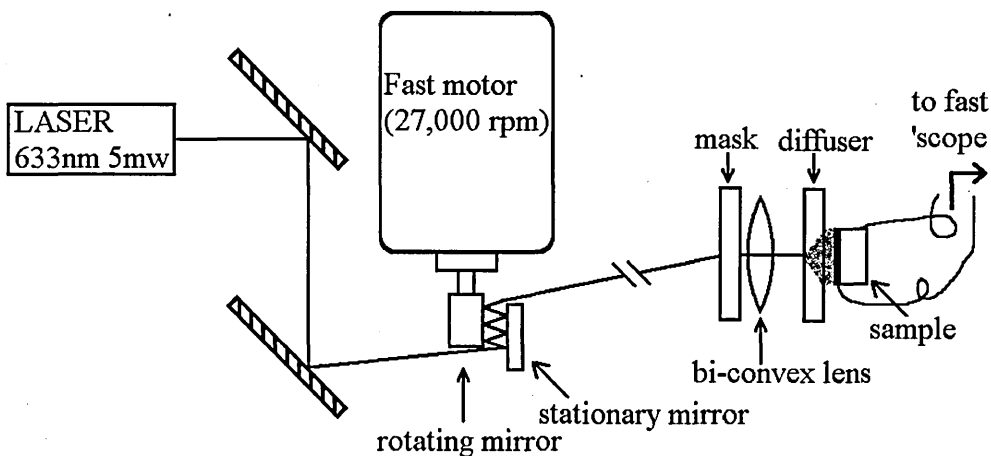


Figure 5.77. Full design of optical modulator based on a fast motor but without distance folding.

It would be beneficial to be able to take the output from a monochromator, and feed this into the chopper. Many attempts were made to optically alter the diverging output from a monochromator using e.g. collimators, various lens arrangements, pinholes and slits etc, but a collimated beam could not be made. Instead, the user of the system must use lasers of varying wavelength to obtain a spectral response from the sample.

### 5.6.2. Final Design and Tests

An optical chopper built using a woodworking router as the drive, with a specially made mirrored section, and was tested with a photodiode to measure the rotational frequency of the motor and to observe the quality of the pulse produced. The motor has a speed

setting from one to six, and the settings one to three were tested (higher settings become increasingly loud and make the motor hotter as it is driving without mechanical load). The frequencies for settings one, two and three are 203.25Hz, 277.77Hz, and 349.65Hz respectively. The speed of the motor is thus nearly linear with setting. Plots of the oscilloscope readings are shown in fig 5.78 and fig 5.79. Fig 5.79 shows a faster time base to show the nature of the pulse. The shape (and cut off and cut on times) was the same for each speed with the only difference observed was that at higher speeds, the voltage pulse does not get as low. This is thought to be due to the photodiode being unable to keep up with the rate of change of light incident on it, and also that the light pulse at higher speeds cuts off before the photodiode has finished detecting the start of the pulse, hence it detects less light. The pulse in fig 5.79 drops in about  $10\mu\text{s}$ , and since the shape is the same for all speed, the actual cut-off time for the light pulse must be better than  $10\mu\text{s}$  at the slowest practical setting for the system.

Samples of silicon with fingers of aluminium deposited were illuminated with the laser directly from the source. No change was observed in the normal planar resistance (about  $20\text{k}\Omega$ ) when illuminated. A solar simulator with full brightness output was then used instead, but still no change in the resistance was observed. It is possible that the light did excite some free carriers, but on top of the already considerable concentration of free carriers in the doped silicon, these extra carriers may have been insignificant. Tests were also carried out on samples of CuPc on interdigitated electrodes, but again, no response was observed either with the pulses or with steady illumination. More work must be done to discover the range of operating parameters required to observe the phenomena.

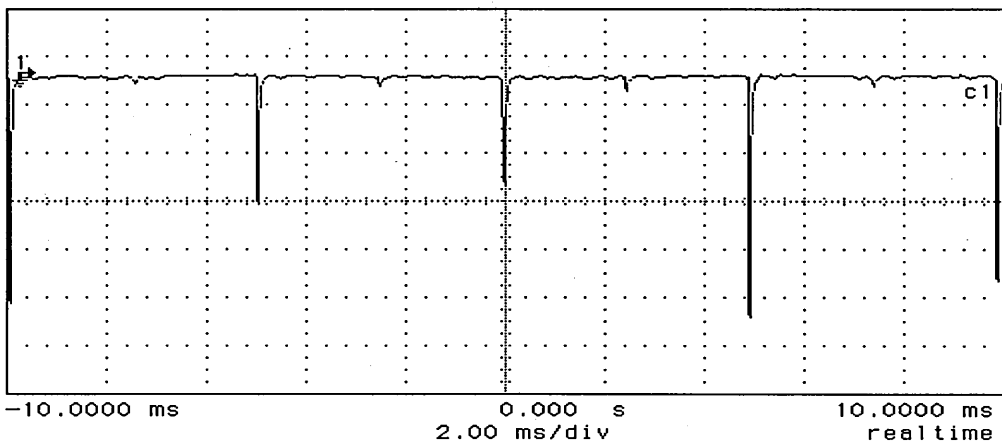


Figure 5.78. Output of the photodiode at speed setting one.

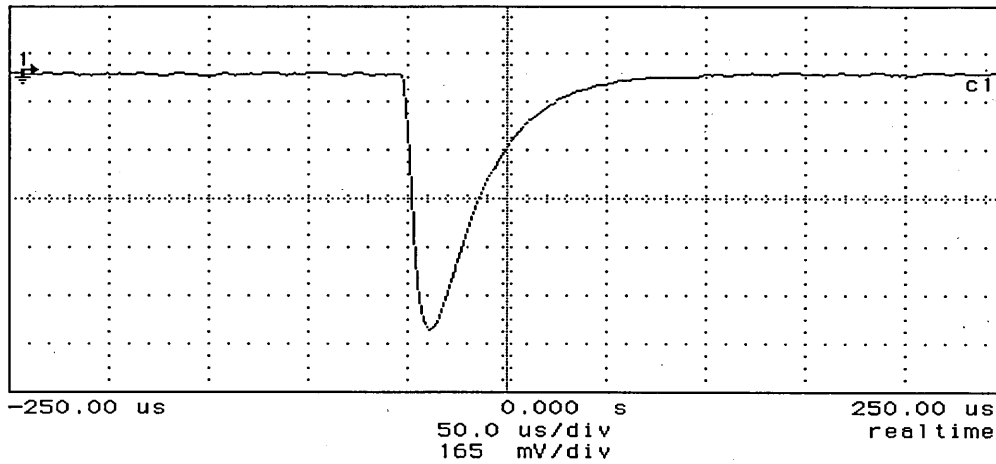


Figure 5.79. Typical pulse shape of the output from the photodiode.

#### Reference List

- (1) Mardare D, Baban C, Gavrila R, Modreanu M, Rusu GI. Surface Science 2002; 507-510:468-472.
- (2) Springer SG, Schmid PE, Sanjines R, Levy F. Surface and Coatings Technology 2002; 151-152:51-54.
- (3) Takeda S, Suzuki S, Odaka H, Hosono H. Thin Solid Films 2001; 392(2):338-344.
- (4) Viseu TMR, Almeida B, Stchakovsky M, Drevillon B, Ferreira MIC, Sousa JB. Thin Solid Films 2001; 401(1-2):216-224.
- (5) Radecka M, Zakrzewska K, Brudnik A, Posadowski W. Thin Solid Films 1999; 343-344:152-155.
- (6) Lapostolle F, Huu Loi T, Billard A, Frantz C. Surface and Coatings Technology 1997; 97(1-3):574-581.

- (7) Treichel O, Kirchhoff V. *Surface and Coatings Technology* 2000; 123(2-3):268-272.
- (8) Takeda S, Suzuki S, Odaka H, Hosono H. *Thin Solid Films* 2001; 392(2):338-344.
- (9) Ohsaki H, Tachibana Y, Mitsui A, Kamiyama T, Hayashi Y. *Thin Solid Films* 2001; 392(2):169-173.
- (10) Tomaszewski H, Poelman H, Depla D, Poelman D, De Gryse R, Fiermans L et al. *Vacuum* 2002; 68(1):31-38.
- (11) Vergohl M, Malkomes N, Staedler T, Matthee T, Richter U. *Thin Solid Films* 1999; 351(1-2):42-47.
- (12) Tomaszewski H, Poelman H, Depla D, Poelman D, De Gryse R, Fiermans L et al. *Vacuum* 2002; 68(1):31-38.
- (13) R.Swanepoel. *J Phys E: Sci Instrum* 1983; 16:1214-1222.
- (14) Miao L, Jin P, Kaneko K, Terai A, Nabatova-Gabain N, Tanemura S. *Applied Surface Science* 2003; 212-213:255-263.
- (15) Dannenberg R, Greene P. *Thin Solid Films* 2000; 360(1-2):122-127.
- (16) Kontos AI, Arabatzis IM, Tsoukleris DS, Kontos AG, Bernard MC, Petrakis DE et al. *Catalysis Today* 2005; 101(3-4):275-281.
- (17) Spadavecchia J, Ciccarella G, Vasapollo G, Siciliano P, Rella R. *Sensors and Actuators B: Chemical* 2004; 100(1-2):135-138.
- (18) Litran R, Ramirez-del-Solar M, Blanco E. *Journal of Non-Crystalline Solids* 2003; 318(1-2):49-55.
- (19) Gigimol M, Mathew B. *Polymer International* 2003; 52:973-980.
- (20) Du H, Fuh R, Li J, Corkan A, Lindsey J. *Photochemistry and Photobiology* 1998; 68:141-142.
- (21) Boschloo G, Lindstrom H, Magnusson E, Holmberg A, Hagfeldt A. *Journal of Photochemistry and Photobiology A: Chemistry* 2002; 148(1-3):11-15.
- (22) Regan B, Gratzel M. *Nature* 1991; 353:737.
- (23) Tracey S, Ray A, Shishiyanu T. *IEE Proceedings* 1998; 145(5):383.

## Conclusion And Suggestions For Further Work

---

### 6.1. Discussion of Achievements

- Semiconducting layers of smooth rutile phase  $\text{TiO}_2$  were produced by DC reactive sputtering at room temperature, and without pulsing the DC supply, with a thickness around 200nm (a dispersion in thickness was observed due to sputtering phenomena). Annealed  $\text{TiO}_2$  films showed correct stoichiometry.  $\text{TiO}_2$  films with an extended surface area were made using a fine powder consisting of commercial Degussa P25  $\text{TiO}_2$  and were deposited by the new technique of flood printing developed for this research.
- The semiconducting layers were characterised by various methods; electrically to determine the planar conductivity with and without annealing; optically to determine the refractive index and extinction coefficient spectra with and without annealing, to observe nano and micro scale details of the films, and to observe the band transition properties (using a model fitting algorithm produced by the author for this research); structurally to determine thickness (in comparison to in situ QCM measurements), grain size, crystallographic phase, and stoichiometry.
- Thin films of Copper Phthalocyanine dye and Rose Bengal dye were deposited on differently coated substrates; F:TO,  $\text{TiO}_2$ , and bare glass.
- The dye films were characterised optically to determine changes in the absorption spectra due to different chemical environments.

- Heterojunction solar cells based on the dye layers adsorbed on the semiconducting layers were produced in fifteen different designs with each design based on another to observe the effect of single design changes. Such changes included different thickness of porous TiO<sub>2</sub> layer, and whether a conducting polymer layer is applied. The devices were built up on F:TO coated glass slides and electrical contacts were made by DC sputtering platinum fingers on the top.
- The solar cells were characterised in terms of efficiency, load characteristics, and equivalent circuit model parameters. A model fitting algorithm was produced by the author for this research based on the single diode model incorporating ideality factor, series resistance and reverse saturation current. The effect of the top contact in reducing the efficiency of the cells was studied in isolation to the devices. The contacts were applied to identical sets of layers as are used in the solar cells, which form a rough surface for the contact to be applied onto. Electrical measurements showed high resistance in the range of k $\Omega$  that are cell design dependent, have a dispersion due to thickness dispersion, and manifest as an increased series resistance in the cell.
- An experimental setup capable of measuring the lifetime of photogenerated carriers in the dye films was developed that could produce pulses with a cut off time in the nano-seconds time regime, but can be simply improved to give cut off times in the sub nano-second time regime. The setup was based on modulating a collimated beam of light such as that from a standard laboratory laser.

## 6.2. Contribution to Knowledge

- Rutile phase films of  $\text{TiO}_2$  have been produced by DC reactive magnetron sputtering without in situ heating and without subsequent annealing, and without pulsing the power supply.
- Fifteen progressive designs of heterojunction solar cell have been designed in an attempt to find the optimum structure. The effects of single design changes have been observed and show better change directions for further designs. The designs show that by filling the pores that exist on top of the dye layer with a conductive polymer, the quality of the top contact is improved. A greater thickness of polymer is expected produce a greater quality of top contact and greater cell efficiency.
- An experimental setup has been developed that can illuminated a sample with a trapezoidal pulse with a cutoff time in the nano second time regime, but that only costs a few hundred pounds. Commercial systems produce pulses that are not as simple to use (they are short rounded pulses, not simple trapezoids), but still cost several thousand pounds.
- Two analysis algorithms have been developed to assist in this research; one for fitting a diode model to the electrical characteristics of the cells, and one for fitting the Tauc model to the optical absorption edge of the sputtered  $\text{TiO}_2$  films. These algorithms are very simple to use and changes in each parameter have a quite different effect on the fitting. This means that a good fit is more likely than if two or more parameters have a similar effect on the fitting, as if both parameters change in opposite directions by equal amounts, the result can be the same. The simplest example is the sum of two physically different parameters – there are a plethora of sets of the parameters that give the same result, meaning the effect of each may not be extractable.

### 6.3. Future Work

The structure of the porous layer is an important factor in determining the efficiency of the device. If the pores are too small and hard to reach, the dye may not penetrate far enough (the metal contact certainly won't penetrate far enough) to fill the pores and the space is wasted, and there can be a long depth of oxide for electrons to travel through and thus the efficiency will be reduced. More elaborate measurements of the porous layer, including porosity depth profile will allow for better designs of the layer. Perhaps a graded layer with increasing pore size towards to surface will allow for better coverage with the dye, and better contact between the top contact and the dye. This may be achieved by using increasing amount of PEG filler with the P25 with increasing number of layers, then burning out the PEG chemical or thermally.

Many more designs of solar cell could be made to refine the optimisation. This will of course be a long lasting procedure as there are a plethora of different dyes and conducting polymers and such chemicals that can be used, each at a wide range of concentration or thickness. The device may be multi layered with each layer having a separate and complimentary absorption band. The cell may comprise several devices stacked on top of each other. A problem with using many dye layers is that the series resistance may increase, and the efficiency may decrease even though the overall absorption will increase. The multi device cell could have the same absorption but not the increased resistance, although it would be more difficult to make. Some sort of optimisation algorithm would be very useful to fine tune the device and calculate, for example, the best thickness of a particular layer based on several devices' performances with different thicknesses of that layer. The optical modulator may be utilised in the search for better dyes – it may show which dyes will produce the longest-lived electrons.